

Torsional Oscillator Study for  
Solid  $^4\text{He}$  Growth on  
Graphite and Graphene from the Superfluid

September 2013

Aaron M Koga



I dedicate this work to my family, without whom I would not be here. If this is an accomplishment, it is as much theirs as mine.

## Acknowledgements

I would like to thank my advisor, Keiya Shirahama, for his continued guidance and encouragement. I would also like to acknowledge the invaluable assistance provided by Yoshiyuki Shibayama and the other members in this lab. The opportunity to work with such kind and eager people has been humbling and gratifying.

Thank you also to the members of my thesis committee for many good suggestions and comments.

# Contents

<b>List of Figures</b>	<b>vii</b>
<b>1 Introduction</b>	<b>1</b>
<b>2 Theoretical and Experimental Overview</b>	<b>5</b>
2.1 $^4\text{He}$ Phase Diagram . . . . .	5
2.1.1 Superfluid $^4\text{He}$ . . . . .	6
2.1.2 Solid $^4\text{He}$ . . . . .	6
2.2 The Roughening Transition . . . . .	6
2.3 Epitaxial Growth of Solid $^4\text{He}$ on Graphite from the Superfluid . . . . .	9
2.3.1 Continuous Growth: the Franchetti Relation . . . . .	9
2.3.2 Discontinuous Growth: Layering Transitions . . . . .	11
2.3.3 Experimental Studies of Layering Transitions in Solid $^4\text{He}$ on Grafoil . . . . .	12
2.4 $^4\text{He}$ Adsorption on Graphite and Graphene from the Gas Phase . . . . .	17
2.4.1 $^4\text{He}$ on Graphite . . . . .	17
2.4.2 $^4\text{He}$ on Graphene . . . . .	17
<b>3 Experimental Method and Apparatus</b>	<b>19</b>
3.1 Theory of the Torsional Oscillator Method . . . . .	19
3.1.1 Drive and Detection . . . . .	19
3.1.2 Resonant Modes . . . . .	20
3.1.3 Frequency Shifts . . . . .	22
3.1.4 Oscillation Amplitude . . . . .	23
3.1.5 Oscillation Velocity . . . . .	25
3.2 Grafoil Experimental Cell . . . . .	26
3.2.1 Torsional Oscillator Design . . . . .	26
3.2.2 Grafoil Sample . . . . .	28
3.2.3 Assembly And Fitting . . . . .	29
3.3 Other Experimental Apparatus at Low Temperature . . . . .	31

3.3.1	Cu Platform . . . . .	31
3.3.2	Electrodes . . . . .	33
3.3.3	Heat Switch . . . . .	34
3.3.4	Thermometer and Heater . . . . .	35
3.3.5	Pressure Gauge and Regulator . . . . .	35
3.4	Graphene Experimental Cell . . . . .	39
3.4.1	Graphene Sample . . . . .	39
3.5	Room Temperature Electronics for Temperature, Pressure, Frequency, and Amplitude Measurement . . . . .	42
3.5.1	Temperature Measurement and Regulation . . . . .	42
3.5.2	Pressure Measurement and Regulation . . . . .	42
3.5.3	Frequency and Amplitude Measurement . . . . .	42
3.6	Procedure for Data Acquisition . . . . .	43
3.6.1	Grafoil . . . . .	43
3.6.2	Graphene . . . . .	44
<b>4</b>	<b>Data and Analysis</b>	<b>45</b>
4.1	Raw Data . . . . .	45
4.1.1	Raw Grafoil Data . . . . .	46
4.1.2	Raw Graphene Data . . . . .	46
4.2	Analysis . . . . .	47
4.2.1	Liquid Background . . . . .	47
4.2.2	Growth and Melting of Adsorbed Solid . . . . .	49
4.3	Grafoil Experiment: Growth and Melting Isotherms . . . . .	50
4.4	Graphene Experiment: Growth Isotherms . . . . .	52
4.4.1	Hysteresis . . . . .	53
4.4.2	Vibration and Annealing Effects . . . . .	53
<b>5</b>	<b>Discussion: Grafoil Experiment</b>	<b>57</b>
5.1	Layer-by-layer Growth and Melting . . . . .	57
5.2	Two-Stage Layer Formation . . . . .	60
5.3	Adsorbed Solid Near $P_s$ . . . . .	61
5.4	Dips in the Isotherms . . . . .	61
5.5	Energy Dissipation ( $Q^{-1}$ ) . . . . .	62

<b>6 Discussion: Graphene Experiment</b>	<b>63</b>
6.1 A More Ideal Substrate than Grafoil . . . . .	63
6.2 2D Structural Transitions . . . . .	64
6.2.1 1/5 . . . . .	66
6.2.2 1/3 . . . . .	66
6.2.3 4/7 . . . . .	67
6.2.4 0.6 . . . . .	68
6.2.5 0.82 . . . . .	68
6.2.6 Discontinuous Growth Below $T_R$ . . . . .	69
6.3 Estimation of Commensurate Structure Energies . . . . .	70
6.3.1 Internal Energy of Helium . . . . .	70
6.3.2 Internal Energy of Phase $C_i$ , $U(C_i)$ . . . . .	70
6.3.3 Condition for the Growth of $C_i$ . . . . .	71
6.3.4 Internal Energy Difference Between Two Commensurate Phases $\Delta U(C_i \rightarrow C_j)$ . . . . .	71
6.4 Dips and Overshoots . . . . .	72
6.4.1 Melting and Freezing . . . . .	72
6.4.2 Layer Density Change . . . . .	73
6.4.3 Adsorbed Solid Roughness . . . . .	73
<b>7 Conclusion</b>	<b>75</b>
<b>A Appendix</b>	<b>77</b>
A.1 Sample Surface Area Measurements: Nitrogen Adsorption . . . . .	77
A.2 Temperature Dependence: Empty Cell and Low Pressure Measurements	81
A.3 Grafoil Isotherms . . . . .	84
A.3.1 Melting . . . . .	84
A.3.2 Freezing . . . . .	90
A.4 Graphene Isotherms . . . . .	95
A.5 Tunneling of $^4\text{He}$ into Carbon Samples . . . . .	100
<b>References</b>	<b>103</b>



# List of Figures

2.1	Phase diagram for $^4\text{He}$ at low temperature. Figure taken from (1), copyright (2005) by the American Physical Society. . . . .	5
2.2	Sketch of the liquid-solid interface. . . . .	7
2.3	Sketch of solid adsorbed on a substrate under the Franchetti Relation. . . . .	10
2.4	Sketch of layering transitions showing $T_{c,n}$ becoming lower with lower layer number. Figure taken from (2), copyright (1984) by the American Physical Society. . . . .	11
2.5	Sketch of the tortuous grafoil structure made of many individual graphite sheets. . . . .	13
2.6	Penn. State Group's observations using the fourth sound method. Fourth sound minima occur at approximately half integer Franchetti numbers (horizontal axis). Figure taken from (2), copyright (1984) by the American Physical Society. . . . .	13
2.7	Israel Group's adsorption isotherms. Kinks occur at approximately whole integer layer number (vertical axis). Figure taken from (3), copyright (1984) by the American Physical Society. . . . .	14
2.8	Penn. State Group's observation of two-stage layering transitions. Additional fourth sound minima are seen on the low pressure side of each established transition below 0.95 K. Horizontal lines connected by vertical bars mark the quantity $P_{\text{step},n} - P_{\text{kink},n}$ . Figure taken from (4), copyright (1992) by the American Physical Society. . . . .	15
2.9	Sketch of kink and step surface defects. . . . .	15
3.1	Sketch of the torsional oscillator method. . . . .	20
3.2	Sketch of torsional and floppy modes in simple harmonic oscillator. . . . .	21
3.3	Sketch of typical torsional oscillator frequency response of an empty cell and a $^4\text{He}$ filled cell as a function of temperature. . . . .	22
3.4	Drawing of the vector relationship including delta. . . . .	24

3.5	Sketch of $A(\omega)$ for a given $I$ and $\gamma$ . . . . .	24
3.6	Sketch of various $A(\omega)$ with different $Q$ values. . . . .	25
3.7	Sketch of the cell, which was hung on the mixing chamber. . . . .	26
3.8	Schematic of the AgCu oscillator, BeCu cap, and Al movable electrode. . . . .	27
3.9	Sketch of the grafoil stack held by the stainless steel holder. Not drawn to scale. . . . .	29
3.10	Sketch of brass holder used to machine the stack with the lathe. Not drawn to scale. . . . .	30
3.11	The machined grafoil-Ag foil sample. . . . .	30
3.12	The sample after being glued into the cap. . . . .	31
3.13	Schematic of the copper platform. . . . .	32
3.14	Schematic of the fixed electrodes and their holder. . . . .	33
3.15	Photograph of the assembled cell surrounded by the brass holder and fixed electrodes. . . . .	34
3.16	Sketch of the heat switch used to connect the copper platform to the mixing chamber. . . . .	35
3.17	Picture of the thermometer and heater mounted to the copper platform, mounted below the mixing chamber by the heat switch . . . . .	36
3.18	Schematic of the capacitive pressure gauge. Not drawn to scale. . . . .	37
3.19	Sketch of the cell and system for pressure regulation. The same system was used to regulate the pressure in both experiments. . . . .	38
3.20	Schematic of the torsional oscillator used in graphene measurements. Not drawn to scale. . . . .	39
3.21	SEM images of the bare graphene sample. . . . .	40
3.22	(A): Image of the pressed graphene sample in the oscillator cap. (B): Assembled oscillator on the Cu platform. . . . .	41
3.23	Block diagram of the feedback loop used to measure the oscillator frequency. . . . .	43
3.24	Sketch of the pressure-temperature paths for sample preparation and measurement of melting data in the grafoil experiment. . . . .	44
4.1	Sample raw data from the graphene cell for frequency change from time=0 $\Delta f$ , $Q^{-1}$ , and $P$ . The cell comes to equilibrium at each pressure. . . . .	45

4.2	Raw melting data from the grafoil experiment as a function of $P$ for $f$ and $Q^{-1}$ taken at 0.9 K above 1.6 MPa. Vertical solid lines mark the frequency shifts coinciding with dissipation. The inset shows $f$ from the same isotherm below 1.6 MPa. The liquid background $f_L$ is plotted as the dotted line (see Sect. 4.2.1).	46
4.3	Raw data as a function of $P$ showing $f$ and $Q^{-1}$ taken at 1.05 K. The dotted line shows the frequency of the liquid background $f_L$ (see Sect. 4.2.1).	47
4.4	Selected growth and melting isotherms from the grafoil experiment. From top to bottom: Growth at 1.6 K, melting at 1.1 K, and melting at 0.9 K. The 1.6 K and 1.1 K curves are shifted vertically for easy viewing. The horizontal axis is scaled with the Franchetti relation. Solid lines mark the onset of original layering transitions and dotted lines mark the onset of secondary transitions.	50
4.5	Selected growth and melting isotherms from the grafoil experiment. From top to bottom: Melting at 0.1 K, growth at 0.8 K, and growth at 0.1 K. The 0.1 K melting and 0.8 K growth curves are shifted vertically for easy viewing. The horizontal axis is scaled with the Franchetti relation. Solid lines mark the onset of original layering transitions and dotted lines mark the onset of secondary transitions.	51
4.6	Grafoil experiment $n$ for melting isotherms from 1.2 K to 0.1 K. The horizontal axis is scaled by the Franchetti relation.	51
4.7	Grafoil experiment $n$ for growth isotherms from 1.2 K to 0.1 K. The horizontal axis is scaled by the Franchetti relation.	52
4.8	Graphene experiment $n$ for the 1.05 K and 0.6 K isotherms. Arrows mark the discontinuous jumps in solid coverage. The 1.05 K isotherm is vertically offset by 2 layers for easy viewing.	52
4.9	Graphene experiment. (A): Solid $^4\text{He}$ coverage for all isotherms from 1.65 K and 0.1 K. The isotherms are vertically offset for easy viewing. (B): $1/Q$ for all isotherms from 1.65 K and 0.1 K. The isotherms are vertically offset by a multiplicative factor.	54
4.10	Graphene experiment. Hysteresis above 1.6 MPa taken at 0.7 K. Black data points for increasing pressure and blue data points for decreasing pressure. The first point at 1.6 MPa is assigned $n = 2.0$ .	55
4.11	Selected graphene isotherms from different experimental runs plotted together for comparison. Inset shows the chronological order in which isotherms were taken and the thermal cycling and vibrations of the cell between each isotherm. Data are offset vertically.	55

5.1	Sketch of grafoil pore structure immersed in superfluid $^4\text{He}$ . . . . .	58
5.2	Sketch of the distribution of binding energies on various substrates. . . . .	59
6.1	Selected grafoil and graphene freezing isotherms plotted together for comparison. The horizontal axis is scaled using the Franchetti relation. . . . .	64
6.2	The 0.6 K graphene isotherm offset vertically. The solid blue line shows the extrapolation to $P = 0$ MPa (see text). Horizontal lines mark fractional $n$ in the fifth layer. Red horizontal bars mark pressure differences between the labeled commensurate phases (see text). . . . .	65
6.3	All graphene isotherms below 1.2 K offset vertically. The solid blue line shows the extrapolation to $P = 0$ MPa (see text). Horizontal lines mark fractional $n$ in the fifth layer. Red horizontal bars mark pressure differences between the labeled commensurate phases (see text). . . . .	66
6.4	A possible $1/5$ commensurate structure. Red hexagons show the in-plane confinement (see Sect. 6.3.2). . . . .	67
6.5	The well known $1/3$ commensurate structure. Red hexagons show the in-plane confinement (see Sect. 6.3.2). . . . .	67
6.6	$4/7$ commensurate structure proposed by Elser (5). Red hexagons show the in-plane confinement (see Sect. 6.3.2). . . . .	68
6.7	Transition observed by the Israel Group at a fractional $n = 0.6$ . Figure taken from (3), copyright (1984) by the American Physical Society. Red arrow (marking the transition at 3.6 layers) and labels added for clarity. . . . .	69
6.8	Sketch of a (A) smooth surface, (B) somewhat smooth surface, and (C) rough surface. Some superfluid trapped in the roughness couples to the torsional oscillator motion. . . . .	74
A.1	Nitrogen adsorption isotherm for the grafoil sample. . . . .	77
A.2	BET fit for the grafoil sample. . . . .	78
A.3	Nitrogen adsorption isotherm for the graphene sample. . . . .	79
A.4	BET fit for the graphene sample. . . . .	80
A.5	Grafoil empty cell data. . . . .	81
A.6	Grafoil data as a function of temperature at 0.5 MPa. Used to find $f_L$ . . . . .	82
A.7	Graphene empty cell data. . . . .	82
A.8	Graphene data as a function of temperature at 0.01 MPa. Used to find $f_L$ . . . . .	83
A.9	Grafoil melting 1.6 K isotherm. . . . .	84
A.10	Grafoil melting 1.2 K isotherm. . . . .	84
A.11	Grafoil melting 1.1 K isotherm. . . . .	85

A.12 Grafoil melting 0.9 K isotherm. . . . .	85
A.13 Grafoil melting 0.8 K isotherm. . . . .	86
A.14 Grafoil melting 0.7 K isotherm. . . . .	86
A.15 Grafoil melting 0.6 K isotherm. . . . .	87
A.16 Grafoil melting 0.5 K isotherm. . . . .	87
A.17 Grafoil melting 0.4 K isotherm. . . . .	88
A.18 Grafoil melting 0.2 K isotherm. . . . .	88
A.19 Grafoil melting 0.1 K isotherm. . . . .	89
A.20 Grafoil freezing 1.6 K isotherm. . . . .	90
A.21 Grafoil freezing 1.2 K isotherm. . . . .	90
A.22 Grafoil freezing 0.9 K isotherm. . . . .	91
A.23 Grafoil freezing 0.8 K isotherm. . . . .	91
A.24 Grafoil freezing 0.6 K isotherm. . . . .	92
A.25 Grafoil freezing 0.5 K isotherm. . . . .	92
A.26 Grafoil freezing 0.4 K isotherm. . . . .	93
A.27 Grafoil freezing 0.3 K isotherm. . . . .	93
A.28 Grafoil freezing 0.15 K isotherm. . . . .	94
A.29 Grafoil freezing 0.1 K isotherm. . . . .	94
A.30 Graphene freezing 1.65 K isotherm. . . . .	95
A.31 Graphene freezing 1.15 K isotherm. . . . .	95
A.32 Graphene freezing 1.05 K isotherm. . . . .	96
A.33 Graphene freezing 0.95 K isotherm. . . . .	96
A.34 Graphene freezing 0.8 K isotherm. . . . .	97
A.35 Graphene freezing 0.6 K isotherm. . . . .	97
A.36 Graphene freezing 0.4 K isotherm. . . . .	98
A.37 Graphene freezing 0.2 K isotherm. . . . .	98
A.38 Graphene freezing 0.15 K isotherm. . . . .	99
A.39 Graphene freezing 0.1 K isotherm. . . . .	99
A.40 Tunneling of $^4\text{He}$ into the Grafoil sample as a function of time at 0.8 K. Straight lines are to guide the eye in extrapolating to Time = 48 hours.	100
A.41 Tunneling of $^4\text{He}$ into the Graphene sample as a function of time at 1.0 K. Straight lines are to guide the eye in extrapolating to Time = 48 hours.	101



# 1

## Introduction

Helium is unique because its behavior is dominated by quantum properties at low temperature. Liquid helium-4 ( $^4\text{He}$ ) becomes superfluid at 2.172 K. Solid  $^4\text{He}$  also forms in the low temperature region after pressurization to 2.53 MPa. The superfluid-solid system exhibits special properties that make it ideal for the general study of crystal growth.

The large thermal conductivity, small latent heat, and easy mass transport in the liquid allow systems containing superfluid and solid  $^4\text{He}$  to come to equilibrium in a very short time. At low temperatures, solid  $^4\text{He}$  can grow and melt so quickly that crystallization waves can be observed (6). Faceting in  $^4\text{He}$  crystals has been theorized and studied (1). Below a certain temperature, called the roughening temperature  $T_R$ , rough crystal surfaces become smooth facets. This notion was originally predicted by Landau in 1949 (7) and evolved into the modern theory of roughening, whose first solutions came from Chui and Weeks in 1978 (8).

When immersed in liquid  $^4\text{He}$ , solid  $^4\text{He}$  is known to grow epitaxially on graphite well below the bulk solidification pressure  $P_s$  (9). As the pressure of the superfluid  $P$  increases, the thickness of the adsorbed solid also increases. Theoretically, as a consequence of the same factors that lead to crystal roughening (10), the growth of  $^4\text{He}$  crystals on graphite below  $T_R$  is thought to become discontinuous with pressure and show discontinuous jumps in the adsorbed solid as one whole smooth layer forms before the next begins.

Experiments in search of these layering transitions have been performed primarily by two groups: one from Pennsylvania State University (2; 4; 11) and one from Israel (3; 12). From here on, these two groups are referred to as the “**Penn. State Group**” and the “**Israel Group**.” The Penn. State Group used the fourth sound technique and observed sharp minima in the sound velocity occurring once per solid layer at each half layer. The Israel Group used a differential adsorption technique and saw mostly

continuous solid growth punctuated by small kinks at the completion of each layer. Furthermore, the Penn. State Group saw an additional fourth sound minimum during each layer below 0.95 K. They supposed this signaled that each layer grew in, not one, but two stages.

It seems to us that the above experiments indicate layer-by-layer solid adsorption. But, the sharp fourth sound minima seem to indicate much more discontinuous growth than the smooth adsorption isotherms of the Israel Group's data. The location of the transition (half or whole layer number) is also in dispute.

The experiments have also shown the growth of solid  $^4\text{He}$  on graphite below 0.95 K to be more complex than the growth above 0.95 K. However, the observation of two-stage layering made by the Penn. State Group has, to our knowledge, never been confirmed and the cause of the two stages is still unclear. From the fourth sound data alone, it seems difficult to know how much solid grows in each stage or even that the secondary stage is not the growth of an additional solid layer.

This thesis presents two torsional oscillator studies: one for the growth of solid  $^4\text{He}$  on grafoil, an exfoliated graphite used by both the Penn. State Group and the Israel Group, and another on graphene. Throughout the course of this thesis, these two experiments are referred to as the “**grafoil**” and “**graphene**” experiments.

The grafoil measurements show shifts in the oscillation frequency and patterns of energy dissipation. Using the known surface area of the grafoil sample, changes in oscillation frequency are converted to a changes in the amount of adsorbed solid. These measurements rectify some of the differences observed between the Penn. State and Israel groups' findings. From 0.9 K and below, the grafoil measurements confirm the two-stage layering seen by the Penn. State Group and reveal that there are indeed two stages in the formation of one layer rather than the growth of two layers. Carrying out these measurements to 0.1 K has revealed a new and interesting aspect of solid  $^4\text{He}$  adsorbed on grafoil: at low temperature, there is less solid on the substrate. Although the theory (10; 13) of layering transitions calls for step-like discontinuities, solid growth on grafoil is seen to be mostly continuous, punctuated by a series of small kinks in the adsorption isotherms.

The above observations lead us to believe that the growth of solid  $^4\text{He}$  on grafoil is heavily influenced by the unideal nature of the substrate. The individual graphite platelets have diameters on the order of tens of nm (14; 15) and are assembled in a tortuous pore structure made of large voids connected by narrow necks (16). In an effort to find a more ideal substrate, we performed the graphene experiment. The sample was multilayer graphene with individual platelet diameters on the  $\mu\text{m}$  order, which is much larger than grafoil.

---

The graphene measurements show much more discontinuous solid growth. The isotherms contain extended flat areas separated by jumps in the amount of adsorbed solid. Surprisingly, in contrast with the theory of layering transitions, five discontinuities, each coincident with energy dissipation, are observed during the growth of a single layer. As the temperature is lowered, these discontinuities and the accompanying energy dissipation peaks become sharper. We propose a scenario in which the uppermost layer grows through a series of two-dimensional (2D) commensurate and incommensurate structures. Calculations of the internal energy difference between the commensurate phases reproduces the pressure differences of the superfluid between the phases. These novel results suggest that the growth of solid  $^4\text{He}$  on graphene is more complicated than simple layer-by-layer growth. Furthermore, the jumps in solid coverage are preceded by dips and overshoots.

The outline of this thesis is as follows. Chapter 2 provides a theoretical overview of relevant concepts and presents some related experimental results. Chapter 3 gives a detailed explanation of the apparatus and procedure for data acquisition. Chapter 4 presents the method used to analyze the data. Chapter 5 discusses the grafoil results. Comparison of the grafoil data to the Penn. State and Israel groups is made. Chapter 6 discusses the graphene results. A scenario in which the adsorbed solid grows through a series of 2D transitions is proposed. Chapter 7 is a summary and concluding remarks.



## 2

# Theoretical and Experimental Overview

This chapter provides an overview of the concepts and existing experimental results relevant to this thesis.

## 2.1 $^4\text{He}$ Phase Diagram

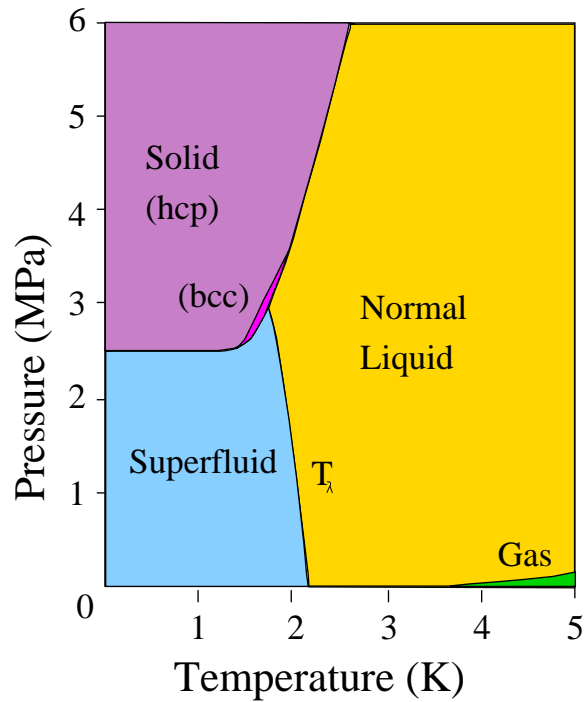


**Fig. 2.1:** Phase diagram for  $^4\text{He}$  at low temperature. Figure taken from (1), copyright (2005) by the American Physical Society.

Helium is the second lightest and second most abundant element in the known universe. Due to its large zero point motion, Helium is the only element which does not solidify under its own vapor pressure; it is a quantum fluid even at zero temperature. The most abundant isotope,  $^4\text{He}$ , becomes superfluid below a critical temperature  $T_\lambda$ . The solid phase of  $^4\text{He}$  only forms at sufficiently high pressure.

The phase diagram in Fig. 2.1 shows  $T_\lambda = 2.172$  K, where  $^4\text{He}$  transitions from a regular liquid (He I) to a superfluid (He II). At a pressure of 2.53 MPa (17),  $^4\text{He}$  can solidify.

### 2.1.1 Superfluid $^4\text{He}$

Superfluidity is a macroscopic quantum phenomenon in which a large fraction of particles become locked in the ground state. This Bose condensate is characterized by very fast mass and heat transport and zero measurable viscosity. Elementary excitations of the superfluid are characterized by the dispersion relation (18). Low wave vector excitations are known as phonons. At higher wave vector, the dispersion relation shows a minimum whose particles are known as rotons. As the temperature of the superfluid is lowered, the energy required to excite rotons increases and very few exist below 0.8 K.

### 2.1.2 Solid $^4\text{He}$

As stated previously, superfluid  $^4\text{He}$  will solidify at a pressure  $P_s = 2.53$  MPa. Bulk solid  $^4\text{He}$  is known to form in both b.c.c. (body centered cubic) and h.c.p. (hexagonal closest packing) crystal structures, depending on pressure and temperature, as shown in Fig. 2.1. The solid density near  $P_s$  is 0.19 g/cc (19), corresponding to a lattice constant of 3.66 Å. Since the liquid-solid transition in  $^4\text{He}$  is discontinuous, there is an energy barrier to crystallization. In a pure  $^4\text{He}$  system, overcoming the barrier often requires over pressurization (above the bulk solidification pressure) of a few mbar.

The unique quantum properties of superfluid  $^4\text{He}$  make systems containing both solid and superfluid especially interesting. These systems exhibit rapid equilibrium and solid growth rates, producing crystallization waves (20), which are not realized in other materials.

## 2.2 The Roughening Transition

The surface of  $^4\text{He}$  crystals have been intensely studied in theory and experiment (1). One point of much interest has been the roughening transition. There are two opposing factors which determine the smoothness of the crystal surface: the underlying lattice potential and thermal excitations of surface defects or adatoms. At low temperatures,

thermal excitations are suppressed and the lattice potential pins the surface at integer values of the lattice constant, making the surface is smooth and faceted. As the temperature increases, the surface becomes rough as it is covered by step, kink, and other defects. Facets were first observed at the surface of  $^4\text{He}$  crystals by Landau et. al. in 1980 (21). As the temperature is lowered, several different facets are known to appear on  $^4\text{He}$ . In total, 4 facets have been observed experimentally, the only one of interest to this thesis is the c-facet.

The temperature below which the surface transitions from a rough state to a smooth one is known as the roughening temperature  $T_R$ , and was derived by Fisher and Weeks (22) and Nozieres (23). An overview of the Fisher and Weeks derivation follows. It should be noted that the notion of surface roughness is defined macroscopically rather than microscopically.

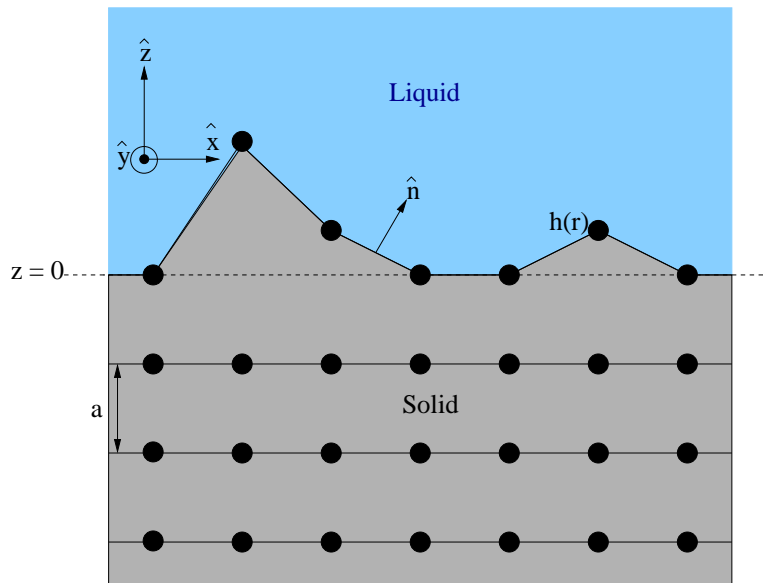


Fig. 2.2: Sketch of the liquid-solid interface.

Consider a solid-liquid interface which is a crystalline plane with rational Miller Indices, as shown in Fig. 2.2. The equilibrium position of each point (atom) on the surface is located at  $z = 0$  and the vertical displacement of the surface from equilibrium is given by the function  $h(\vec{r})$ . For long wavelength, small surface distortions, a quantity called the surface stiffness is given by

$$\Gamma_i = \gamma(\hat{z}) + \partial^2 \gamma / \partial \hat{n}_i \partial \hat{n}_i |_{\hat{n}=\hat{z}}, \quad (2.1)$$

where  $\gamma$  is the surface tension and  $i = \hat{x}, \hat{y}$  can be chosen for convenience. There may in general be higher order derivatives of  $\gamma$ , but they are neglected for small surface

distortions. Also,  $\Gamma$  is given as a continuous function of position, which is justified for long wavelength distortions. The free energy of the interface can then be written as

$$F = \frac{1}{2} \int dr^2 [\gamma_x (\partial_x h)^2 + \gamma_y (\partial_y h)^2]. \quad (2.2)$$

To show that the interface is smooth below a certain temperature, Fisher and Weeks prove a contradiction by supposing that the interface is rough for all temperatures. The roughness, which consists of thermal and quantum fluctuations of the interface, can be characterized by a series of crystallization waves with wave vector  $\vec{q}$ . The hamiltonian can then be written as

$$H = \frac{1}{2} \int_{\vec{q}} [\pi_{\vec{q}} \pi_{-\vec{q}} / m_{\vec{q}} + K_{\vec{q}} h_{\vec{q}} h_{-\vec{q}}], \quad (2.3)$$

where  $\pi_{\vec{q}}$  is the momentum conjugate of the fourier transform,  $m_{\vec{q}} = (\rho_s - \rho_l)^2 / q \rho_l$  is the effective mass of a wave (with  $\rho_s$  the density of solid and  $\rho_l$  the density of liquid), and  $K_{\vec{q}}$  is the force constant given by

$$K_{\vec{q}} = \Gamma_x q_x^2 + \Gamma_y q_y^2 = \omega_{\vec{q}}^2 m_{\vec{q}}. \quad (2.4)$$

The mean square fluctuations of the interface are written as

$$\begin{aligned} \langle h^2(\vec{r}) \rangle &= \int_{\vec{q}} \langle h_{\vec{q}} h_{-\vec{q}} \rangle \\ &= \int_{\vec{q}} \frac{\hbar \omega_{\vec{q}}}{2K_{\vec{q}}} \left( \frac{\exp(\hbar \omega_{\vec{q}}/T) + 1}{\exp(\hbar \omega_{\vec{q}}/T) - 1} \right) \\ &= \int_{\vec{q}} \frac{\hbar \omega_{\vec{q}}}{K_{\vec{q}}} \left( \frac{1}{\exp(\hbar \omega_{\vec{q}}/T) - 1} + \frac{1}{2} \right). \end{aligned} \quad (2.5)$$

At  $T = 0$ , the fluctuations become

$$\begin{aligned} \langle h^2(\vec{r}) \rangle &= \int_{\vec{q}} \frac{\hbar \omega_{\vec{q}}}{2K_{\vec{q}}} \\ &= \int_{\vec{q}} \frac{\hbar}{2m_{\vec{q}} K_{\vec{q}}} \\ &\sim \int_{\vec{q}} \frac{1}{\vec{q}}, \end{aligned} \quad (2.6)$$

which is finite. Thus, the assumed rough interface has a finite width even at  $T = 0$ . The last integral in Eq. 2.6 is convergent for long wavelengths.

The full interface hamiltonian can be written in the form

$$H = \int d^2 r \left[ \frac{J}{2} |\vec{\nabla} h(\vec{r})|^2 + V(h(\vec{r})) \right], \quad (2.7)$$

where higher order derivatives of  $h(\vec{r})$  have been neglected for long wavelengths. Fisher and Weeks argue that because the rough interface has a finite width,  $V(h(\vec{r}))$  will in

general have a term of the form  $-y_0[\cos(2\pi h(\vec{r})/a)]$ ,  $y_0 > 0$ , which is the periodic potential of the underlying lattice. The cosine reaches its maximum value when  $h(\vec{r})$  is an integer multiple of the lattice constant  $a$ . Therefore the above term provides a preference for the solid surface to locate at integer multiples of  $a$ . The term has an eigen value, found by group-renormalization (8)

$$\lambda = 2 - \frac{\pi T}{a^2(\Gamma_x \Gamma_y)^{1/2}}. \quad (2.8)$$

If  $T$  is less than the value

$$T_R = \frac{2a^2}{\pi}(\Gamma_x \Gamma_y)^{1/2}, \quad (2.9)$$

then the cosine term becomes relevant to the interface hamiltonian and for large enough  $y_0$ , can force the interface to integer multiples of  $a$ . In other words, the lattice potential confines fluctuations of the interface, making the surface smooth. Equation 2.9 is known as the universal roughening relation.

The most detailed studies of roughening have been performed for  $^4\text{He}$  h.c.p. crystals. Three transitions are known to occur at 1.3 K (0001 face or c-facet), 1.0 K (1010 face), and 0.4 K (1011 face) (24). Lower numbered crystal planes have smaller spacing and therefore more sharply varying lattice potentials, making it easier to pin the surface (as discussed previously), thus resulting in higher  $T_R$ . For a more complete review of roughening experiments in  $^4\text{He}$  see, for example (24).

## 2.3 Epitaxial Growth of Solid $^4\text{He}$ on Graphite from the Superfluid

Bulk solid forms at  $P_s = 2.53$  MPa, but when immersed in liquid  $^4\text{He}$ , solid  $^4\text{He}$  is known to grow epitaxially on graphite even below  $P_s$  (9). Solid  $^4\text{He}$  does not grow epitaxially on all substrates, making the  $^4\text{He}$ -graphite system special. The large hexagonal van der Waals potential of the graphite, which matches the h.c.p. symmetry of solid  $^4\text{He}$ , acts to increase the effective liquid pressure near the substrate beyond  $P_s$ , thus allowing solidification of h.c.p.  $^4\text{He}$ .

### 2.3.1 Continuous Growth: the Franchetti Relation

The Franchetti Relation (25) is a simple way to relate the liquid pressure and the number of adsorbed solid layers on a substrate  $\theta_F$ . To derive the relation, consider a liquid and a flat substrate as sketched in Fig. 2.3. The liquid pressure far from the substrate  $P$  is different from the pressure close to the substrate  $P_z$ , because of the substrate's attractive van der Waals field given by  $U(z) = -\alpha/z^3$ . Here  $\alpha$  is the van

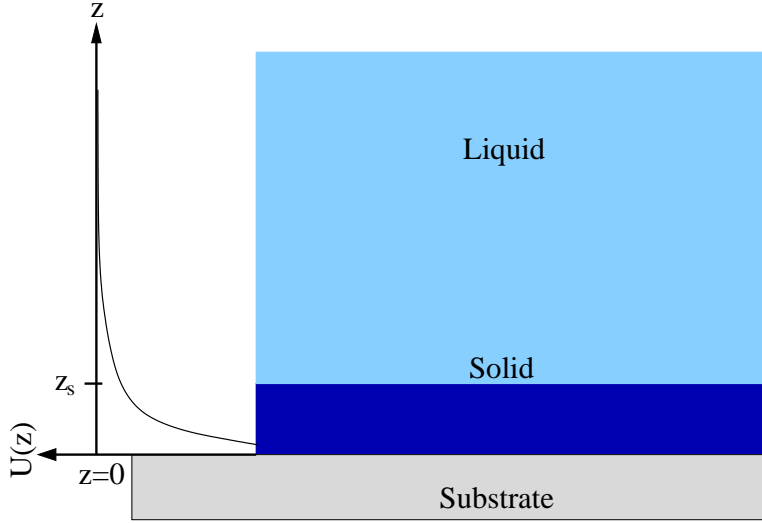


**Fig. 2.3:** Sketch of solid adsorbed on a substrate under the Franchetti Relation.

der Waals constant and  $z$  is the distance from the substrate. The van der Waals force acts to increase the pressure of the liquid near the substrate, resulting in a pressure

$$\begin{aligned} P(z) &= P + \int_z^\infty \frac{\rho(z')}{m} \frac{dU}{dz'} dz' \\ &= P + \frac{\rho_l}{m} U(z), \end{aligned} \quad (2.10)$$

with  $m$  the mass of a liquid molecule,  $\rho(z)$  the local liquid density, and  $\rho_l$  the average liquid density. If the van der Waals attraction increases the liquid pressure beyond  $P_s$ , solid will form. Assuming the edge of the solid is the point where  $P(z_s) = P_s$ , the coverage in number of layers is found:

$$\begin{aligned} P_s = P(z_s) &= P + \frac{\rho_l}{m} \frac{\alpha}{z_s^3} \\ \theta_F = \frac{z_s}{h_0} &= \left( \frac{\rho_l \alpha}{m h_0^3} \right)^{1/3} (P_s - P)^{-1/3}. \end{aligned} \quad (2.11)$$

The height of a single solid layer is given by the constant  $h_0$ . Substituting known values for the constants  $\rho_l$ ,  $\alpha$ ,  $m$ , and  $h_0$ ,  $^4\text{He}$  and graphite results in the equation (11)

$$\theta_F = \frac{6.7}{(P_s - P)^{1/3}}. \quad (2.12)$$

From the Franchetti Relation, it is seen that as  $P$  increases, the number of adsorbed solid layers also increases, and diverges as  $P_s$  is approached (bulk solid grows from the substrate surface). The Franchetti Relation assumes constant growth, which is true for a rough crystal surface (i.e. true above  $T_R$ ).

### 2.3.2 Discontinuous Growth: Layering Transitions

As a consequence of the same factors that lead to crystal roughening, the growth well below  $T_R$  is expected to become discontinuous with pressure, as the solid grows discontinuously via a series of whole layer steps known as layering transitions. For a detailed derivation of layering transitions, the reader is referred to Huse (10).

In layering transitions, as in roughening, there is a competition between the underlying lattice potential and thermal fluctuations. When the underlying potential is able to pin the lattice at integer values of  $a$ , the surface of the solid is smooth and additional  $^4\text{He}$  is adsorbed in whole layers, each remaining smooth as  $P$  is increased until the next layer is formed. At the atomic level, the formation of a new layer can be thought to start with the accumulation of adatoms on the surface of an already completed layer. However, nucleation on a smooth surface is more difficult than nucleation on a rough surface and accomplished only after overcoming a significant potential barrier. Thus, just after the completion of a layer, an initial increase in pressure results in no new solid formation. When the pressure becomes great enough, the chemical potential between the solid and liquid phases increases to a level that can support the nucleation and expansion of adatom clusters. As clusters form, the potential barrier decreases, leading to a flood of nucleation which results in a new smooth layer.

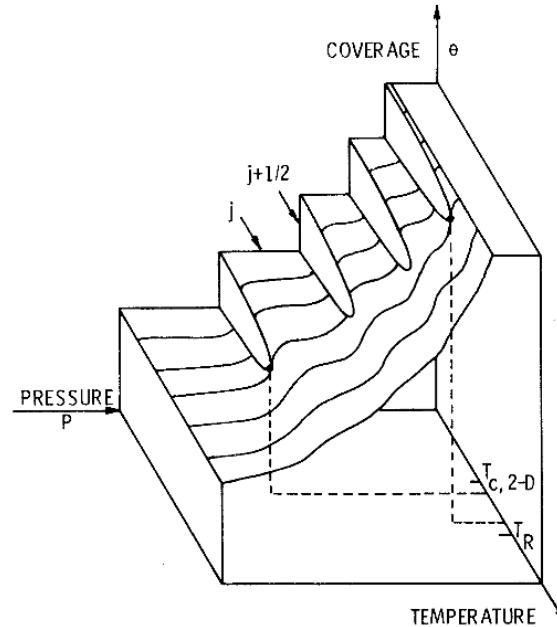


**Fig. 2.4:** Sketch of layering transitions showing  $T_{c,n}$  becoming lower with lower layer number. Figure taken from (2), copyright (1984) by the American Physical Society.

To be precise, each layer has its own critical temperature  $T_{c,n}$ , below which that

layer grows discontinuously, where the layer number is represented by  $n$ . A sketch of this behavior is shown in Fig. 2.4. This is because both the substrate potential and underlying  $^4\text{He}$  lattice potential act on the surface. Huse showed that  $T_{c,n}$  and  $T_R$  are related. Starting with a similar interface hamiltonian to Fisher and Weeks (Eq. 2.7),  $V(h)$  is given by

$$V(h(\vec{r})) = y_0 \cos(2\pi h(\vec{r})) + ch(\vec{r})^{-2} + \Delta f h(\vec{r}). \quad (2.13)$$

Here,  $ch(\vec{r})^{-2}$  takes into account the van der Waals attraction of the substrate and  $\Delta f$  is the difference in free energy per unit volume between the solid and liquid phases of  $^4\text{He}$ . The periodic lattice potential is the same as that of Fisher and Weeks.

The result of renormalization group analysis using the above potential is that

$$T_R - T_{c,n} \sim 1/\ln^2(n). \quad (2.14)$$

That is, the critical layering temperature for small  $n$  is less than  $T_R$  and increases with  $n$ , eventually approaching  $T_R$  for large  $n$ . Fluctuations of the interface are confined by the substrate more vigorously at lower layer number; at higher layer numbers, both tall (multi-atom in height) and short surface defects can form, but at lower layer numbers, only short defects are allowed. At a certain temperature this results in rougher surfaces at lower layer numbers and thus lower  $T_{c,n}$ . On the other hand, when there is a large number of adsorbed layers, the substrate potential on the interface is weak and layers are governed by the usual roughening transition:  $T_{c,n} \rightarrow T_R$ .

### 2.3.3 Experimental Studies of Layering Transitions in Solid $^4\text{He}$ on Grafoil

Experiments in search of layering transitions in solid  $^4\text{He}$  adsorbed on grafoil, an exfoliated graphite, have been performed by two groups: one from Pennsylvania State University (Penn. State University) (2; 4; 11) and one from Israel (3; 12). The substrate structure of grafoil is far from ideal with average platelet diameters on the order of tens of nm (14; 15), and a pore structure made of large voids connected by narrow necks (16). Figure 2.5 shows a sketch of the grafoil pore structure.

The Penn. State Group used fourth sound measurements to study layering transitions. Fourth sound is a wave that propagates in the superfluid (as opposed to first sound, which propagates in the normal fluid). The Penn. State Group observed sharp periodic dips in the fourth sound velocity as the liquid pressure was increased. Some of their observations are shown in Fig. 2.6. Under their model, the fourth sound velocity propagating through the grafoil-helium system is related to solid growth by

$$C \simeq C_4 \left( 1 - \Gamma \frac{\partial \theta}{\partial P} \right), \quad (2.15)$$

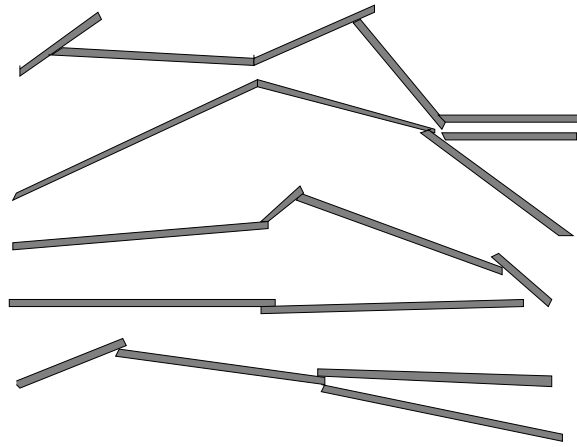


**Fig. 2.5:** Sketch of the tortuous grafoil structure made of many individual graphite sheets.

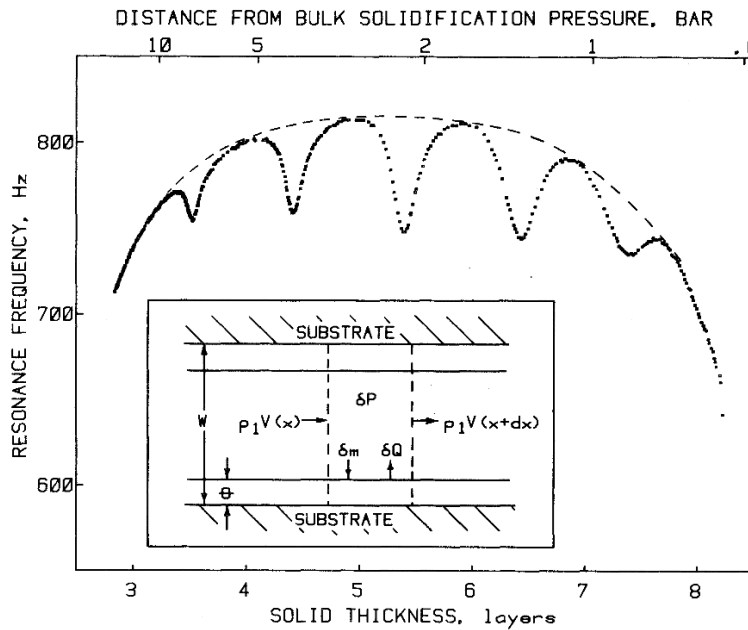


**Fig. 2.6:** Penn. State Group's observations using the fourth sound method. Fourth sound minima occur at approximately half integer Franchetti numbers (horizontal axis). Figure taken from (2), copyright (1984) by the American Physical Society.

where the constant  $\Gamma = \Delta\rho C_1^2 a/w$ ,  $\theta$  is the number of adsorbed solid layers,  $\Delta\rho$  is the difference in solid and liquid densities,  $C_1$  is the first sound velocity,  $a$  is the solid helium lattice constant, and  $w$  is the average separations between graphite planes. From this equation, minima in the fourth sound velocity correspond to maxima in the solid growth rate. After converting  $P$  to  $\theta_F$ , they observed that the minima occurred at each half-integer Franchetti number, and thus inferred the observation of layering

transitions.

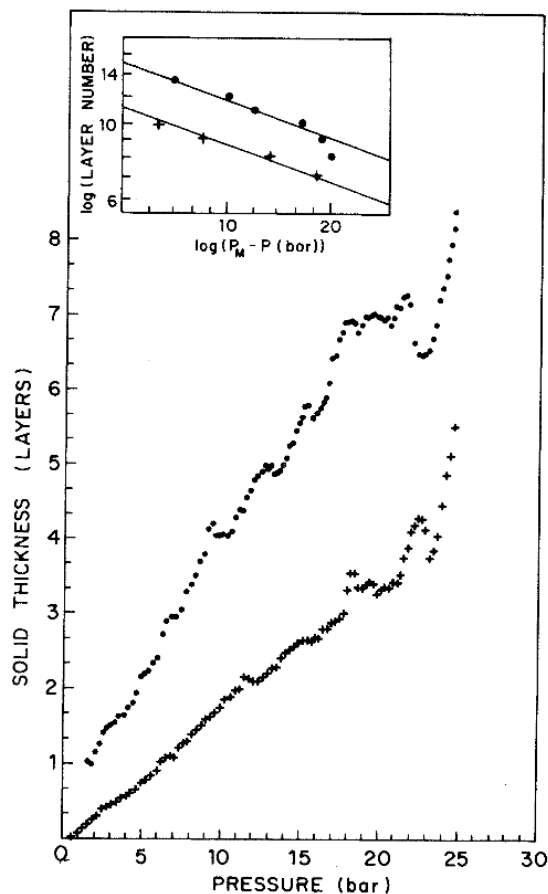


**Fig. 2.7:** Israel Group's adsorption isotherms. Kinks occur at approximately whole integer layer number (vertical axis). Figure taken from (3), copyright (1984) by the American Physical Society.

The Israel Group studied layering transitions in  $^4\text{He}$  using a differential adsorption technique. By knowing the amount of  $^4\text{He}$  extracted from a cell and the corresponding pressure, they could calculate the change in the number of adsorbed solid layers. Their results, in Fig. 2.7, showed a mostly smooth change in the number of adsorbed solid layers punctuated by small kinks at the completion of each layer.

Later, the Penn. State Group (4) observed what they believed to be two-stage layering transitions below 0.95 K. Their observations are shown in Fig. 2.8. Additional minima in the fourth sound velocity occurring before (on the low pressure side of) each established layering transition. The additional minima was assumed to be an additional stage in the formation of each layer. Two possible explanations were put forth. One was that each layer undergoes a 2D phase transition such as a structural reorganization. The other was the difference between kink and step surface defects.

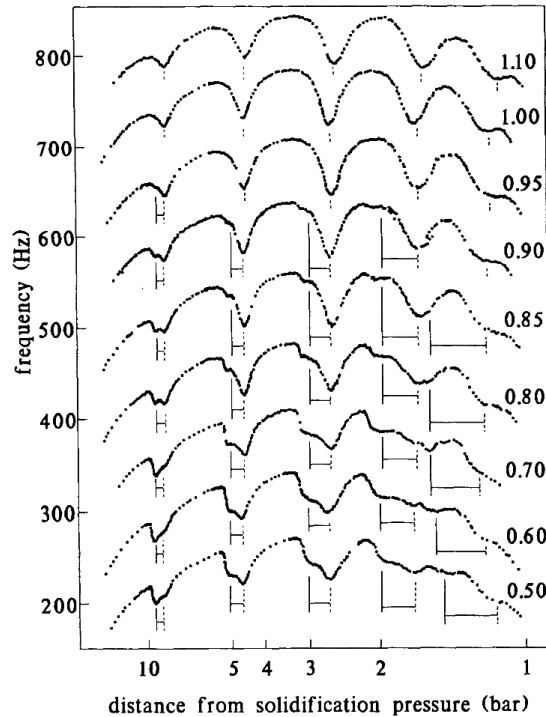


**Fig. 2.8:** Penn. State Group’s observation of two-stage layering transitions. Additional fourth sound minima are seen on the low pressure side of each established transition below 0.95 K. Horizontal lines connected by vertical bars mark the quantity  $P_{\text{step},n} - P_{\text{kink},n}$ . Figure taken from (4), copyright (1992) by the American Physical Society.

They explained the difference between kink and step sites as follows. The start of each new layer begins with the nucleation surface defects. As the pressure increases, atoms bind to those defects and expand to form the next layer. Suppose that there are two types of defects, kinks and steps, as drawn in Fig. 2.9. An additional adsorbed atom forms more bonds at a kink site than at a step site. Thus, it is easier to adsorb atoms to kink sites. This means that kink sites can expand at lower pressure than step sites. As the kinks start to expand, the fourth sound velocity decreases, causing the first minimum. At a higher pressure, step sites also start expanding, causing the second observed minimum.

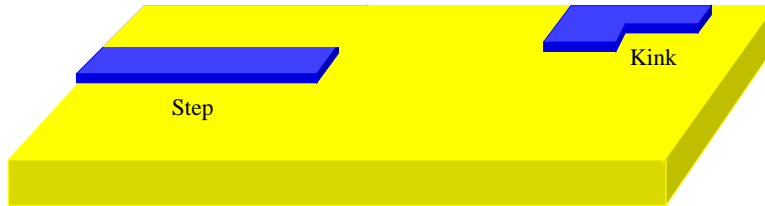


**Fig. 2.9:** Sketch of kink and step surface defects.

The Penn. State Group theorized a relationship between the pressures of kink and step expansion. The average deviation (in thickness) from an integer layer number  $n$ , is given by a power law  $(\theta_F - n)^\beta$  (26).  $\beta$  is the critical cluster size. Classical atomic nucleation theory says that the concentration of clusters on a surface is proportional to  $\exp(E_i/k_B T)$ , where  $E_i$  is the energy of a cluster with  $i$  atoms (27). Since the concentration of clusters is proportional to the thickness of an incomplete layer,

$$\theta - n = (\theta_F - n)^\beta \quad (2.16)$$

$$\propto \exp(E_i/k_B T). \quad (2.17)$$

Using the Franchetti Relation for  $\theta_F$ , the pressure can be related to the average deviation from an integer layer number.

$$\begin{aligned} \theta - n &= \left( \frac{\alpha}{(P_s - P)^{1/3}} - n \right)^\beta \\ \frac{\alpha}{(P_s - P)^{1/3}} &= x^{1/\beta} + n \\ P_s - P &= \frac{\alpha^3}{n^3} \left( 1 + \frac{(\theta - n)^{1/\beta}}{n} \right)^{-3}. \end{aligned} \quad (2.18)$$

Using Eq. 2.17, eq. 2.18, and heavy simplification, the Penn. State Group writes a non-rigorous expression for the pressure difference in their two-stage layering observation.

$$\begin{aligned} P_{\text{step},n} - P_{\text{kink},n} &= (P_s - P_{\text{kink},n}) - (P_s - P_{\text{step},n}) \\ &\propto e^{\frac{U_n}{\beta k_B T}} \left( e^{\frac{E_{\text{kink}}}{\beta k_B T}} - e^{\frac{E_{\text{step}}}{\beta k_B T}} \right), \end{aligned} \quad (2.19)$$

where the van der Waals energy is given by  $U_n = \frac{m\alpha}{\rho n^3} = \frac{m}{\rho}(P_s - P_{\text{step},n})$ . They make further simplifications to Eq. 2.19 by using  $T = T_R$  and assuming that  $\beta = 2$  at  $T_R$ . The critical cluster size is often on the order of a few atoms (28). These simplifications result in the expression

$$P_{\text{step},n} - P_{\text{kink},n} = P_0 \exp(U_n/2k_B T_R), \quad (2.20)$$

which has only one adjustable parameter,  $P_0$ , found from fitting the data to be  $0.2 \pm 0.04$  bar. One important thing to note is that this kink-step model implies a constant pressure difference between kink and step expansion in each layer as a function of temperature. Horizontal lines connecting vertical bars show the quantity  $P_{\text{step},n} - P_{\text{kink},n}$  in Fig. 2.8. This simple model approximately agreed with the fourth sound data.

The experiments on grafoil seem to imply layer-by-layer growth of solid  $^4\text{He}$  from the superfluid phase. However, the sharp minima observed in the fourth sound imply

much more discontinuous growth than observed with the differential adsorption method. Also, whether the transitions occur at half or whole integer numbers is in dispute.

The results from both groups agree that the growth of solid  $^4\text{He}$  is more complex below 0.95 K, but two-stage layering was, to our knowledge, never confirmed and the cause of the two stages is still unclear. From the fourth sound data alone it is difficult to know how much solid grows in each stage or even that the additional stage is not the growth of another whole layer.

## 2.4 $^4\text{He}$ Adsorption on Graphite and Graphene from the Gas Phase

Although the solid growth/melting experiments for this thesis were performed from the superfluid phase, information contained in experiments performed in the thin film region (adsorption from the gas phase) is useful for understanding our results. Also, some connections to experiments and theory for  $^4\text{He}$  adsorption from the gas phase are made in the discussion. We briefly state some useful information here.

### 2.4.1 $^4\text{He}$ on Graphite

Many experiments and much theoretical work has been performed for the adsorption of thin  $^4\text{He}$  films on graphite. Torsional oscillator (29) and neutron diffraction (30) experiments have shown the first two layers to be solid, with the third and higher layers adsorbed liquid. The first two solid layers have a very rich phase diagram, undergoing various 2D phase transitions as more  $^4\text{He}$  atoms are adsorbed. In the first layer, for example, the solid is first a commensurate  $1/3$  solid, undergoes a transition at a filling of approximately 0.6 layers to a domain-wall phase, and then at nearly  $3/4$  layer transitions to an incommensurate solid (31). Atoms are promoted into the second layer starting at a density of  $0.12 \text{ \AA}^{-2}$ , a value which is considerably more dense than that of bulk solid,  $0.087 \text{ \AA}^{-2}$  (calculated from the bulk lattice constant). Completion of the second layer, however, was observed to occur at a second layer density of  $0.092 \text{ \AA}^{-2}$  (32), which is only slightly larger than that of bulk solid.

### 2.4.2 $^4\text{He}$ on Graphene

To our knowledge, no experiments have been performed for thin film  $^4\text{He}$  on graphene substrates. But, much theoretical work has been done using computer simulation. Graphite is a stack of many graphene sheets with  $3.35 \text{ \AA}$  inter planar spacing and the usual ABAB stacking. The adsorption potential for graphene is about 10% weaker

than graphite (33). Despite this difference, simulations have shown qualitatively similar phase diagrams for the first two layers of  $^4\text{He}$  adsorbed on graphene (34; 35). Commensurate-incommensurate phase transitions and domain wall phases are still expected to exist. Differences due to the adsorption potential seem to be largest in the low density region (below 1 layer) (35).

# 3

## Experimental Method and Apparatus

Both the grafoil and graphene measurements utilized the torsional oscillator method. The oscillator was cooled with a dilution refrigerator. Temperatures studied were from 1.65 K to 0.1 K. This chapter first discusses the theory of the torsional oscillator method, followed by the experimental setup and procedure used in the grafoil and graphene measurements. Basically, both experiments used many of the same parts; the torsional oscillators and samples were the main differences.

### 3.1 Theory of the Torsional Oscillator Method

Here, a brief overview of the torsional oscillator method is presented. For a more detailed discussion, the reader is referred to, for example (36; 37). A torsional oscillator is a mechanical resonator that is used as a very sensitive balance. Figure 3.1 shows a sketch of the torsional oscillator method. The torsion mass is connected to and resonates at one end of a torsion rod, which provides the restoring force. The torsion mass contains the experimental sample under investigation. By preparing an oscillator with high quality factor, very small changes in the moment of inertia of the sample can be detected.

#### 3.1.1 Drive and Detection

The oscillation is driven and detected by electrodes that form two capacitive transducers. One electrode supplies a driving force while the other detects the oscillator's response. As Fig. 3.1 shows, they are coupled through a center electrode that is mounted on but electrically insulated from the torsional mass. The center electrode moves with the torsional mass and is therefore often called the movable electrode. The two other

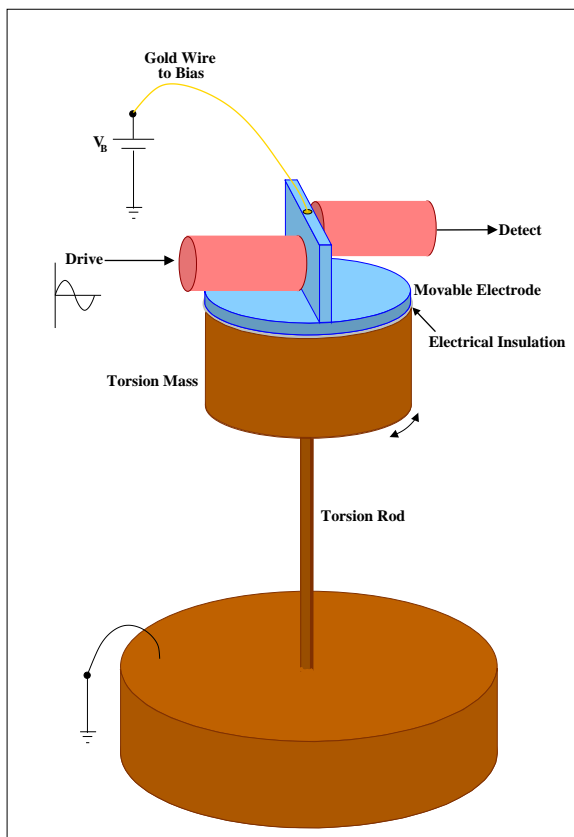


**Fig. 3.1:** Sketch of the torsional oscillator method.

electrodes (for drive and detection) are unmovable and, in the case of this thesis, fixed with a special holder (see sect. 3.3.2). A periodic signal is applied by the drive electrode that results in a torque and subsequent oscillation that is detected by the detection electrode.

The movable electrode is often biased to improve the oscillator's response. With no biasing, the force exerted by the drive capacitance is given by the usual relationship,  $F = CV^2/2d$ , which is not linear with respect to the voltage of the drive signal. By adding a large enough bias, the voltage range of the drive signal becomes relatively small compared with the absolute voltage (given mostly by the bias). Thus, the exerted force becomes almost linear with respect to the driving voltage.

#### 3.1.2 Resonant Modes

If the torsional oscillator is treated as a simple harmonic oscillator, then the equation of motion is

$$I \frac{d^2\theta}{dt^2} = -\kappa\theta, \quad (3.1)$$

where  $I$  is the moment of inertia and  $\kappa$  is the spring constant of the torsion rod. The resonant frequencies are given by

$$\omega = (\kappa/I)^{1/2}. \quad (3.2)$$

For a simple flat-disk torsion mass of uniform density, there are two main modes: torsional and floppy. These modes, sketched in Fig. 3.2, have frequencies that can be found using equation 3.2 and the following:

$$\begin{aligned} \text{torsional mode } I &= (\rho\pi r^2 h)r^2/2 \\ \kappa &= \pi G a^4/32L \\ \text{floppy mode } I &= (\rho\pi r^2 h)[(L + h/2)^2 + r^2/4 + h^2/12] \\ \kappa &= 3\pi E a^4/64L. \end{aligned} \quad (3.3)$$

Here  $\rho$  is the density of the disk,  $G$  is the shear modulus of the torsion rod,  $E$  is the Young's modulus of the rod,  $r$  and  $h$  are the radius and height of the flat disk respectively, and  $a$  is the radius of the torsion rod (36). The torsional mode, or rather,

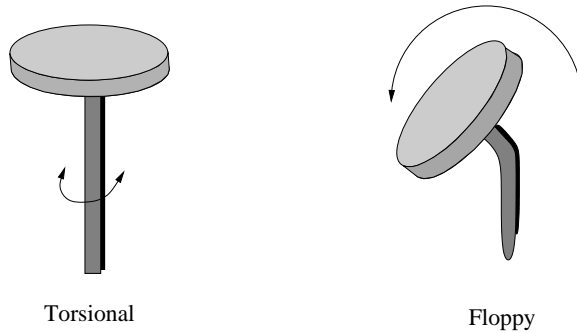


Fig. 3.2: Sketch of torsional and floppy modes in simple harmonic oscillator.

changes in the its resonant frequency are used to make measurements.

In this experiment, a hole in the torsion rod (see section 3.2) functioned as the  $^4\text{He}$  fill line. This inlet allowed  $^4\text{He}$  to enter the sample space. Thus, the equation for the torsional mode  $\kappa$  becomes

$$\kappa = \pi G(a_{outer}^4 - a_{inner}^4)/32L \quad (3.4)$$

For the more complex oscillator used in this experiment,  $I$  is the sum of the various rotational inertia's of the components comprising the torsional mass.

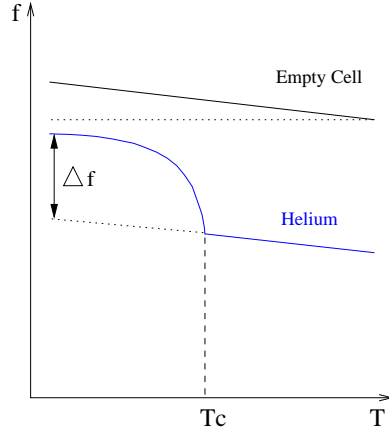


**Fig. 3.3:** Sketch of typical torsional oscillator frequency response of an empty cell and a  ${}^4\text{He}$  filled cell as a function of temperature.

### 3.1.3 Frequency Shifts

Two parameters are important during measurement: resonant frequency and detection signal amplitude. From Eq. 3.2, it is clear that the resonant frequency changes with  $\kappa$ . For example, as the oscillator is cooled, the stiffness of the torsion rod increases and so the frequency also increases. This frequency dependence is often called the “empty cell” behavior. The frequency is also affected by changes in the rotational inertia of the sample (the torsion mass). The observed change in inertia is often referred to as the non-classical rotational inertia. By closely monitoring the resonant frequency and its changes (as they differ from the empty cell), the sample behavior can be characterized under various conditions.

As an example, consider a cell as it is filled with liquid  ${}^4\text{He}$  above  $T_\lambda$ . The inertia increases compared to the empty cell, decreasing the resonant frequency. When the helium is cooled below  $T_\lambda$  and becomes superfluid, it decouples from the oscillation. The classical rotational inertia measured by the oscillator decreases and the frequency increases. This scenario is sketched in Fig. 3.3. In this example, the change in frequency,  $\Delta f$ , can be related to the fraction of superfluid helium by

$$\begin{aligned}
 \Delta f(T) &= \frac{1}{2\pi} \left( \sqrt{\frac{\kappa}{I_{\text{cell}} + I_{\text{He}} \left(1 - \frac{\rho_s(T)}{\rho}\right)}} - \sqrt{\frac{\kappa}{I_{\text{cell}} + I_{\text{He}}}} \right) \\
 &= \frac{1}{2\pi} \sqrt{\frac{\kappa}{I_{\text{cell}}}} \left( \sqrt{\frac{1}{1 + \frac{I_{\text{He}}}{I_{\text{cell}}} \left(1 - \frac{\rho_s(T)}{\rho}\right)}} \right) \\
 &\approx \frac{f_0}{2} \frac{I_{\text{He}}}{I_{\text{cell}}} \frac{\rho_s(T)}{\rho}. \tag{3.5}
 \end{aligned}$$

Changes in  $f$  can be examined over any temperature range and occur for a variety of reasons. The principle is still the same: larger  $\Delta f$  results from larger increases in non-classical rotational inertia.

### 3.1.4 Oscillation Amplitude

The amplitude of oscillation is directly related to the signal amplitude at the detection electrode and can indicate the amount of energy dissipation in the cell. For a driving signal of constant peak-to-peak amplitude, smaller detection signal amplitudes represent larger energy dissipation. An expression for the oscillation amplitude can be derived from the equations of motion.

In a real torsional oscillator, there are mechanisms of energy loss. Assuming a periodic driving force of  $F_0 \cos(\omega t)$ , Eq. 3.1 can be rewritten as

$$I \frac{d^2\theta}{dt^2} + b \frac{d\theta}{dt} + \kappa\theta = F_0 \cos(\omega t), \quad (3.6)$$

where  $b$  contains the loss mechanism(s). For convenience we can rewrite Eq. 3.6 using  $\gamma = b/I$  and  $\omega_0 = \sqrt{\kappa/I}$ , which is the oscillation frequency of an ideal torsional oscillator:

$$\frac{d^2\theta}{dt^2} + \gamma \frac{d\theta}{dt} + \omega_0^2\theta = F_0 \cos(\omega t). \quad (3.7)$$

It is now possible to make the substitution  $z = \theta + iy$ , which yields

$$\frac{d^2z}{dt^2} + \gamma \frac{dz}{dt} + \omega_0^2z = F_0 e^{i\omega t}. \quad (3.8)$$

Assume  $z$  is of the form

$$z = A e^{i(\omega t - \delta)}, \quad (3.9)$$

then Eq. 3.8 gives the relation

$$\begin{aligned} (-\omega^2 A + i\gamma\omega A + \omega_0^2 A) e^{i(\omega t - \delta)} &= \frac{F_0}{I} e^{i\omega t} \\ (\omega_0^2 - \omega^2) A + i\gamma\omega A &= \frac{F_0}{I} e^{i\delta}. \end{aligned} \quad (3.10)$$

$\delta$  can be understood in terms of the vectors in Fig. 3.4. Equating the real and imaginary parts of Eq. 3.10 gives a set of two equations that can be solved for  $A$  and  $\delta$ .

$$A(\omega) = \frac{F_0/I}{[(\omega_0^2 - \omega^2)^2 + (\gamma\omega)^2]^{1/2}} \quad (3.11)$$

$$\tan \delta(\omega) = \frac{\gamma\omega}{\omega_0^2 - \omega^2} \quad (3.12)$$

$A(\omega)$  is the amplitude of the oscillation. A hypothetical sketch for a certain  $I$  and  $\gamma$

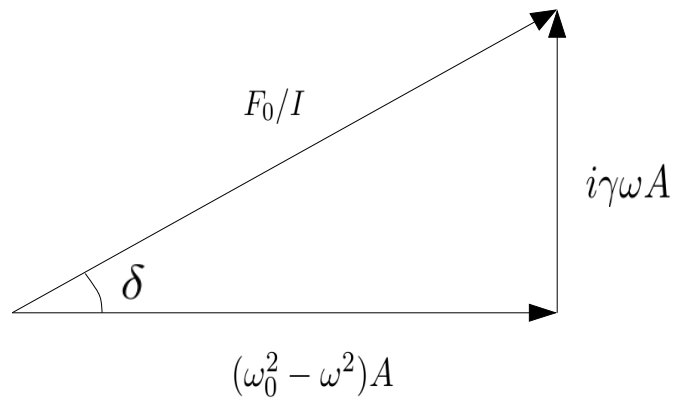


**Fig. 3.4:** Drawing of the vector relationship including delta.

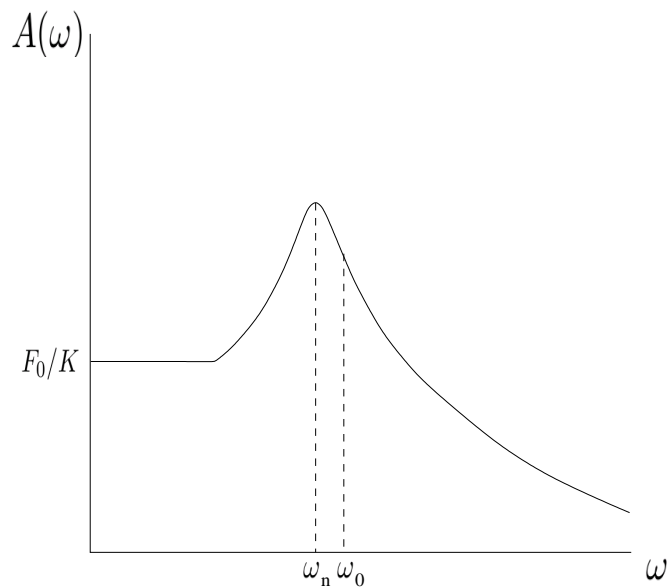


**Fig. 3.5:** Sketch of  $A(\omega)$  for a given  $I$  and  $\gamma$ .

is shown in Fig. 3.5. The form of  $A(\omega)$  changes with  $I$  and  $\gamma$ , as does  $\omega_n$ , the resonant frequency for a given  $I$  and  $\gamma$ .

To understand the effect of  $\gamma$  on the function  $A(\omega)$ , it is useful to introduce the quality factor  $Q$ , defined by

$$Q = \frac{\omega_0}{\gamma}. \quad (3.13)$$

As  $Q$  decreases ( $\gamma$  increases), the distribution of  $A(\omega)$  broadens and the maximum  $A(\omega)$ , which is realized at resonance, decreases. This behavior is pictured in Fig. 3.6.

Data are often plotted as  $Q^{-1}$ . So, maxima in  $Q^{-1}$  correspond to maxima of energy loss.

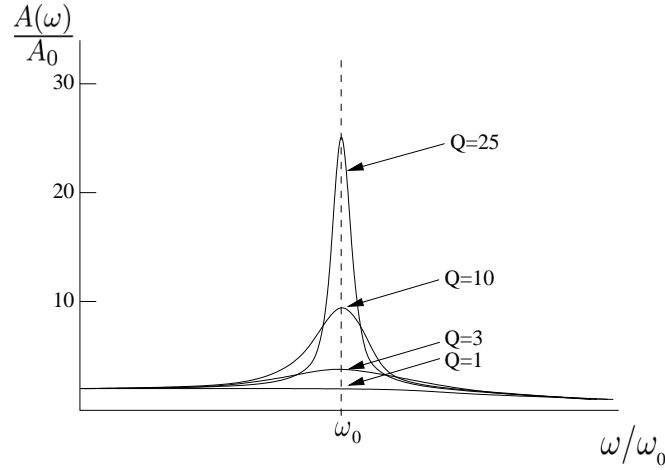


Fig. 3.6: Sketch of various  $A(\omega)$  with different  $Q$  values.

### 3.1.5 Oscillation Velocity

As the oscillator is driven harder (i.e. the amplitude of the driving signal is increased), it moves faster. The maximum velocity of the sample during oscillation will be derived. The complex current can be written as

$$Ie^{i\omega t} = \frac{d}{dt}(CV) = \epsilon_0 S V_B \frac{d}{dt} \frac{1}{D}, \quad (3.14)$$

where  $C$  is the capacitance between the fixed and movable electrodes,  $\epsilon_0$  is the vacuum permittivity (low temperature experiments are almost always performed in vacuum for insulation),  $S$  is the electrode area,  $V_B$  is the bias voltage, and  $D$  is the distance between electrodes. During oscillation,  $D$  is given as a function of time by

$$D = D_0 + \Delta D e^{i\omega t}, \quad (3.15)$$

with  $D_0$  a constant. Combining Eqs. 3.14 and 3.15, and making the approximation  $\Delta D \ll D_0$  (typically  $\Delta D \approx 10\text{-}1000$  nm and  $D_0 \approx 0.1$  mm) yields

$$(\Delta D)\omega = \frac{D_0^2 I}{\epsilon_0 S V_B}. \quad (3.16)$$

The velocity  $(\Delta D)\omega$  corresponds to the movement at the center of the electrode. However, the maximum sample velocity is realized at the outer edge of the sample. Thus, the maximum sample velocity is found by using a geometric ratio:

$$v_{\max} = \frac{r_{\text{sample}}}{r_{\text{electrode}}} (\Delta D)\omega = \frac{r_{\text{sample}}}{r_{\text{electrode}}} \frac{D_0^2 I}{\epsilon_0 S V_B}. \quad (3.17)$$

The constant  $D_0$  can be calculated if the capacitance between the electrodes and  $S$  are known. Practically, the velocity is set by adjusting the size of the drive signal.

### 3.2 Grafoil Experimental Cell

A coin silver torsional oscillator containing a sample of grafoil with surface area  $120 \text{ m}^2$  was mounted on a platform hung below the mixing chamber of the dilution refrigerator. The  $Q$  was 200,000 at 4.2 K and the resonant frequency was 903.6 Hz. Figure 3.7 sketches the cross section of the cell hanging below the mixing chamber.

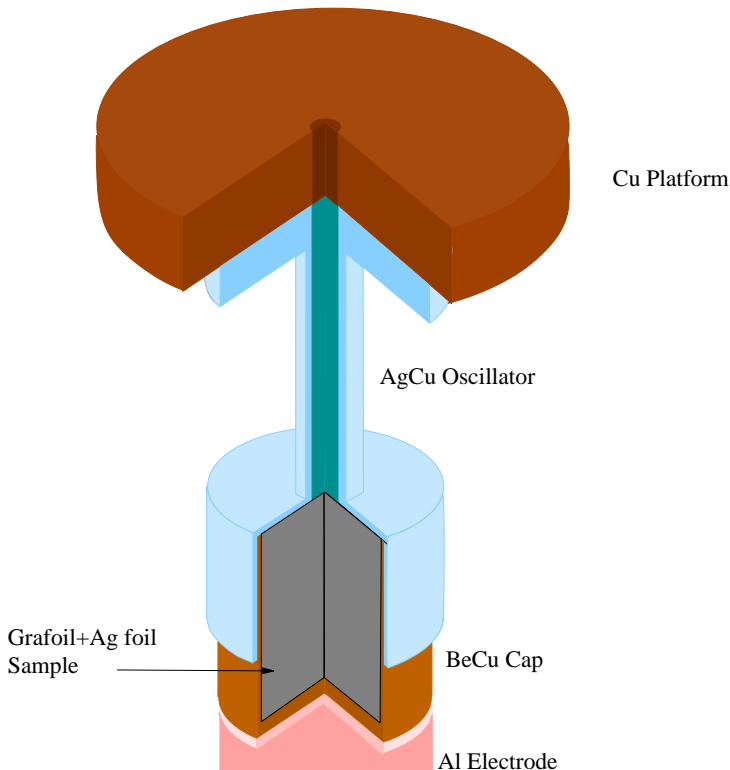
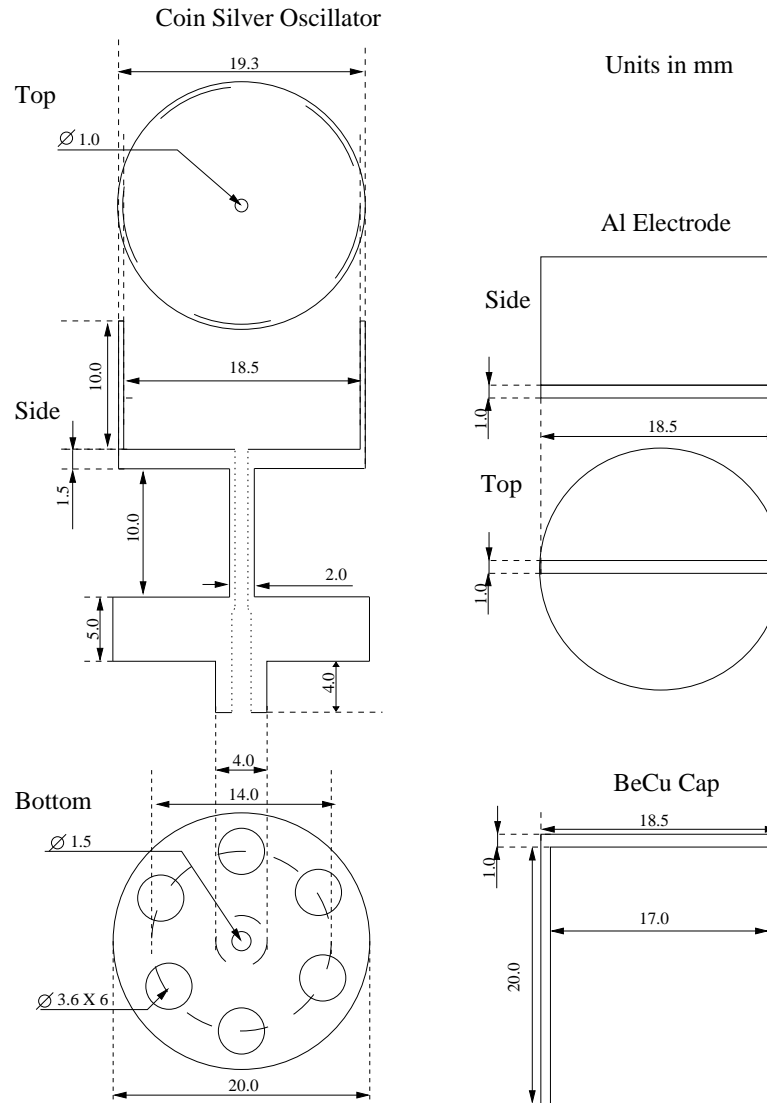


Fig. 3.7: Sketch of the cell, which was hung on the mixing chamber.

#### 3.2.1 Torsional Oscillator Design

To achieve high quality factors and detection of quantum phenomena at low temperature, torsional oscillators should be made of materials whose stiffness depends little on temperature (small stiffness change with temperature) and that have good thermal conductivity. Suitable materials for torsional oscillators include beryllium copper (BeCu), Aluminum 5056 (Al 5056), and coin silver (AgCu). Aluminum was not suitable for this experiment due to its poor heat conduction below 1.2 K, where it becomes superconducting. Of the remaining two choices, AgCu typically shows a frequency shift that is an order of magnitude less than BeCu when cooling from 200 mK to 50 mK.

A design schematic of the torsional oscillator is shown in Fig. 3.8. A 1.0 mm diameter  $^4\text{He}$  fill line was drilled from the bottom of the oscillator through the torsion rod.



**Fig. 3.8:** Schematic of the AgCu oscillator, BeCu cap, and Al movable electrode.

The oscillator and cap were designed to contain pressures high enough to facilitate the growth of solid  $^4\text{He}$ . The top of a cylinder containing pressure  $P$  experiences a maximum stress given by

$$F = \frac{3r^2P}{4t^2} \quad (3.18)$$

where  $r$  is the inner radius of the cylinder and  $t$  is the thickness of the cylinder wall (38). To avoid deformation of the cap,  $F$  must be less than the yield stress of the material, BeCu. A thickness of 0.75 mm was judged to have enough strength to withstand the

	BeCu	AgCu	Al 5056
Density ( $\rho$ )	8.23 g/cm <sup>3</sup>	10.5 g/cm <sup>3</sup>	2.64 g/cm <sup>3</sup>
Young's Modulus ( $E$ )	1.3(10 <sup>11</sup> ) N/m <sup>2</sup>	8.3(10 <sup>10</sup> ) <sup>2</sup> N/m <sup>2</sup>	7.03(10 <sup>10</sup> ) N/m <sup>2</sup>
Shear Modulus $G$	5.3(10 <sup>11</sup> ) N/m <sup>2</sup>	3.0(10 <sup>10</sup> ) N/m <sup>2</sup>	2.61(10 <sup>10</sup> ) N/m <sup>2</sup>
Yield Stress	1.2 GPa	170 MPa	405 MPa

**Table 3.1:** Physical properties of BeCu, AgCu, and Al 5056.

pressures required for <sup>4</sup>He solidification. Table 3.1 lists material characteristics that were used in the design of the oscillator.

After machining of the AgCu oscillator, it was annealed in vacuum at 700°C for 3 hours. The BeCu cap was annealed at 350°C for 3 hours. Annealing serves to remove impurities and increase the material quality.

#### 3.2.2 Grafoil Sample

Grafoil is a commercially available exfoliated graphite and is received as a flexible sheet of a specified thickness. GTA grade grafoil of thickness 0.635 mm was purchased from GrafTech. A stack of grafoil and 0.05 mm thick silver (Ag) foil was assembled and machined to the appropriate size to fit the sample space. The Ag foil provided thermal conductivity and kept the individual grafoil sheets from slipping during oscillation. Special care and annealing were required in order to achieve bonding of the grafoil and Ag foil. The following steps were used in assembly of the grafoil-Ag foil stack.

1. grafoil and Ag foil were cut into squares of about 20 x 20 mm.
2. The grafoil was annealed at 1200°C for 12 hours in vacuum.
3. The Ag foil was ultrasonically cleaned in 15 % HNO<sub>3</sub> for 15 minutes.
4. The Ag foil was annealed at 700°C for 3 hours in vacuum.
5. A stainless steel holder (described below) was annealed at 750°C for 3 hours in vacuum.
6. A stack of 40~50 grafoil squares and Ag squares was assembled in an alternating pattern, pressed, and held together with the stainless steel holder.
7. The stack was annealed in the stainless steel holder at 715°C for 3 hours in vacuum.

During the final annealing, pressure on the order of 0.1 GPa was applied to the stack with a simple stainless steel holder. The holder was made from two blocks of stainless steel held together by four screws. Because the grafoil also binds to the stainless steel surface, a sheet of 'dummy' grafoil was inserted between the stack and the holder to ensure that the stack did not bind to the holder. A sketch is shown in Fig. 3.9. The

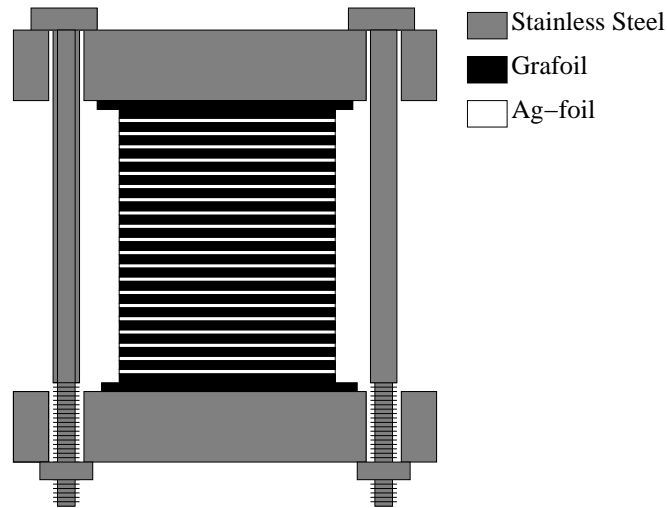


**Fig. 3.9:** Sketch of the grafoil stack held by the stainless steel holder. Not drawn to scale.

stack was then machined to the appropriate size with the lathe. The surface area of the machined graphite sample was determined to be 120 m<sup>2</sup> by the BET Method (39) with nitrogen adsorption. See the appendix Sect. A.1 for the nitrogen adsorption isotherms and BET fit.

### 3.2.3 Assembly And Fitting

To avoid leaks, maximize the signal response of the oscillator, and ensure good thermal coupling of the graphite sample to the oscillator, all parts should fit together well. To achieve this, the following procedure was used to assemble and fit the parts.

To ensure good fitting of the grafoil sample in the torsional oscillator, the stack was machined in a lathe to fit snugly into the annealed cap (and thus once pressed in, it cannot be removed). Although bound together by the process stated in Sect. 3.2.2, the stack is still fragile and may break during machining. To avoid this, pressure was applied in the vertical direction (the same direction as it had been applied during annealing) via a brass holder shown in Fig. 3.10. Use of the brass holder required that a hole first be carefully drilled through the unmachined stack in the approximate center. This hole was drilled by using a jig similar to the one shown in Fig. 3.9 but

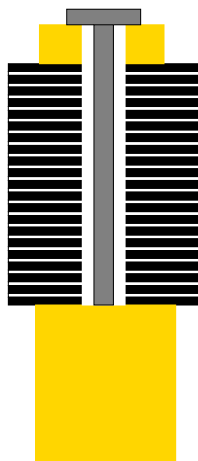


**Fig. 3.10:** Sketch of brass holder used to machine the stack with the lathe. Not drawn to scale.

made of Al and both metal plates had a hole in the center. All tools and machines were carefully cleaned before use to prevent contamination of the grafoil. A photograph of the machined stack is shown in Fig. 3.11, where small holes can be seen in the stack. These holes, which allow helium easy access into the graphite sample, were made with a sewing needle.

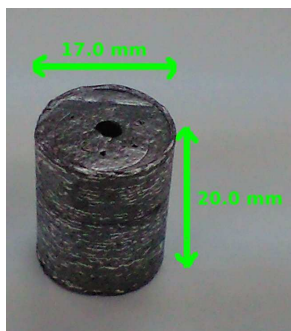


**Fig. 3.11:** The machined grafoil-Ag foil sample.

The stack was then glued into the BeCu cap using stycast 1266. The stycast was applied sparingly to the inside of the cap and the sides of the graphite sample. The sample glued into the cap is pictured in Fig. 3.12.

Stycast 2850 was then used to glue the BeCu cap into the AgCu oscillator. The Al electrode (the experiment's movable electrode) was glued to the top of the assembled oscillator with stycast 2850 and a thin sheet of insulating paper.



**Fig. 3.12:** The sample after being glued into the cap.

## 3.3 Other Experimental Apparatus at Low Temperature

### 3.3.1 Cu Platform

The oscillator was mounted with screws and an indium seal to a copper platform, which was hung below the mixing chamber of the dilution refrigerator. As the schematic shows in Fig. 3.13, a 2.0 mm hole leading out the side of the platform allowed the cell to be filled with  $^4\text{He}$ . The fill line connected to a valve at the top of the dilution unit and  $^4\text{He}$  was supplied by a tank connected to a gas handling system at room temperature.

### 3. EXPERIMENTAL METHOD AND APPARATUS

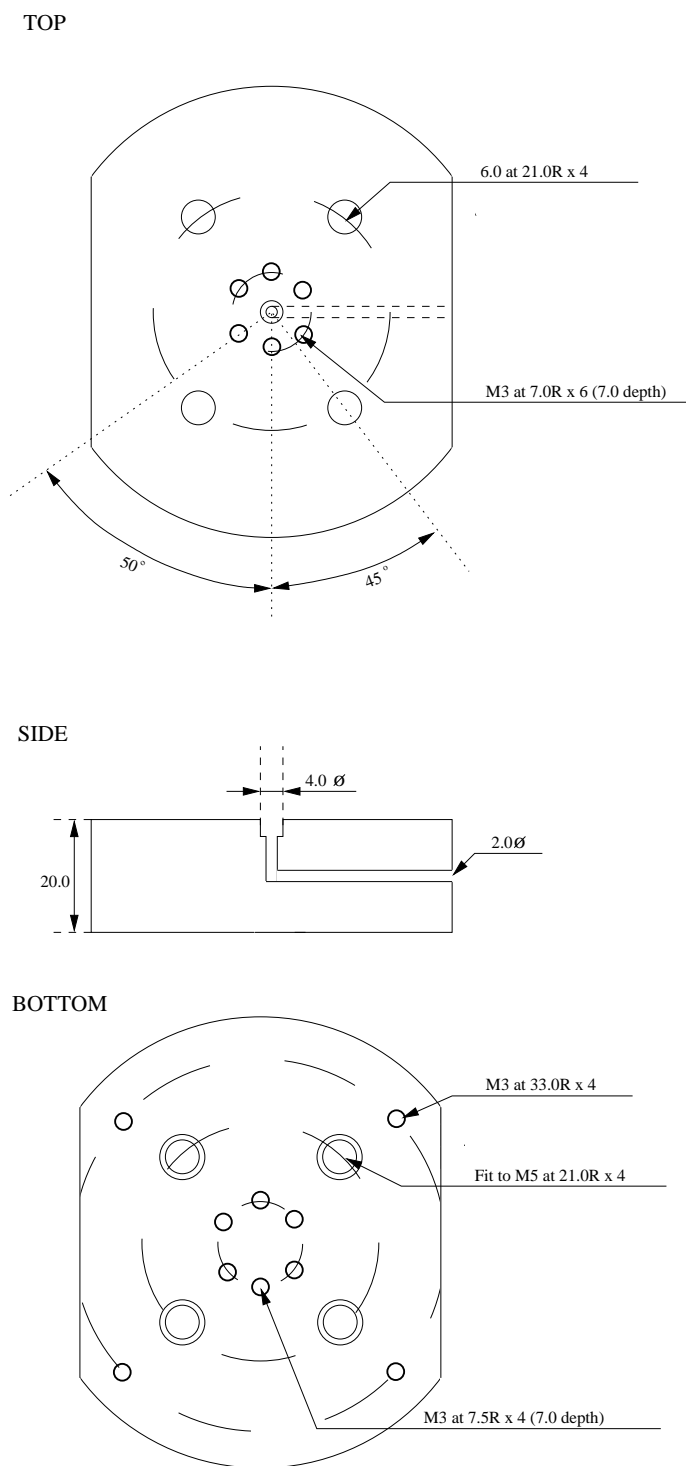


**Fig. 3.13:** Schematic of the copper platform.

## 3.3.2 Electrodes

The movable electrode, whose schematic is shown in Fig. 3.8, was constructed from Al 5056 and designed to sit on the torsional oscillator cap. It was glued in place with stycast 2850 and electrically insulated using a thin piece of paper. The electrode was biased to over 300 V with a battery via a thin gold wire connected to the center of the electrode with silver paste.

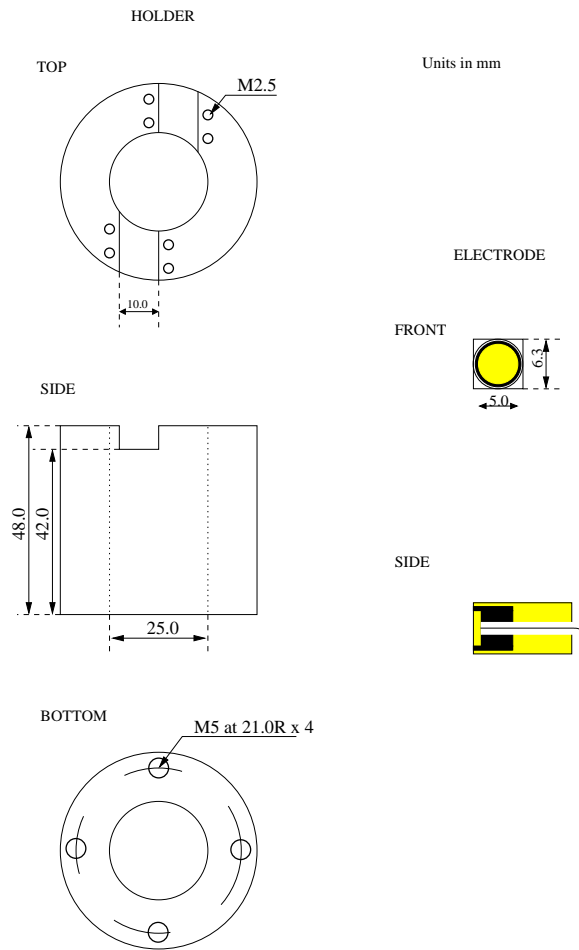


**Fig. 3.14:** Schematic of the fixed electrodes and their holder.

Fixed electrodes for the detection and drive signals were made from brass. The schematic in Fig. 3.14 shows that the active area of the electrodes was  $19.6 \text{ mm}^2$ . A simple circular brass holder, designed to surround the oscillator, elevated and held the fixed electrodes in place. They were placed as close as possible to the movable electrode without touching it.

Figure 3.15 shows a photograph of the assembled cell surrounded by the brass holder and fixed electrodes.

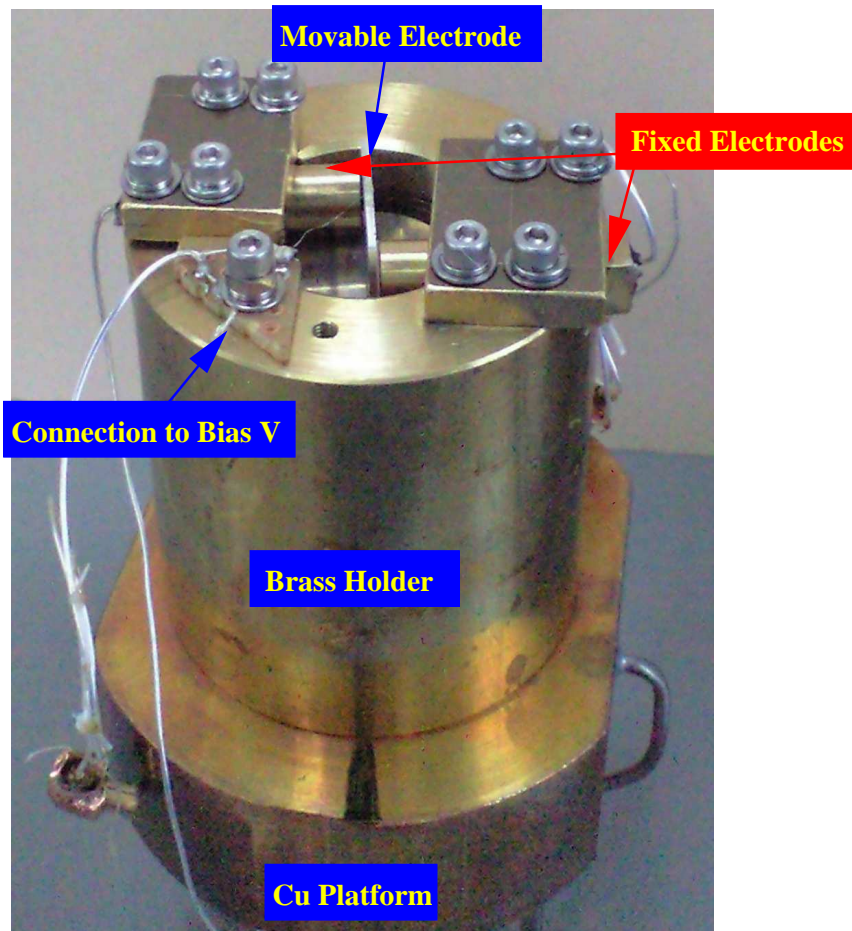


**Fig. 3.15:** Photograph of the assembled cell surrounded by the brass holder and fixed electrodes.

#### 3.3.3 Heat Switch

The copper platform was connected to the mixing chamber with a heat switch. A sketch is shown in Fig. 3.16. The heat switch was made from two copper disks connected to a stainless steel tube, which can be filled with  $^4\text{He}$  independently of the cell. When filled with  $^4\text{He}$ , the heat switch conducts heat from the cell to the mixing chamber, allowing for the maximum cooling power of the dilution refrigerator to reach the cell. When empty, the heat switch partially insulates (there is still heat conducted through the  $^4\text{He}$  fill line to the cell) the cell from the dilution refrigerator. The ability to turn heat conduction on and partially off is beneficial because dilution refrigerators usually become unstable above 1 K when the circulating mixture gas starts to boil. Turning heat conduction partially off allows the cell to be heated beyond 1 K while keeping the dilution refrigerator stable.

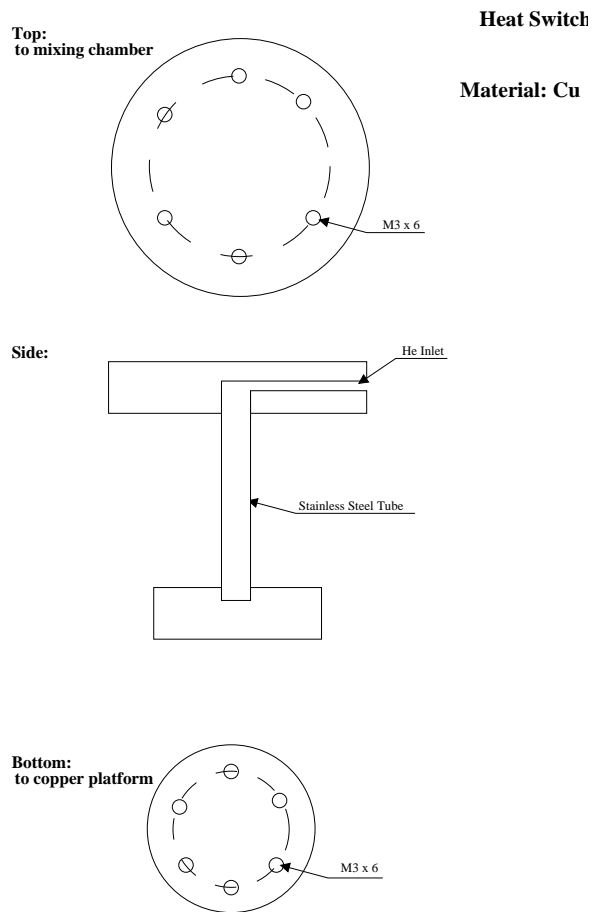


**Fig. 3.16:** Sketch of the heat switch used to connect the copper platform to the mixing chamber.

#### 3.3.4 Thermometer and Heater

A ruthenium oxide thermometer, which was previously calibrated in this lab, and a cernox thermometer were used to measure the cell's temperature. As seen in Fig. 3.17, it was mounted to the platform via a simple copper block. A 120  $\Omega$  strain gauge, used as a heater, was also placed on the platform and was held in place with varnish.

#### 3.3.5 Pressure Gauge and Regulator

Pressure was measured with a capacitive pressure gauge. Pressure was regulated by heating a small volume containing activated carbon that was weakly linked to 4.2 K and mounted on (but insulated from) the 1 K pot stage of the dilution refrigerator. The same capacitive pressure gauge and pressure regulator were used in both experiments.

The schematic of the pressure gauge, drawn in Fig. 3.18, shows a design in which a cavity with a thin diaphragm was made from BeCu. The cavity was connected to the

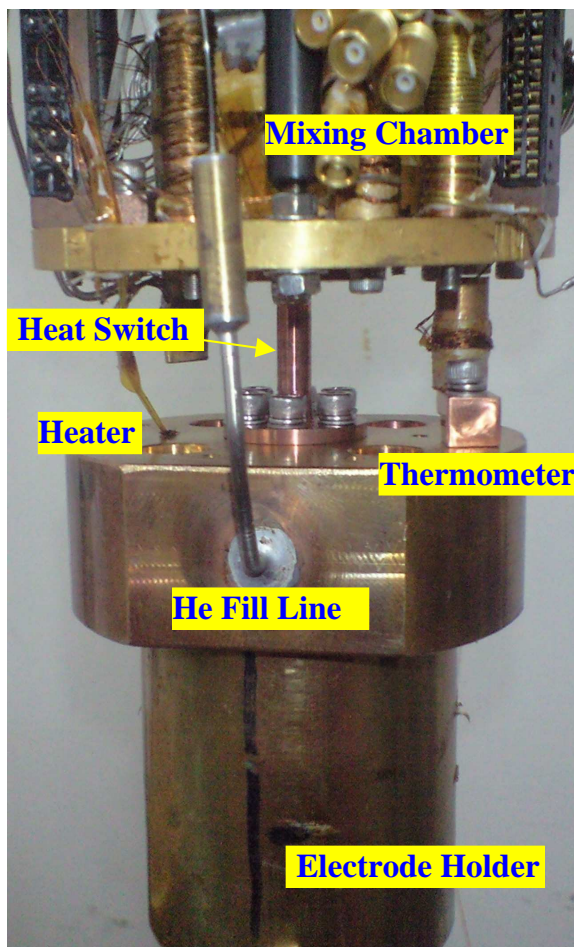


**Fig. 3.17:** Picture of the thermometer and heater mounted to the copper platform, mounted below the mixing chamber by the heat switch

same helium line as the cell, so the liquid pressure in the cavity and cell were assumed equal. As the pressure in the cavity increases, the diaphragm bows outward and the capacitance between the two Cu electrodes increases. The pressure gauge could make measurements with errors on the order of a few Pa. The capacitive pressure gauge was calibrated at above 1.6 K before each experiment against a room temperature digital pressure gauge.

Figure 3.19 shows a sketch of the experimental setup with the pressure gauge mounted on the Cu platform. By controlling the heating of the pressure regulator with a computer, the pressure was stabilized to better than 100 Pa.

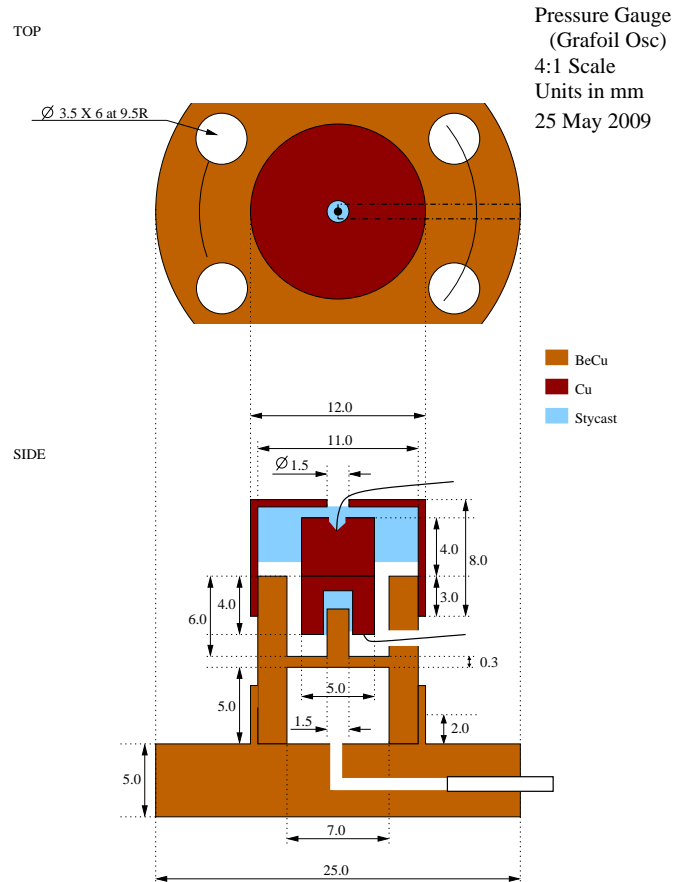


**Fig. 3.18:** Schematic of the capacitive pressure gauge. Not drawn to scale.

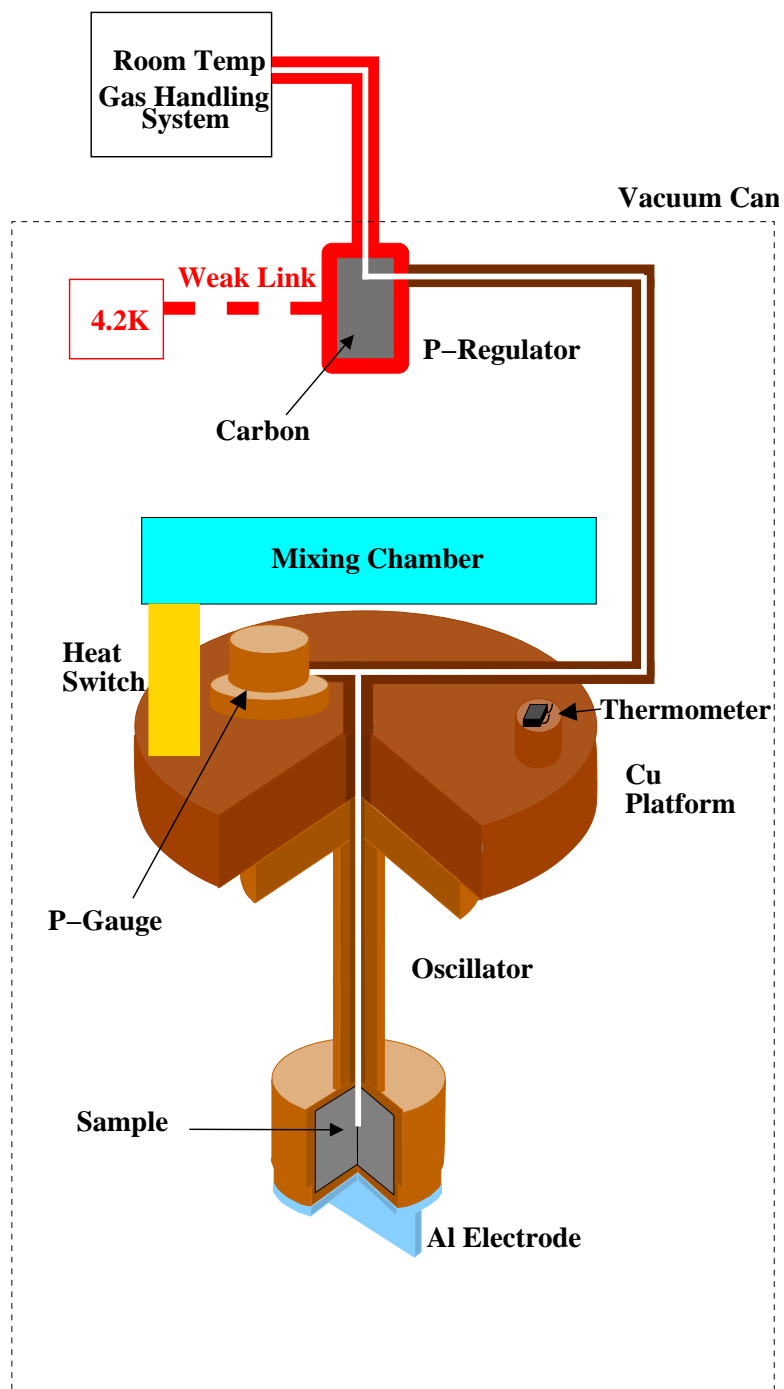


**Fig. 3.19:** Sketch of the cell and system for pressure regulation. The same system was used to regulate the pressure in both experiments.

### 3.4 Graphene Experimental Cell

The cell for measurements on graphene was made from BeCu and the schematic is shown in Fig. 3.20. The cell contained multilayer graphene with a total surface area of 28 m<sup>2</sup>. The  $Q$  was about 300,000 and the resonant frequency was 1189.9 Hz at 4.2 K. The copper platform, thermometers, heater, pressure gauge and regulator, heat switch, fixed electrodes, and brass holder from the grafoil measurement were reused. The torsional oscillator and movable (biased) electrode were changed.

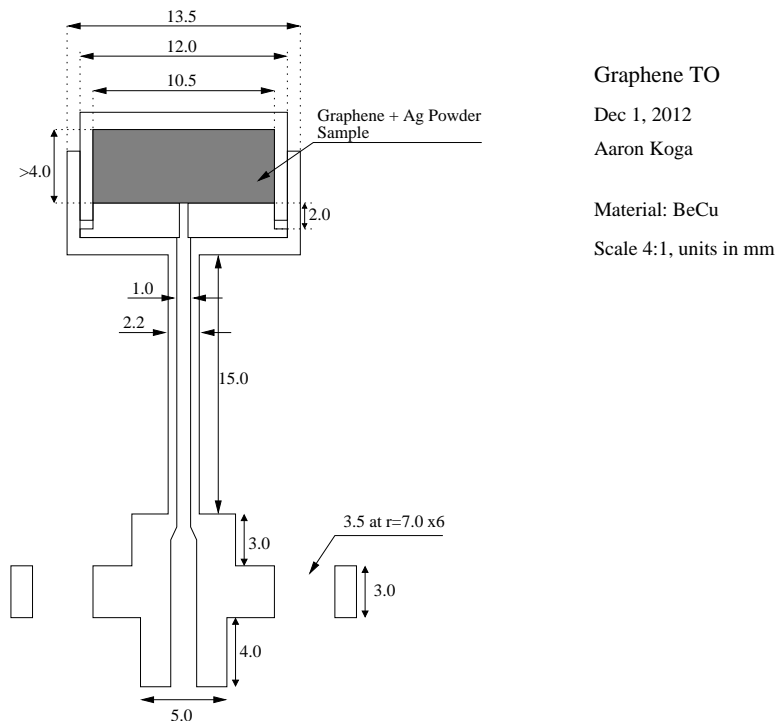


**Fig. 3.20:** Schematic of the torsional oscillator used in graphene measurements. Not drawn to scale.

#### 3.4.1 Graphene Sample

The sample was commercially available multilayer graphene, sold by XG-Sciences (xGnP type M (40)). According to the manufacturer, the individual graphene platelets have an average diameter of 5-7  $\mu\text{m}$  and are aggregated into particles with 6 nm average thickness. This means that with about 3.35  $\text{\AA}$  spacing between sheets, the particles consist of 10-20 graphene layers. It is important to note that the stacking order of the sheets is not necessarily that of graphite (ABAB for hcp or ABC for rhombohedral). It is not unreasonable to also think that the individual graphene sheets can be rotated

### 3. EXPERIMENTAL METHOD AND APPARATUS

with respect to one another. Furthermore, the spacing between sheets, although approximately  $3.35 \text{ \AA}$ , may contain larger voids and irregularities. This can occur at, for example, the area where the edges of two sheets overlap. Therefore, the adsorption potential is probably stronger than a single graphene sheet due to the presence of multiple layers. But because of the irregular stacking of individual sheets, it is weaker than graphite. SEM images of the graphene sample as received from the manufacturer are shown in Fig. 3.21. Per the manufacturer's claim, the individual platelet sizes do indeed look to be on the  $\mu\text{m}$  order.

In order to fix the graphene in the torsional oscillator, it was mixed with 200 mesh Ag powder. The ratio of graphene to Ag powder was approximately 1:4 by mass. The mixture was sintered into the BeCu oscillator cap by pressing under a force of 0.1 GPa while heating at  $200 \text{ }^\circ\text{C}$  in vacuum for a few hours. A jig similar to that used to prepare the grafoil-Ag foil stack, but appropriate for a powdered sample was employed. The resulting pellet was determined to have a surface area of  $28 \text{ m}^2$  via nitrogen adsorption. See the appendix Sect. A.1 for the nitrogen adsorption isotherms and BET fit. Figure 3.22(A) shows the graphene and Ag-powder mixture after being heated and pressed into the oscillator cap and Fig. 3.22(B) shows the assembled oscillator.

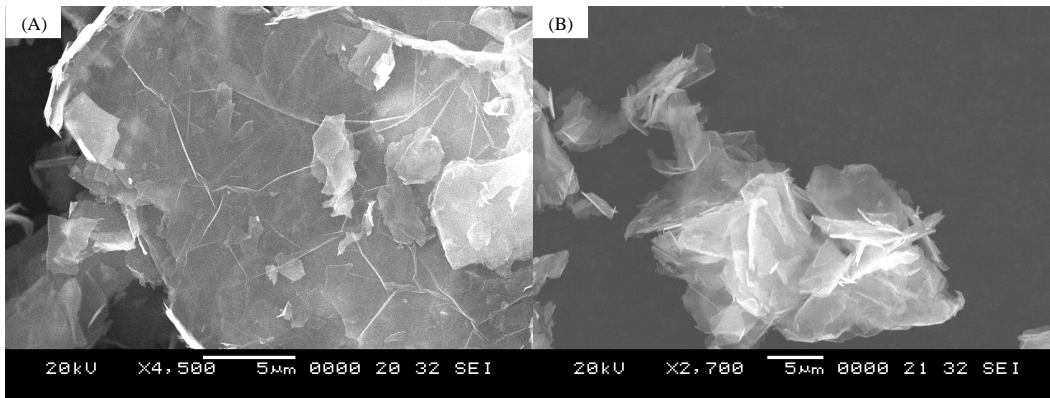
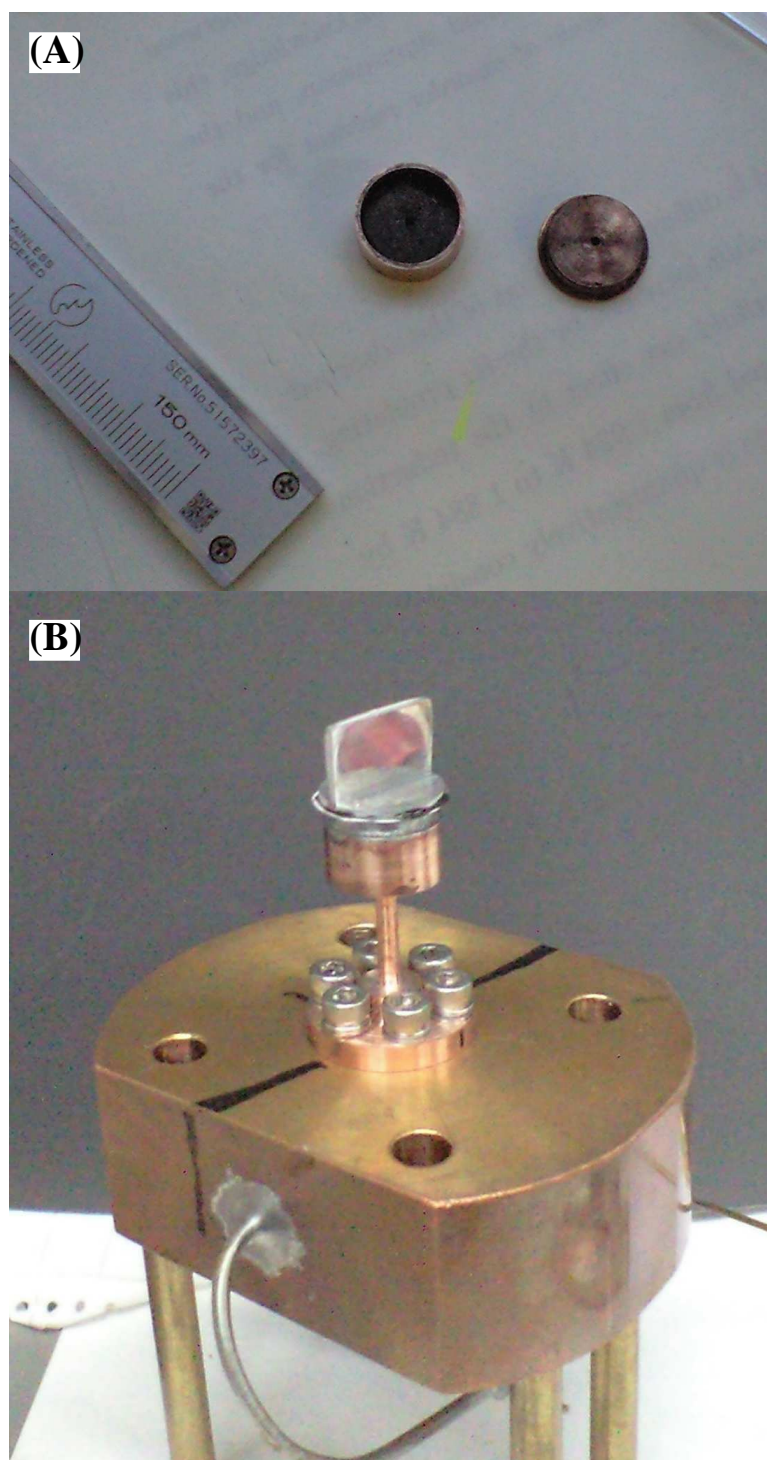


Fig. 3.21: SEM images of the bare graphene sample.



**Fig. 3.22:** (A): Image of the pressed graphene sample in the oscillator cap. (B): Assembled oscillator on the Cu platform.

### 3.5 Room Temperature Electronics for Temperature, Pressure, Frequency, and Amplitude Measurement

The room temperature electronics were controlled via computer through gpib interfaces.

#### 3.5.1 Temperature Measurement and Regulation

The temperature of the oscillator was controlled by a Picowatt TS-530A temperature controller and an AVS-47B resistance bridge. The ruthenium oxide (below 1.1 K) and cernox (above 1.1 K) thermometers on the platform was used to measure the temperature of the cell while heat was applied via the strain gauge. Although the TS-530A and AVS-47B were computer controlled during data acquisition, the optimal PID parameters for temperature control were determined manually before the experiment and stored on the computer in a look-up table.

#### 3.5.2 Pressure Measurement and Regulation

Pressure was measured with an Andeen Hagerling 2550A capacitance bridge. The pressure regulator mounted on the 1 K pot stage was heated using a computer controlled current source. The computer controlled PI regulation achieved better than 100 Pa pressure stabilization.

#### 3.5.3 Frequency and Amplitude Measurement

The oscillator was kept on resonance with the use of the feedback loop shown in Fig. 3.23. All components are commercially available except for the zero crossing detector (ZCD). This is a homemade item that turns any input into a square wave output. Frequency and amplitude data were from the Pendulum CNT-90 frequency counter (clocked with a Pendulum 6680 reference clock) and Stanford Research Systems SR-830 lock-in amplifier respectively.

Measurements on grafoil were taken with the oscillator in constant drive mode (41). The signal applied at the drive electrode is of constant amplitude and the oscillation amplitude decreases with energy dissipation. The driving amplitude was set at the beginning of the experiment to provide an oscillation velocity of 100  $\mu\text{m/s}$ . Measurements on graphene were taken with the oscillator in constant amplitude mode. The amplitude measured at the detection electrode is kept constant by changing the amplitude of the driving signal. The amplitude was varied to provide a velocity of about 100  $\mu\text{m/s}$ . This modification helped to keep the oscillator on resonance amid sudden changes in  $Q$  during the graphene experiment.

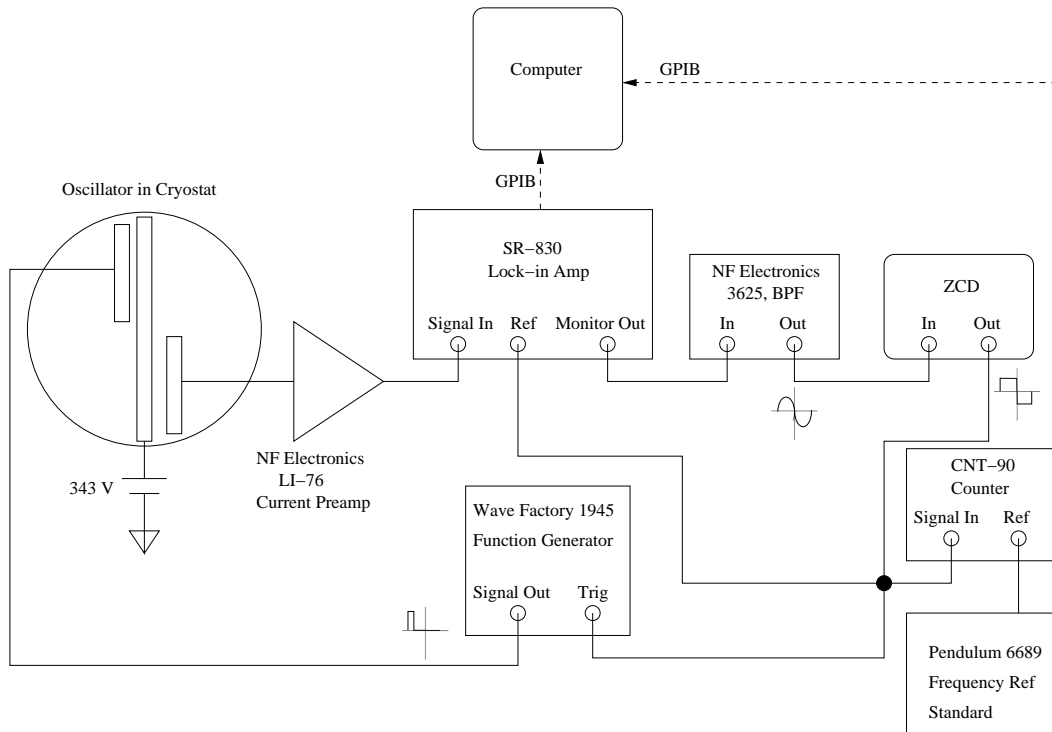


Fig. 3.23: Block diagram of the feedback loop used to measure the oscillator frequency.

## 3.6 Procedure for Data Acquisition

Data were taken by measuring the resonant frequency  $f$  and amplitude (converted to  $Q^{-1}$ ) at constant temperature while changing the pressure in small steps. The cell was allowed to come to equilibrium at each pressure by pausing for 15 to 40 min. After each pause, data for  $f$  and  $Q^{-1}$  were then taken and the pressure was changed for the next data point. Both cells were initially filled from the empty state with liquid at 4.2 K. Care to avoid large vibrations and other disturbances to the cell between isotherms was taken.

### 3.6.1 Grafoil

Freezing data were taken by first increasing the pressure in 0.02 to 0.1 MPa steps by hand up to about 2.1 MPa. The pressure regulator was then heated to increase the pressure to near bulk freezing.

Melting data were taken by preparing samples using the pressure-temperature paths sketched in Fig. 3.24. The samples were pressurized at 500 mK by introducing  $^4\text{He}$  into the cell to about 2.1 MPa and then using the pressure regulator to bring the cell to just under  $P_s$ . The pressurization process took less than 1 hour. Care was taken to prepare

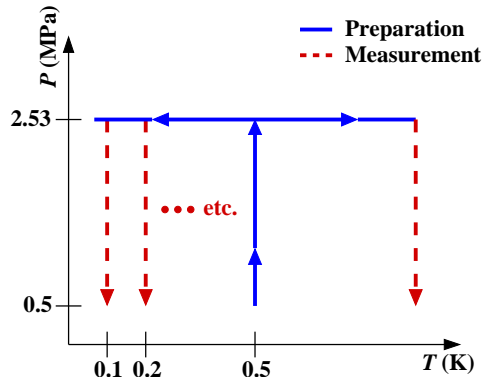


**Fig. 3.24:** Sketch of the pressure-temperature paths for sample preparation and measurement of melting data in the grafoil experiment.

each sample at 500 mK to ensure consistency between samples. The cell was then cooled/heated at constant pressure to the desired measurement temperature. After coming to equilibrium, the pressure was decreased by first using the pressure regulator down to 2.1 MPa and then decreasing the pressure by hand down to around 0.5 MPa.

### 3.6.2 Graphene

Freezing data were taken by first increasing the pressure in 0.02 to 0.1 MPa steps by hand up to about 1.55 MPa. The pressure regulator was then heated to increase the pressure to near bulk freezing.

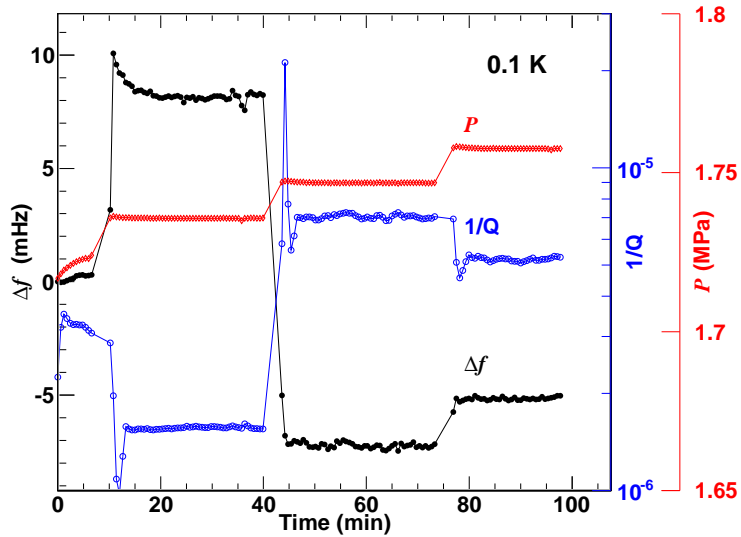
# 4

## Data and Analysis

This chapter presents the results of this thesis and the method used to analyze them.

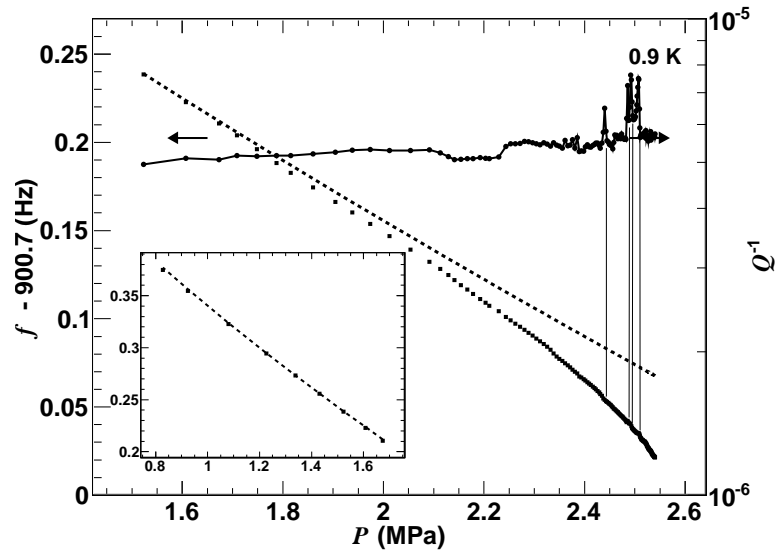
### 4.1 Raw Data

Figure 4.1 shows sample raw data for the oscillation frequency  $f$ , energy dissipation  $Q^{-1}$ , and pressure  $P$  from the graphene cell as a function of time. This data is representative of all isotherms taken from both experiments. To take data,  $P$  is increased or decreased in a step-like fashion. The cell is paused at each pressure and the data clearly shows that the cell comes to equilibrium.



**Fig. 4.1:** Sample raw data from the graphene cell for frequency change from time=0  $\Delta f$ ,  $Q^{-1}$ , and  $P$ . The cell comes to equilibrium at each pressure.

## 4.1.1 Raw Grafoil Data



**Fig. 4.2:** Raw melting data from the grafoil experiment as a function of  $P$  for  $f$  and  $Q^{-1}$  taken at 0.9 K above 1.6 MPa. Vertical solid lines mark the frequency shifts coinciding with dissipation. The inset shows  $f$  from the same isotherm below 1.6 MPa. The liquid background  $f_L$  is plotted as the dotted line (see Sect. 4.2.1).

Sample data from the grafoil experiment of solid  $^4\text{He}$  melting at 0.9 K are shown in Fig. 4.2. The data show a mostly smooth change in  $f$  as a function of pressure. Small shifts in  $f$ , sometimes coinciding with energy dissipation, or maxima in  $Q^{-1}$ , are seen. Data from the same isotherm below 1.6 MPa are shown in the inset of Fig. 4.2.

## 4.1.2 Raw Graphene Data

Graphene data from the 1.05 K growth isotherm are shown in Fig. 4.3. As the pressure is increased, the frequency  $f$ , shows a mostly smooth decrease punctuated with frequency shifts coinciding with energy dissipation, or peaks in  $Q^{-1}$ . The graphene measurements show very regular behavior across all isotherms. Each isotherm contains five frequency shifts between 1.0 and 2.3 MPa and each frequency shift coincides with energy dissipation.

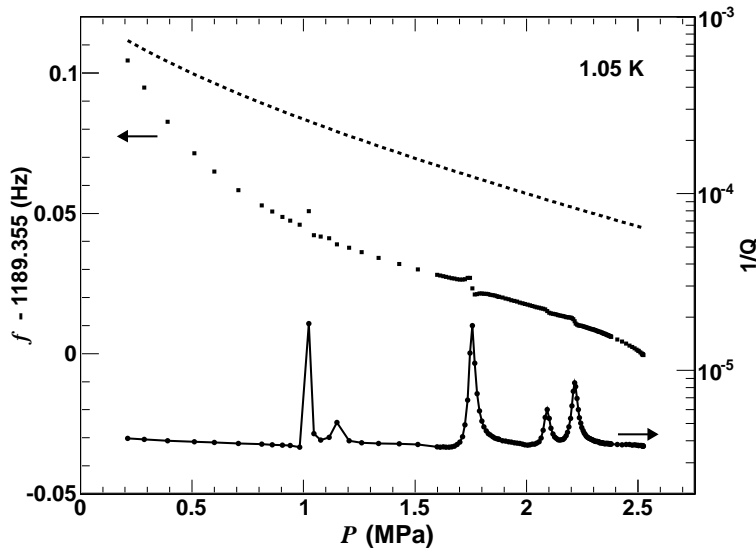


**Fig. 4.3:** Raw data as a function of  $P$  showing  $f$  and  $Q^{-1}$  taken at 1.05 K. The dotted line shows the frequency of the liquid background  $f_L$  (see Sect. 4.2.1).

## 4.2 Analysis

### 4.2.1 Liquid Background

To analyze the  $^4\text{He}$  isotherms, we first note that when changing the pressure of the liquid  $P$  at constant temperature,  $f$  can change as a result of both changes in the density of the liquid  $\rho(P)$  as well as the growth/melting of adsorbed solid  $^4\text{He}$ . Although liquid in the superfluid state theoretically decouples from the torsional motion, some parts may become trapped in the tortuosity of the substrate or couple to at the walls of the oscillator. Therefore,

$$f(P) = \frac{1}{2\pi} \sqrt{\frac{\kappa}{I_{\text{cell}} + I_L(P) + I_s(P)}}, \quad (4.1)$$

where  $I_{\text{cell}}$ ,  $I_L(P)$ , and  $I_s(P)$  are the rotational inertia of the empty cell, the liquid  $^4\text{He}$ , and the solid  $^4\text{He}$ , respectively. The spring constant of the torsion rod is given by  $\kappa$ . Because only the solid growth or melting is of interest, we subtract the frequency background due to the liquid  $f_L$ , to find the frequency change due to only solid  $^4\text{He}$   $f^* = f - f_L$ .

Using the known  $\rho(P)$ , given by Boghosian and Meyer (42),  $f_L$  can be expressed as

$$\begin{aligned} f_L(P) &= \frac{1}{2\pi} \sqrt{\frac{\kappa}{I_{\text{cell}} + I_L(0) \left(\frac{\rho(P)}{\rho(0)}\right)}} \\ &= f_0 \sqrt{\frac{1}{1 + \frac{I_L(0)}{I_{\text{cell}}} \left(\frac{\rho(P)}{\rho(0)}\right)}} \end{aligned} \quad (4.2)$$

where  $I_L(P = 0)$  is the rotational inertia of liquid  $^4\text{He}$  in the cell at low pressure just after it is completely filled and  $f_0$  is the empty cell resonant frequency. The term  $\rho(P)/\rho(0)$  accounts for the increase in liquid density with  $P$ , decreasing  $f$  as  $P$  increases. Since the temperature dependence of  $\rho(P)$  is less than 0.1% with respect to temperature below 1.3 K, we assume the  $\rho(P)$  given by Boghosian and Meyer at  $T = 0$ .

The value of  $I_L(0)/I_{\text{cell}}$  was found by measuring the temperature dependence of  $f$  at a constant, low pressure. The grafoil cell was measured at 0.5 MPa, taking the increased liquid density at 0.5 MPa into account, and the graphene cell was measured at 0.01 MPa.  $f_0$  was measured directly at the beginning of each experiment before  $^4\text{He}$  was admitted to the cell. As the temperature increases, especially above 1 K, some of the superfluid becomes normal fluid and there is increased liquid coupling to the oscillation. Thus, an increase in the value  $I_L(0)/I_{\text{cell}}$  is observed. Data for  $f_0$  and  $f$  in the low pressure state are shown for both cells in Sect. A.2. It may seem that measuring the grafoil cell at 0.5 MPa rather than at lower pressure is inappropriate because solid might grow between 0 and 0.5 MPa. However, experiments for solid growth on grafoil using the fourth sound method (4) saw no evidence of solid growth below about 1.5 MPa and measurements using differential adsorption (3) claimed only a fraction of a layer in total grows below 0.5 MPa. Thus, we believe that in the case of grafoil, 0.5 MPa is a valid pressure to use in the calculation  $I_L(0)/I_{\text{cell}}$ .

The values for  $I_L(0)/I_{\text{cell}}$  in the grafoil cell were found to be  $5.75 \times 10^{-3}$  to  $6.21 \times 10^{-3}$ . The projected value for  $f_L$  for the example isotherm at 0.9 K is plotted as the dotted line in Fig. 4.2. A value of  $7.1 \times 10^{-3}$  is calculated for 50% grafoil porosity and 100% of the liquid helium coupling to the torsional motion. Below  $T_\lambda$ , one would expect some decoupling of the liquid helium and thus a decrease in the value of  $I_L(0)/I_{\text{cell}}$  from the theoretical value for 100% helium coupling. Note that in a previous paper (43), we fitted the data from 1.0 MPa to 1.6 MPa to find the value of  $I_L(0)/I_{\text{cell}}$ . It turns out that the values for  $I_L(0)/I_{\text{cell}}$  given from the fitting,  $5.73 \times 10^{-3}$  to  $6.31 \times 10^{-3}$ , produce results which are indistinguishable from those presented here.

In the graphene cell, values for  $I_L(0)/I_{\text{cell}}$  were found to be  $5.77 \times 10^{-4}$  to  $6.09 \times 10^{-4}$  in the temperature range studied. The dotted line in Fig. 4.3 is the projected value

of  $f_L$  in the graphene cell's 1.05 K isotherm. Full coupling of the superfluid to the torsional motion is calculated to have an  $I_L(0)/I_{\text{cell}}$  value of  $9.0 \times 10^{-4}$ .

$f^*$  can be visualized as the difference between the dotted line ( $f_L$ ) and the data points for  $f$  in Figs. 4.2 and 4.3.

### 4.2.2 Growth and Melting of Adsorbed Solid

The change in frequency of the torsional oscillator is related to the change in rotational inertia by  $\Delta f = \Delta I f_0 / (2I_{\text{cell}})$ , where  $I_{\text{cell}}$  is the empty cell rotational inertia. Assuming constant volume of the cell, the growth (melting) of one solid  $^4\text{He}$  layer decreases (increases) the amount of superfluid. Therefore, the theoretical change in frequency due to the growth of one solid layer is expressed as

$$\Delta f_{\text{LR}}(P) = \frac{f_0}{2I_{\text{cell}}} I_{\text{LR}} \left( 1 - \frac{\rho(P)}{\rho_s} \right), \quad (4.3)$$

with  $\rho_s$  the density of bulk solid. The rotational inertia of one solid  $^4\text{He}$  layer  $I_{\text{LR}}$ , is calculated using the known density of bulk solid (19), the geometry of the cell, and the surface area of the substrate. Although the density of solid in the first two layers adsorbed on graphite is known to be larger than bulk solid, we believe that using the density of bulk solid in our analysis is valid. Recall that while the density of solid in the first layer is significantly higher than the bulk value of  $0.087 \text{ \AA}^{-2}$  (calculated from the bulk solid density), the second layer has a density of  $0.092 \text{ \AA}^{-2}$ , which is only 7% different from bulk. The third and higher layers are expected to be even closer to the bulk solid value. Looking at Eq. 4.3, when  $P \rightarrow 0$ , the difference between  $\rho(P)$  and  $\rho_s$  is the greatest and so is  $\Delta f_{\text{LR}}$ . In the opposite limit,  $\rho(P) \rightarrow \rho_s$  (i.e. all liquid in the cell freezes to bulk solid),  $\Delta f_{\text{LR}} = 0$  since a layer grown on the substrate surface is indistinguishable from a layer grown in the bulk solid.

Dividing by  $\Delta f_{\text{LR}}$ , we convert a change in the solid frequency  $\Delta f^*$  to a change in solid  $^4\text{He}$  coverage  $\Delta n$ , in layers. We sum  $\Delta n$  to find the total number of solid layers on the substrate  $n = \sum \Delta n$ . Note that we cannot determine the absolute number of adsorbed solid layers, but rather the net change during the course of a measurement. We assign the lowest pressure point to a value of  $n = 0$ .

It is thought that  $^4\text{He}$  can tunnel into or out of graphite samples. Although this effect is not well understood, it can heavily affect experiments such as those performed for this thesis. We have estimated the size of the tunnelling effect for both the grafoil and graphene samples and determined that they are negligible. See the appendix, Sect. A.5 for more information.

## 4.3 Grafoil Experiment: Growth and Melting Isotherms

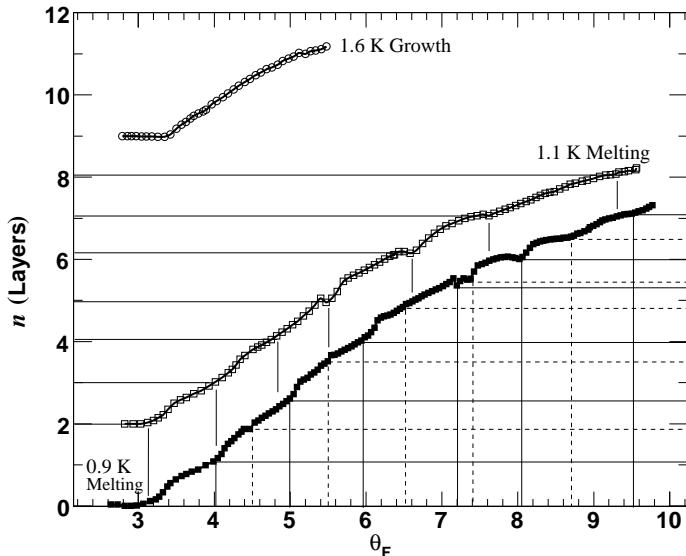


**Fig. 4.4:** Selected growth and melting isotherms from the grafoil experiment. From top to bottom: Growth at 1.6 K, melting at 1.1 K, and melting at 0.9 K. The 1.6 K and 1.1 K curves are shifted vertically for easy viewing. The horizontal axis is scaled with the Franchetti relation. Solid lines mark the onset of original layering transitions and dotted lines mark the onset of secondary transitions.

We obtain isotherms such as those shown in Figs. 4.4 and 4.5. The coverage is plotted as a function of the Franchetti number  $\theta_F$ . Although the continuous growth assumption of the Franchetti Relation (Eq. 2.12) is not an accurate representation of the growth observed in this experiment, the relation facilitates comparison with past experiments. The isotherms show mostly continuous changes in  $n$  with kinks and bumps. The structure of the 0.9 K isotherm appears more complicated than the 1.1 K isotherm, and the 1.6 K isotherm shows a smooth increase in  $n$ . It was not possible to measure above a pressure corresponding to the Franchetti number 5.5 at 1.6 K without freezing of the  $^4\text{He}$  along the helium line (for introducing  $^4\text{He}$  into the cell) near the 1 K pot.

Figures 4.6 and 4.7 plot  $n$  for all the melting and growth isotherms respectively. The isotherms are also individually plotted in the appendix, Sect. A.3. The isotherms in both figures seem to collapse on each other at low pressure and show similar growth/melting. The data for both melting and growth clearly show that isotherms at lower temperature contain less adsorbed solid near  $P_s$ . The difference in  $n$  between the low and high temperature isotherms is a few atomic layers during both growth and melting near  $P_s$ .

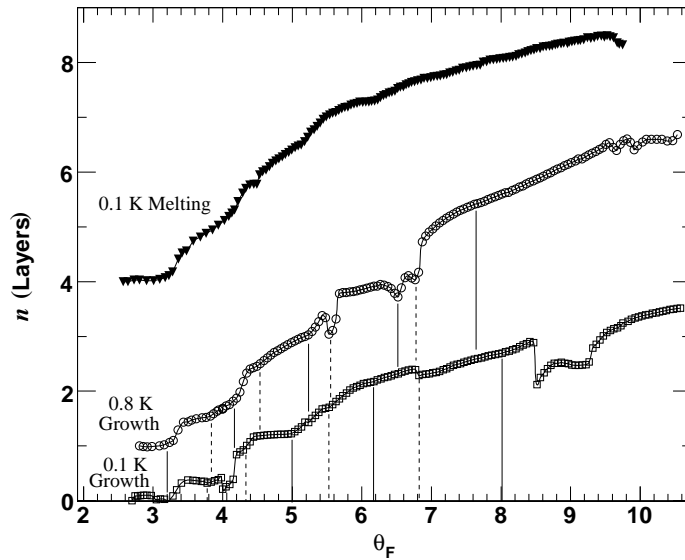


**Fig. 4.5:** Selected growth and melting isotherms from the grafoil experiment. From top to bottom: Melting at 0.1 K, growth at 0.8 K, and growth at 0.1 K. The 0.1 K melting and 0.8 K growth curves are shifted vertically for easy viewing. The horizontal axis is scaled with the Franchetti relation. Solid lines mark the onset of original layering transitions and dotted lines mark the onset of secondary transitions.

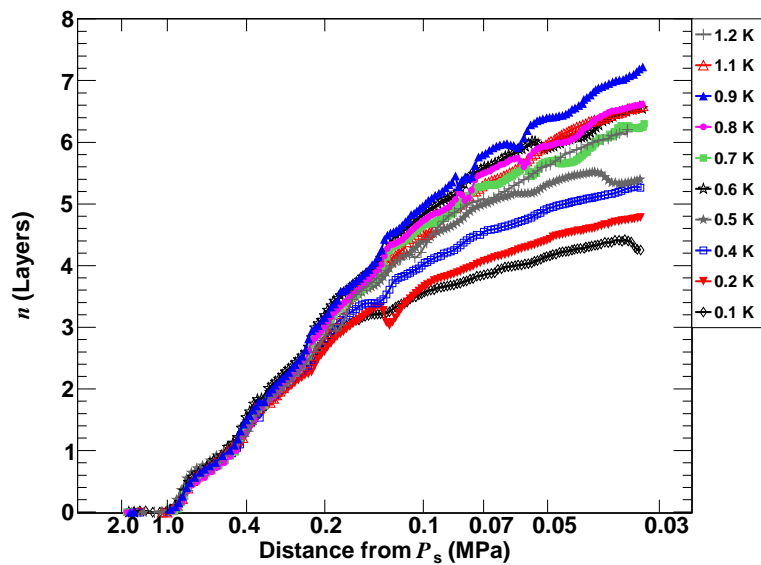


**Fig. 4.6:** Grafoil experiment  $n$  for melting isotherms from 1.2 K to 0.1 K. The horizontal axis is scaled by the Franchetti relation.

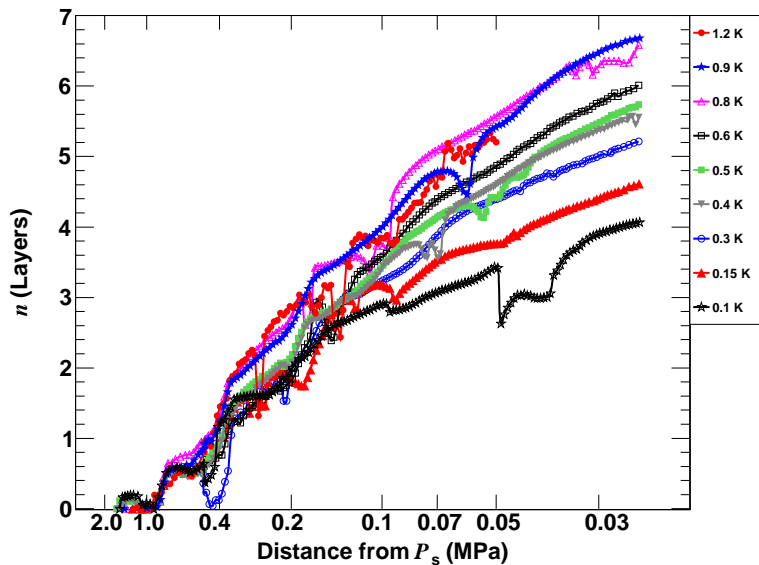


**Fig. 4.7:** Grafoil experiment  $n$  for growth isotherms from 1.2 K to 0.1 K. The horizontal axis is scaled by the Franchetti relation.

#### 4.4 Graphene Experiment: Growth Isotherms

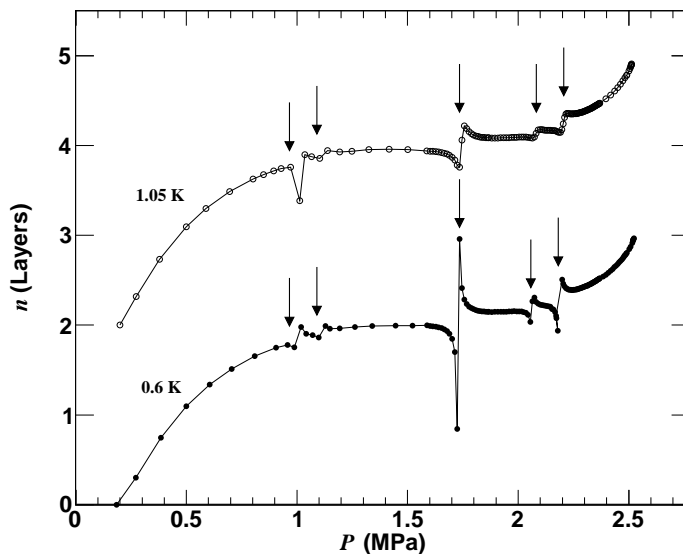


**Fig. 4.8:** Graphene experiment  $n$  for the 1.05 K and 0.6 K isotherms. Arrows mark the discontinuous jumps in solid coverage. The 1.05 K isotherm is vertically offset by 2 layers for easy viewing.

Again, the change in  $n$  was summed and the resulting growth isotherms are plotted in Figs. 4.8 and 4.9. The isotherms are also individually plotted in the appendix, Sect. A.4.

At 1.65 K (Fig. 4.9), the isotherm shows a smooth increase in the amount of solid  $^4\text{He}$  and no clear anomaly in  $Q^{-1}$  is observed. In contrast, all isotherms from 1.15 K and below exhibit striking step-like behavior with discontinuities. Each step is accompanied by an energy dissipation peak (peak in  $Q^{-1}$ ). In total, 5 discontinuities are observed within a range of one adsorbed layer. As the temperature is lowered, the discontinuities and peaks become sharper. Below 0.6 K, the isotherms are almost identical.

From 0.8 K and below, the steps are preceded by dips and subsequent "overshooting" before settling at a lower value. This behavior is most easily seen in the step at 1.72 MPa, but is visible at all five discontinuities. At the 1.72 MPa anomaly, the dip and overshoot are large than one layer. Additionally, energy dissipation is reduced during the dip in the isotherms taken at 0.6 K and below.

#### 4.4.1 Hysteresis

No hysteresis in the position or size of the discontinuities is observed between increasing and decreasing  $P$ . But, a slight difference in the shape of the isotherm is seen at  $P > 2.0$  MPa. This can be seen in Fig. 4.10, which shows an isotherm taken at 0.7 K above 1.6 MPa. The pressure was first increased from 1.6 MPa to near  $P_s$  then decreased to 1.6 MPa. The isotherm is from a different experimental run than those shown in Figs. 4.9 and 4.8, but the discontinuities occur at the same pressures and the behavior is very similar. The first data point in the 0.7 K isotherm at 1.6 MPa is assigned a value of  $n = 2.0$  for continuity with the other isotherms.

#### 4.4.2 Vibration and Annealing Effects

Helium was initially introduced into the oscillator at 4.2 K. Figure 4.11 shows data taken at 0.8 K soon after the initial filling. As shown in the inset, several liquid helium transfers (refilling the dewar which insulates the dilution refrigerator) later, the green 0.7 K isotherm was taken. The behavior is somewhat different from the 0.8 K isotherm, despite annealing the sample at 3 K overnight. The behavior seems to have changed as a result of large vibrations and pressure changes sustained during liquid helium transfers. After annealing at  $>4$  K, another measurement was taken at 0.7 K, shown in blue. Annealing at this temperature recovers the behavior of the original measurement. Finally, during a different run, the data show very similar behavior to the original 0.8 K isotherm. This is plotted as the black 0.6 K isotherm, which is the same isotherm shown

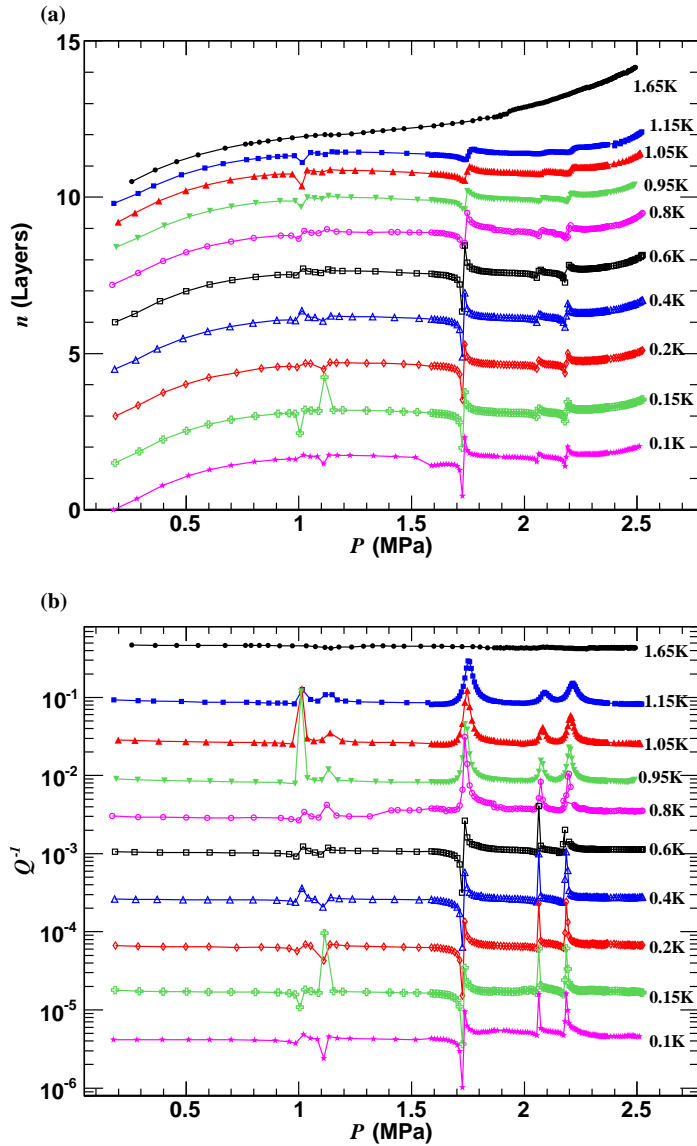


**Fig. 4.9:** Graphene experiment. (A): Solid  $^4\text{He}$  coverage for all isotherms from 1.65 K and 0.1 K. The isotherms are vertically offset for easy viewing. (B):  $1/Q$  for all isotherms from 1.65 K and 0.1 K. The isotherms are vertically offset by a multiplicative factor.

in Figs. 4.8 and 4.9 These measurements prove two important points about the data. First, annealing at above 4 K recovers the original behavior of the cell even after being heavily disturbed by large vibrations and rapid pressure changes. Second, the data is highly reproducible. Data taken from two different experimental runs show very similar behavior.

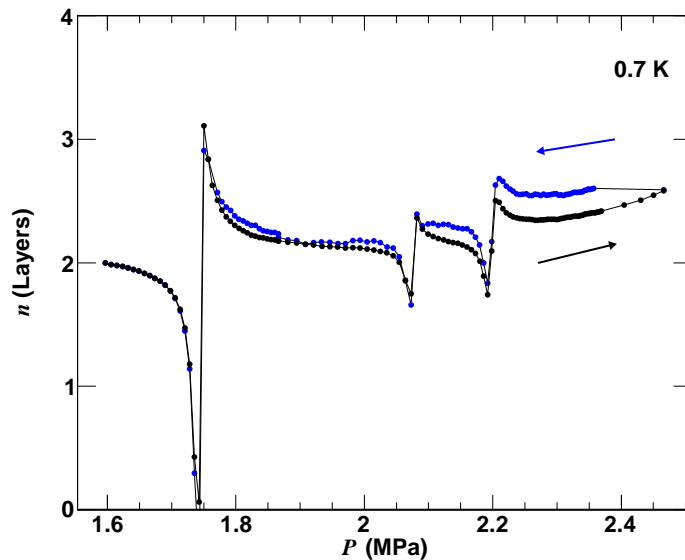


**Fig. 4.10:** Graphene experiment. Hysteresis above 1.6 MPa taken at 0.7 K. Black data points for increasing pressure and blue data points for decreasing pressure. The first point at 1.6 MPa is assigned  $n = 2.0$ .

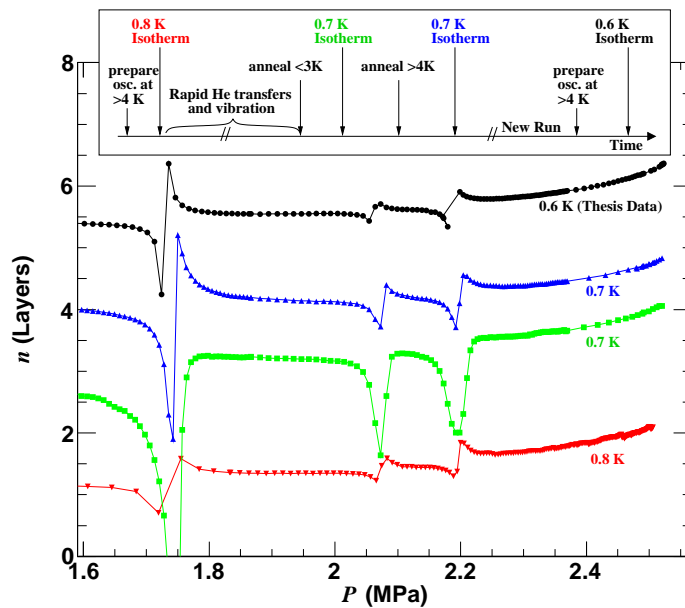


**Fig. 4.11:** Selected graphene isotherms from different experimental runs plotted together for comparison. Inset shows the chronological order in which isotherms were taken and the thermal cycling and vibrations of the cell between each isotherm. Data are offset vertically.



# 5

## Discussion: Grafoil Experiment

This chapter presents a discussion of the grafoil results. Layer-by-layer growth and melting of solid  $^4\text{He}$  on grafoil is discussed and the results are compared with previous experiments by the Penn. State and Israel groups. The two-stage layering behavior previously introduced is also discussed and an alternative explanation is offered.

### 5.1 Layer-by-layer Growth and Melting

The 1.6 K isotherm in Fig. 4.4 shows a smooth increase in the amount of adsorbed  $^4\text{He}$ , indicating continuous solid growth as a function of  $P$ . In contrast, the 1.1 K and 0.9 K isotherms have structure with bumps and kinks. Since this structure is reminiscent of torsional oscillator frequency shifts, we refer to them as shifts in  $n$ . Shifts are observed in all growth and melting isotherms from 1.2 K to 0.1 K, displayed in Figs. 4.4-4.7. We believe that these shifts represent non-continuous layer-by-layer growth/melting. We use this term to describe growth/melting that is not perfectly smooth and may show small discontinuities. We distinguish it from layering transitions, in which growth/melting theoretically proceeds via a series of whole layer discontinuities.

The  $n$  data show changing slope, suggesting periods with large amounts of solid growth/melting followed by periods with small amounts of growth/melting, in agreement with the observations made via the fourth sound (2; 4; 11). The sharp minima in the fourth sound signaled increases in the growth rate of solid  $^4\text{He}$ . Also in agreement with the fourth sound experiments is that the shifts in the 1.1 K melting isotherm, with onsets marked by solid lines, are observed approximately once per Franchetti number (horizontal axis). Interestingly, these shifts also occur about once per layer (vertical axis), similar to the observations from the differential adsorption method (3). Although the fourth sound and differential adsorption measurements claimed to be at odds with one another, the results here agree with both sets of measurements. The fourth sound

observed layer-by-layer growth via the superfluid pressure (our horizontal axis) and the differential adsorption method observed the same layer-by-layer growth through the calculated number of adsorbed solid layers (our vertical axis). Here we have shown how these two sets of measurements can be reconciled.

Discontinuous growth should occur only below the roughening temperature (10), 1.3 K (1). Indeed, as previously stated, the isotherm taken at 1.6 K is absent of shifts in  $n$ . Strictly speaking, we have not observed a series of whole layer discontinuities as predicted for layering transitions. The absence of discontinuous layer jumps may be attributable to the non-ideal nature of the grafoil substrate (16). Grafoil is made of many individual graphite platelets with average diameter usually on the order of a few tens of nm or less. The platelets show preferential alignment and a complicated pore structure, in which there are large voids connected by small necks, as sketched in Fig 5.1.

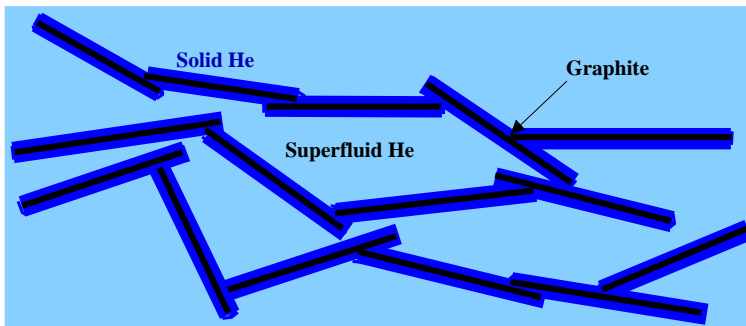


**Fig. 5.1:** Sketch of grafoil pore structure immersed in superfluid  $^4\text{He}$ .

The grafoil substrate consists of a collection of available sites to which  $^4\text{He}$  atoms can bind, thereby becoming solid. First, sites with the highest binding energies are filled with  $^4\text{He}$  atoms. As the superfluid pressure is slowly increased, sites with gradually lower energies also attract  $^4\text{He}$  atoms, and the adsorbed solid grows. On an ideal infinite substrate, the distribution of surface binding energies is a delta function, as drawn in Fig. 5.2. Thus, when the chemical potential of the liquid phase exceeds the delta function binding energy, an entire layer of solid atoms is adsorbed and the system undergoes a layering transition. Adsorption isotherms in real systems, however, can exhibit broadening (44; 45). Finite size effects (46) and substrate heterogeneities (47; 48; 49) on a real substrate result in a distribution of surface binding energies of finite width, leading to smearing of the adsorption isotherms. Nanometer sized graphite platelets can only adsorb less than  $10^3$   $^4\text{He}$  atoms at bulk density in a single layer. The distribution of binding energies on grafoil is further complicated by the area where

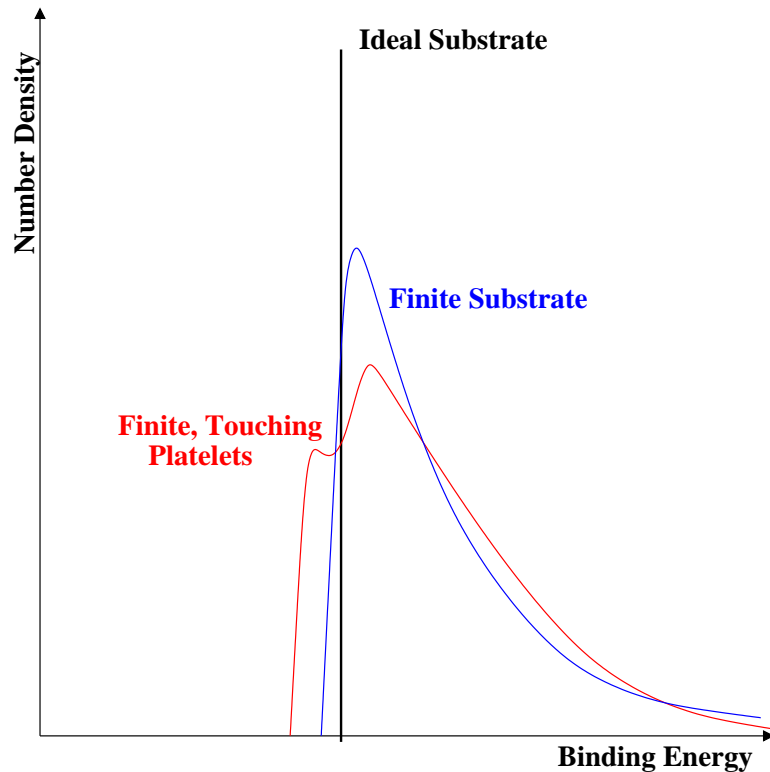


**Fig. 5.2:** Sketch of the distribution of binding energies on various substrates.

the edges of two neighboring graphite platelets come into contact or overlap. As seen in Fig. 5.1, both small and large contact angles may occur. Based on a simulation of enhanced freezing in a wedge shaped substrate (50), the contact angles of grafoil may have an enhanced attractive potential. Atoms would then be preferentially adsorbed in the contact angle of neighboring graphite platelets. The new layer grows from the contact angle, slowly spreading to the rest of the platelet, resulting in a mostly continuous adsorption isotherm

While shifts in the melting isotherms show a smooth change in  $n$ , shifts in the growth isotherms show stronger step-like structure with a few small discontinuities. The difference is especially apparent when comparing the two 0.1 K isotherms shown in Fig. 4.5. The 0.1 K growth isotherm contains extended flat regions at low layer numbers whereas the melting isotherm does not. Growth on a smooth surface requires overcoming a significant potential barrier to nucleation (24), which could lead to the flat regions in the growth isotherms. On the other hand, melting can start at the edge of the adsorbed solid crystal (51), resulting in smoother melting isotherms.

As stated before (see Sect. 2.3.3), the sharp minima of the fourth sound seemed to suggest much more discontinuous growth than the smooth isotherms of the differential

adsorption method could justify. In fact, data from differential adsorption was taken on melting, and like us, observed that the change in adsorbed solid  $^4\text{He}$  appeared mostly continuous punctuated by kinks located at integer layer numbers. The sharp minima of the fourth sound were seen during freezing (4). Similarly, we have seen stronger step-like behavior in the adsorption isotherms during freezing.

The melting data appear to have much more regular behavior (the isotherms are “prettier”) than the growth data. Pushing hot  $^4\text{He}$  into the cell when increasing  $P$  perturbs it much more than removing cold  $^4\text{He}$  from it when decreasing  $P$ .

## 5.2 Two-Stage Layer Formation

As discussed above, the 1.1 K isotherm in Fig. 4.4 shows shifts approximately once per Franchetti number and once per  $n$ , marked with solid lines. Looking at the 0.9 K isotherm reveals more complicated behavior as secondary shifts, marked with dotted lines, accompany the original shifts. Alternating original and secondary labels starting from the fourth layer results in the original transitions persisting about once per Franchetti number. One secondary transition accompanies each original one. This is in good qualitative agreement with the Penn. State Group’s observation of two-stage layer formation. The onset of original and secondary shifts at 0.9 K do not have regular coincidence with  $n$ , unlike the 1.1 K isotherm. However, it is clearly seen that each secondary stage is not the growth of an extra layer, but rather that layers are generally forming in two stages. Similar two-stage layer formation is observed in all growth and melting isotherms from 0.9 K to 0.1 K. Vertical lines marking the onset of the stages are provided for the two growth isotherms in Fig. 4.5 for comparison.

The Penn. State Group proposed that the two stages result from the difference between kink and step adsorption sites or a structural two dimensional phase transition (4). In both of these cases we expect to see a constant or at least systematic relationship between the fractional  $n$  at the original and secondary stages in each layer. According to the kink and step growth model of the Penn. State Group (see Sect. 2.3.3), the onset pressure of the secondary transition with respect to the original transition varies little with temperature. Examination of Fig. 4.5 (or a comparison of any two isotherms we have collected, for that matter) reveals that this does not hold true for our data. If each layer undergoes a structural transition, we expect to observe secondary shifts at the same non-integer  $n$  in each layer. For example, a commensurate-incommensurate transition in each layer at the  $\sqrt{3} \times \sqrt{3}$  filling should show a secondary transition occurring at each  $1/3$  layer. We have observed no such regularity in either the growth or melting isotherms. We also note that the Israel Group observed more complicated

behavior at 0.1 K compared to 1.0 K, but, like us, did not observe the regularity required for the Penn. State Group’s proposed explanations of two-stage layering.

We propose another possible explanation of two-stage layer growth which results from the substrate pore structure. From the discussion of grafoil non-ideality presented above, the point(s) where the platelets touch will experience an increase in attractive force. One possibility is that the distribution of binding energies are modified by the enhanced attraction to introduce a secondary maximum with higher binding energy. A possible sketch of this situation is drawn as the red curve in Fig. 5.2. This effect would change with the layer number (i.e. distance from the substrate) and not necessarily show systematic behavior. Furthermore, the  $^4\text{He}$  crystals adsorbed on neighboring platelets may come into contact as they grow. Crystal defects such as screw dislocations will form, creating preferential sites for additional  $^4\text{He}$  adsorption. Defect nucleation during the growth of the two crystals will change as a function of temperature, explaining why we do not observe the same size or position for coverage shifts in different isotherms.

### 5.3 Adsorbed Solid Near $P_s$

It is interesting that both 0.9 K isotherms in Figs. 4.6 and 4.7, rather than the 1.1 K or 1.2 K isotherms, show the largest amount of adsorbed solid near  $P_s$ . The amount of adsorbed solid near  $P_s$  then decreases with temperature. The lowest temperature isotherms at 0.1 K show up to 3 less solid layers than the 0.9 K isotherms.

Following the explanation of substrate structure and crystals on neighboring graphite platelets coming into contact with one another, dislocations between mismatching lattices may not form as easily at low temperature. As dislocations are suppressed, neighboring crystals will be less likely to grow together and provide preferential sites for  $^4\text{He}$  adsorption. Depending on the contact angle of neighboring graphite platelets, the adsorbed crystals are more likely to touch at high layer numbers, thus making the temperature effect on dislocations more pronounced. The isotherms collapse on one another and show very similar behavior at low layer number and start to “spread out” at high layer number.

### 5.4 Dips in the Isotherms

Close examination of both the growth and melting isotherms reveals that the end of some of the  $n$  shifts are marked by small dips in the isotherms. One possible interpretation is that this is melting of adsorbed solid with increasing  $P$ . The Israel Group also saw small dips at the completion of each layer. They surmised that the dips could also

be explained by a small change in density at the completion of each layer. As discussed in section 2.4.1, the first two layers on graphite are known to have a higher density than bulk solid  $^4\text{He}$ . Since the effect of the substrate decreases with distance from it, as  $n$  increases, the adsorbed solid is often thought to approach that of bulk density. If each layer adsorbs at a slightly higher density than bulk solid, dips in the isotherm at the completion of each layer may result from a transition to bulk solid density.

### 5.5 Energy Dissipation ( $Q^{-1}$ )

Peaks in  $Q^{-1}$  are sometimes coincident with the shifts in  $n$ . This can be seen in section A.3, where each isotherm is plotted individually. It is not surprising because solid growth, especially on a smooth surface, requires overcoming a potential barrier (24). The peaks in energy dissipation show varied behavior with temperature and do not consistently appear with each shift in  $n$ . This may be another result of the unideal substrate structure and its changing effect on the growth as a function of temperature and  $n$ .

# 6

## Discussion: Graphene Experiment

This chapter discusses the graphene results. Discontinuous growth of solid  $^4\text{He}$  on the graphene sample is observed. We propose an explanation in which the uppermost solid layer grows through a series of 2D phase transitions through several commensurate and incommensurate phases.

### 6.1 A More Ideal Substrate than Grafoil

The isotherm taken at 1.65 K in Fig. 4.9 shows a smooth increase in the amount of solid  $^4\text{He}$  and no clear anomaly in  $Q^{-1}$  is observed. Again, this indicates continuous solid growth. From 1.15 K and below, the solid growth is discontinuous and looks to have much more ideal step-like structure than the growth on grafoil. There are extended flat regions separated by sharp jumps in  $n$ . We suppose that the larger platelet size and more ideal structure of the graphene results in a more ideal substrate than grafoil.

The total amount of solid adsorption on graphene platelets is about 3 layers when compared to 4 to 7 layers on grafoil. Figure 6.1 shows several selected freezing isotherms from both the grafoil and graphene cell for comparison. Decreased solid growth may be due to graphene's weaker adsorption potential and the absence of a tortuous pore structure. In particular, the wedge shapes resulting from the contact and overlap of neighboring graphite platelets can provide nucleation sites for solid adsorbed on grafoil.

Another result of the more ideal graphene substrate is the regularity of the isotherms. Without the unideal pore structure of grafoil, there should be little change in the  $n$  position of each discontinuity or overall solid adsorption with temperature. Indeed we have observed that each isotherm below  $T_R$  contains 5 discontinuities accompanied by a peak in  $Q^{-1}$ . The total adsorption on graphene varies less than 0.3 layers over the

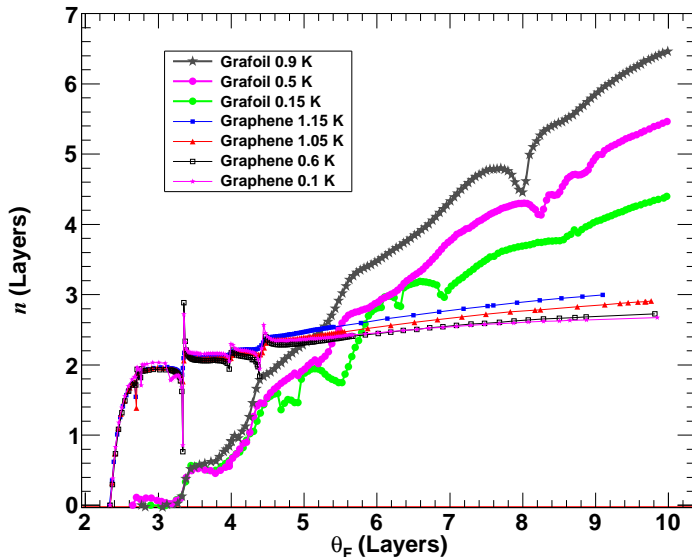


**Fig. 6.1:** Selected grafoil and graphene freezing isotherms plotted together for comparison. The horizontal axis is scaled using the Franchetti relation.

temperature range studied in comparison with several layers on grafoil. Basically all of the variation in the graphene isotherms is found after the highest pressure discontinuity.

The pressure of each discontinuity becomes slightly lower as  $T$  is decreased and is unchanging from 0.8 K and below, as seen in Fig. 4.9. Since the theoretical amount of adsorbed solid calculated from the Franchetti Relation (Eq.2.12) is a function of the distance from  $P_s$ , a small change in the position of each discontinuity is expected as the melting curve shifts upward starting around 1 K.

## 6.2 2D Structural Transitions

Five discontinuities are observed during the growth of less than one layer. This is much more than one or two (one above 0.95 K and two below 0.95 K with the onset of two-stage growth) transitions seen per layer in solid growth on grafoil. A very compelling interpretation is that the step-like discontinuities originate from structural transitions of the uppermost layer, rather than multiple layer-by-layer growth as seen on grafoil. Each flat region in the adsorption isotherms represents a 2D structure in the uppermost layer; each discontinuity is a transition from one structure to another.

As explained in section 2.4.1, 2D solid  $^4\text{He}$  adsorbed on graphite (31; 32) and graphene (35) exhibits various solid phases such as commensurate phases, domain wall structures, and incommensurate phases. It is possible that the large size of the indi-

vidual graphene platelets employed here facilitates much longer range order than the nm-sized grafoil platelets, making various 2D solid structures readily observable.

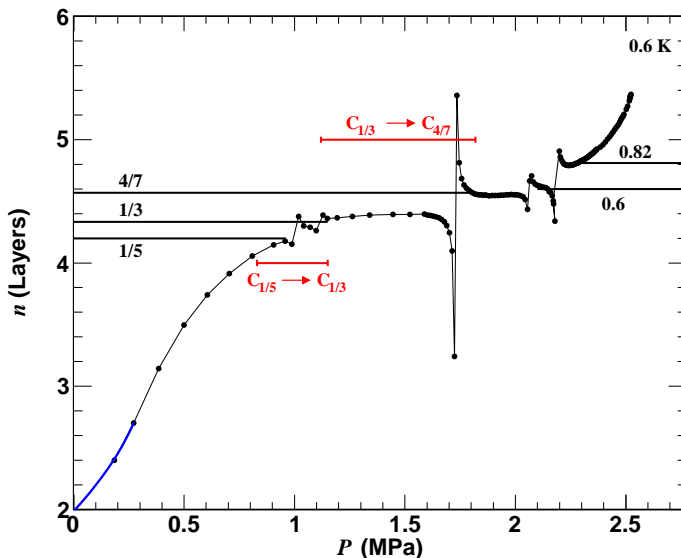


**Fig. 6.2:** The 0.6 K graphene isotherm offset vertically. The solid blue line shows the extrapolation to  $P = 0$  MPa (see text). Horizontal lines mark fractional  $n$  in the fifth layer. Red horizontal bars mark pressure differences between the labeled commensurate phases (see text).

To estimate the absolute number of adsorbed solid layers, we first note that the first two layers in thin film experiments are solid with subsequent layers fluid on graphite. We therefore believe that it is reasonable to assume that there are two layers adsorbed on the graphene at  $P = 0$  MPa. Additionally, the Franchetti Relation predicts about 2.07 layers on graphene at 0 MPa. Well below the roughening temperature the surface of the adsorbed solid should be smooth, most likely with a value of 2.0 layers.

Since our data start at 0.2 MPa, we extrapolate to 0 MPa and introduce a vertical offset to our calculated  $n$  so that  $P = 0$  MPa corresponds to  $n = 2$ . This is shown in Fig. 6.2, where the vertical offset was determined to be  $n = 2.4$ . The extrapolation to  $P = 0$  MPa was performed by eye and is drawn as the blue line. Horizontal lines mark fractional  $n$  that approximately correspond to the flat regions of the isotherm. **Note that we could also infer the labeled fractions/decimals based on the density change at each discontinuity.** So, we are not completely dependent upon the assumption that  $n = 2$  at  $P = 0$ . Figure 6.3 shows all isotherms plotted together with the same offset. The flat areas in all isotherms approximately agree with the labeled fractional  $n$ .

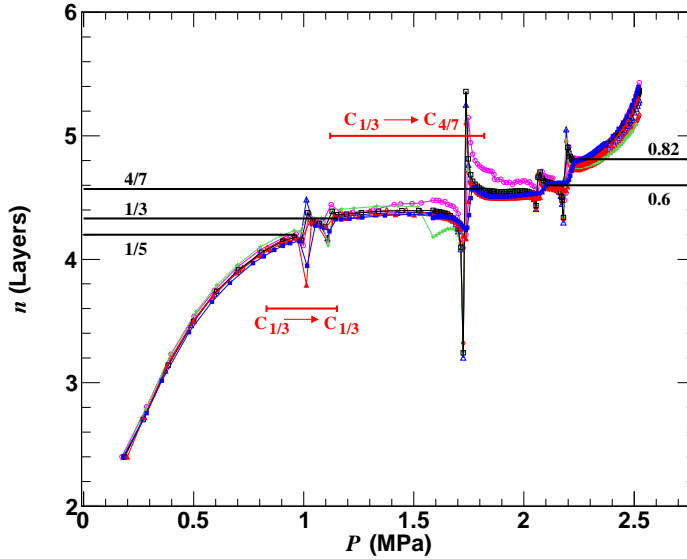


**Fig. 6.3:** All graphene isotherms below 1.2 K offset vertically. The solid blue line shows the extrapolation to  $P = 0$  MPa (see text). Horizontal lines mark fractional  $n$  in the fifth layer. Red horizontal bars mark pressure differences between the labeled commensurate phases (see text).

The first three fractions,  $1/5$ ,  $1/3$ , and  $4/7$ , may be structures in the fifth layer commensurate with the completed fourth layer. The partial filling 0.6 has been observed by the Israel Group (3) on grafoil. 0.82 may be an incommensurate solid phase.

### 6.2.1 $1/5$

The fraction  $n = 1/5$  may be a structure commensurate with the underlying completed helium layer.  $1/5$  is a convenient fraction that fits the data and a possible commensurate structure is drawn in Fig. 6.4.  $1/5$  of available adsorption minima are occupied by adsorbate  $^4\text{He}$ .

### 6.2.2 $1/3$

A commensurate  $1/3$  phase is known to occur in various monolayer adsorbates such as  $^4\text{He}$  (32) and krypton (52) on graphite. The well known structure, sketched in Fig. 6.5, has  $1/3$  of the available potential minima occupied by adsorbate atoms. Although this structure is often seen as commensurate with graphite, here, we propose that it is commensurate with the underlying solid  $^4\text{He}$  layer.

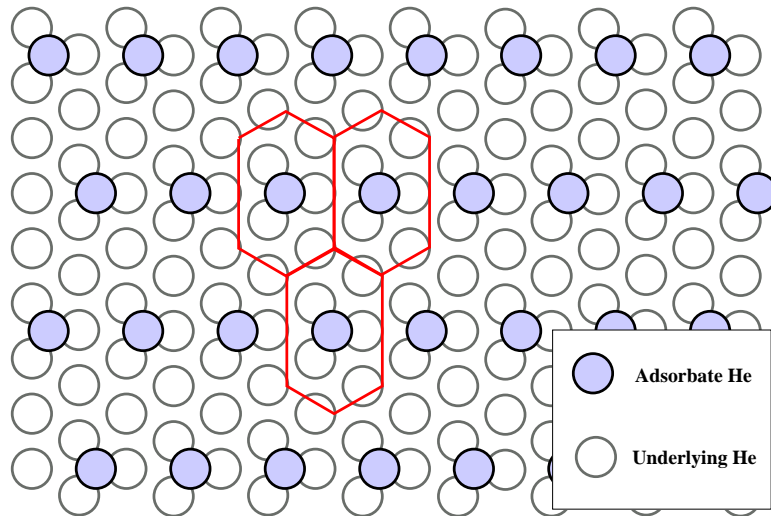


**Fig. 6.4:** A possible  $1/5$  commensurate structure. Red hexagons show the in-plane confinement (see Sect. 6.3.2).

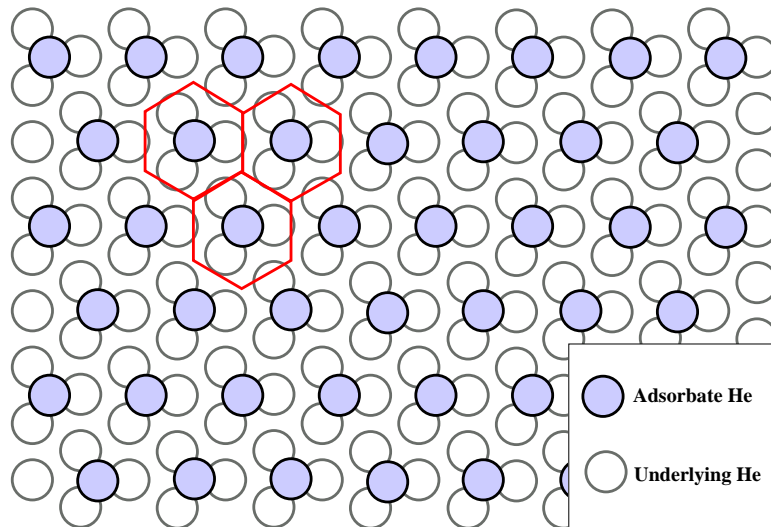


**Fig. 6.5:** The well known  $1/3$  commensurate structure. Red hexagons show the in-plane confinement (see Sect. 6.3.2).

### 6.2.3 $4/7$

A  $4/7$  commensurate structure is known to occur in the second layer of  $^4\text{He}$  (32) and  $^3\text{He}$  (53) adsorbed on graphite. This is commensurate with the underlying helium layer and a structure proposed by Elser (5) is drawn in Fig. 6.6. The adsorbate layer has hexagonal symmetry but none of the atoms sit in potential minima created by the underlying helium layer. There are two possible adsorption sites: A and B. A atoms are three times more common than B atoms and sit at saddle points, as shown in Fig. 6.6.

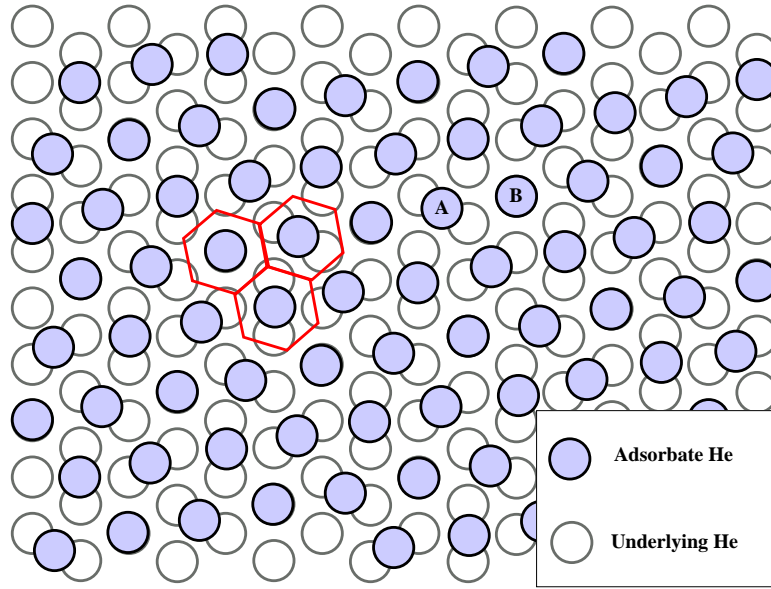


**Fig. 6.6:** 4/7 commensurate structure proposed by Elser (5). Red hexagons show the in-plane confinement (see Sect. 6.3.2).

B atoms sit at potential maxima.

#### 6.2.4 0.6

The Israel Group observed a transition at a partial  $n$  of 0.6. Figure 6.7 shows their observation. They proposed that this represented the  $\sqrt{3}\times\sqrt{3}$  phase commensurate with graphite. We adopt this interpretation for the flat region corresponding to  $n = 4.6$  in Fig. 6.2.

#### 6.2.5 0.82

Simulations (31) have seen that the second layer of  $^4\text{He}$  adsorbed on graphite becomes an incommensurate solid at a second layer density of  $0.076 \text{ \AA}^{-2}$ . Heat capacity measurements (54) have shown that the second layer completes at a density of  $0.092 \text{ \AA}^{-2}$ . Thus, incommensurate solid in the second layer of  $^4\text{He}$  adsorbed on graphite starts at partial  $n = 0.82$ . This agrees with the highest pressure flat region in our data. Furthermore, because the lattice constant of an incommensurate solid can be continually compressed, the growth of the incommensurate solid should appear continuous. Indeed, the isotherm in Fig 6.2 is continuous after the transition to an incommensurate solid.

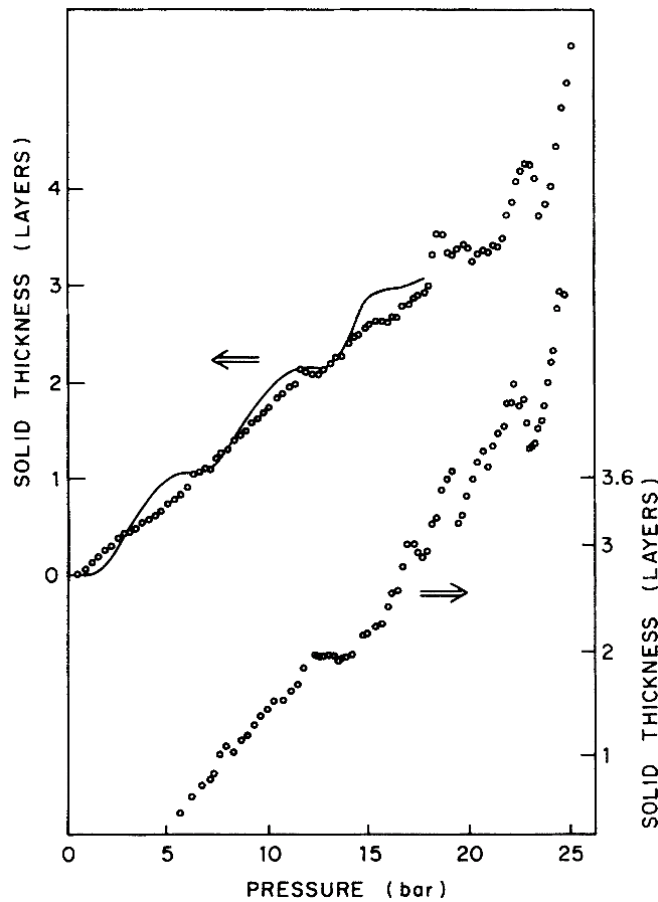


**Fig. 6.7:** Transition observed by the Israel Group at a fractional  $n = 0.6$ . Figure taken from (3), copyright (1984) by the American Physical Society. Red arrow (marking the transition at 3.6 layers) and labels added for clarity.

### 6.2.6 Discontinuous Growth Below $T_R$

On graphene, as on grafoil, the solid growth is continuous above  $T_R$  and discontinuous below. Recall that  $T_R$  is the roughening temperature for the c-facet of  $^4\text{He}$  and is independent of the substrate. Above  $T_R$ , continuous growth makes it difficult to define each solid layer. Without clear definition of a single solid layer, 2D transitions within that layer would be obscured. It is, therefore, not surprising that we have observed discontinuities in the isotherms only below  $T_R$ .

One may notice that discontinuities are not observed in the two layers grown below 1.0 MPa. The observation of commensurate and incommensurate phases requires a delicate balance between the substrate and interatomic  $^4\text{He}$  potentials. This may not occur in every adsorbed layer.

As the temperature is lowered, the discontinuities and  $Q^{-1}$  peaks become sharper.

Close to  $T_R$ , thermal excitations such as adatoms on the crystal surface or dislocations in the 2D crystal structure smear the discontinuous solid growth. As the temperature is lowered, these excitations are suppressed, leading to sharper steps.

### 6.3 Estimation of Commensurate Structure Energies

To strengthen the claim that the uppermost layer undergoes various 2D structural transitions, we calculate the internal energy of the proposed commensurate phases (1/5, 1/3, and 4/7) and use the internal energy differences between the phases to predict the difference in  $P$  between the phases.

#### 6.3.1 Internal Energy of Helium

Following London (55), the internal energy per helium atom is given by

$$U = \Phi + E^0 \tag{6.1}$$

$$\Phi = \sum \phi \tag{6.2}$$

$$E^0 = \frac{h^2 d}{2\pi m (V^{1/3} - 0.891d)^2 (V^{1/3} + 0.731d)}, \tag{6.3}$$

where  $\Phi$  is the potential energy given as the sum of interaction energies between individual helium atoms and  $E^0$  is the zero point motion.  $V$  is the “confining” volume for an atom,  $m$  is the mass of the confined atom, and  $d$  is 2.3 Å (found by London from fitting physical data).

#### 6.3.2 Internal Energy of Phase $C_i$ , $U(C_i)$

Using Eq. 6.1,  $U(C_i)$ , the internal energy of a given commensurate phase  $C_i$ , is estimated.  $\phi$  is taken as the Lennard Jones potentials between individual  $^4\text{He}$  atoms. The 6-12 Lennard Jones potential of  $^4\text{He}$  is (56)

$$\psi = 4\varepsilon \left[ \left(\frac{\sigma}{r}\right)^{12} - \left(\frac{\sigma}{r}\right)^6 \right] \tag{6.4}$$

with  $r$  the distance between atoms,  $\varepsilon = 10.8$  K, and  $\sigma = 2.57$  Å.  $\Phi(C_i)$  is calculated as the sum over first nearest neighbors.

$$\Phi(C_i) = \sum_{\text{n.n.}} \phi(C_i) + J_L. \tag{6.5}$$

Each atom in the uppermost layer has solid nearest neighbors in the underlying layer as well as the same layer. The distance between atoms is determined by the structure of  $C_i$ . Since we are interested in the energy per atom, the interaction energy within

the same layer should be halved to avoid overcounting (i.e. count only 3 of the 6 lateral bonds). In principle  $\Phi$  also contains Lennard Jones terms with the neighboring superfluid. We assume this interaction is independent of the structure  $C_i$  and therefore write it as the constant  $J_L$ .

The zero point energy is calculated by assuming each atom in the uppermost layer is confined to a hexagonal prism. The hexagonal base is defined by the structure  $C_i$  and is drawn in Figs. 6.4 to 6.6 as red hexagons. Confinement in the direction perpendicular to the substrate was assumed to be  $3.76 \text{ \AA}$ , which is the same confinement experienced by the liquid based on its density.

### 6.3.3 Condition for the Growth of $C_i$

Let  $P_i$  be the pressure at which  $C_i$  freezes from the liquid.  $P_i$  should be the pressure at the beginning of a flat region just after a discontinuity in the isotherm. Then,

$$U(C_i) = \mu_L(P_i) + \frac{\alpha}{h^3} + C. \quad (6.6)$$

Here,  $\mu_L(P_i)$  is the chemical potential of the liquid given as

$$\mu_L(P_i) = \mu_L(0) + \int_0^{P_i} V_m dP, \quad (6.7)$$

where  $V_m(P)$  is the liquid molar volume as a function of pressure and  $\mu_L(0)$  is simply the latent heat of vaporization taken with a minus sign (57).  $\frac{\alpha}{h^3}$  is the van der Waals potential of the substrate acting on the uppermost solid layer and  $h$  is the distance from the substrate to the uppermost layer.  $C$  accounts for other constant terms such as the latent heat of fusion.

### 6.3.4 Internal Energy Difference Between Two Commensurate Phases

$$\Delta U(C_i \rightarrow C_j)$$

To apply this energy calculation to our data, we find the difference in internal energy between two commensurate phases  $\Delta U(C_i \rightarrow C_j) = U(C_j) - U(C_i)$ .

$$\Delta U(C_i \rightarrow C_j) = \sum \phi(C_j) + E^0(C_j) - \sum \phi(C_i) - E^0(C_i) = \int_{P_i}^{P_j} V_m dP. \quad (6.8)$$

Calculating the difference  $\Delta U(C_i \rightarrow C_j)$  allows us to cancel quantities such as  $J_L$  that are not easily estimated. Since all  $C_i$  are observed in the same layer, the substrate's van der Waals potential is a constant and also cancels.

We calculate  $\Delta U(C_{1/5} \rightarrow C_{1/3})$  and  $\Delta U(C_{1/3} \rightarrow C_{4/7})$  using the structures shown in Figs. 6.4 to 6.6. Because adsorbed atoms in Elser’s  $C_{4/7}$  do not sit in the potential minima of the underlying layer, second nearest neighbors in the underlying layer become important and are accounted for in  $\sum \phi(C_{4/7})$ . For each  $\Delta U$ ,  $P_i$  and  $P_j$  are chosen to satisfy Eq. 6.8. The chosen  $P_i$  and  $P_j$  are plotted as the red bars in Fig. 6.2. This calculation, although approximate, agrees with our data.

## 6.4 Dips and Overshoots

In the most prominent discontinuity, seen at 1.72 MPa, the isotherms show a large dip and an overshoot of nearly one layer. Recall that the cell comes to equilibrium at each data point. The same behavior is also clearly seen at the two discontinuities above 2.0 MPa, but the dip and overshoot are smaller. Possible reasons for this behavior are speculated and evaluated.

We have found that the dissipation peak always coincides with increases in the adsorption isotherms. During the dip that precedes each step, energy dissipation decreases.

### 6.4.1 Melting and Freezing

One possible interpretation is that the adsorbed solid melts and freezes with increasing  $P$ . If each flat region represents a different 2D solid phase, then the dips and overshoots would be melting and overshooting freezing between each 2D solid phase.

Transitions from one 2D structure to another can proceed by the formation of domain walls (58). It has been shown that adsorbates on a hexagonal lattice can contain a fluid phase between commensurate and incommensurate solid phases (59; 60). When the adsorbed solid starts to transition from the commensurate to incommensurate phase, domain walls form. In the presence of dislocations, the domain walls can become unstable and the solid melts into a domain wall fluid. As the adsorbate grows, more domain walls form and the net repulsive force between them resolidifies the crystal into the incommensurate phase. Observations of such a domain wall fluid phase have been made in 1 to 2 layer krypton adsorbed on graphite (61) for a transition from a  $\sqrt{3} \times \sqrt{3}$  commensurate phase (1/3 filling) to an incommensurate phase. According to the theory (59), the existence of a fluid phase is predicated on the adsorbed solid being weakly commensurate (i.e. large average distance between domain walls). In the case of krypton, the free lattice constant is only slightly smaller than that imposed by the graphite substrate (52).

As seen in Fig. 6.2, fractional fillings of the fifth layer before and after the largest dip are approximately  $1/3$  and  $4/7$ , respectively. The density difference between the  $1/3$  and  $4/7$  phases seems too large to qualify for the same domain wall fluid seen in krypton on graphite. But, a similar type of melting may explain the dips observed. A domain wall fluid phase should be more easily seen at high temperature due to the thermal excitation of destabilizing dislocations. The graphene data shows that the dips and overshoots become larger with lower temperature. If one believes that a domain wall fluid can still form in the  $^4\text{He}$ -graphene system, the observation of melting at low temperature may be due to rotons. Roton scattering against solid  $^4\text{He}$  surfaces is known to provide resistance to solid growth (62; 63). Below 0.8 K very few rotons exist in the superfluid (64), allowing the surface to move freely, thus giving rise to rapid melting and overshooting growth.

### 6.4.2 Layer Density Change

As proposed by the Israel Group, dips (and possibly overshoots) can also be the result of density changes in the last adsorbed layer. While a small density change may seem possible, it seems quite unlikely that this could account for one entire layer change in the adsorption isotherms as seen at 1.72 MPa. The density of the last adsorbed layer would need to become zero. That is that the layer would melt. If the dip and overshoot are considered, it is difficult to believe that the density would decrease, suddenly increase, then decrease again to a lower value. Finally, why this effect would increase in size as the temperature is lowered is unknown.

### 6.4.3 Adsorbed Solid Roughness

Ideally, liquid  $^4\text{He}$  decouples from the torsional oscillator when it becomes superfluid. Superfluid can, however, be trapped by the sample and dragged with the oscillation. Superfluid that couples to the oscillation acts to increase the rotational inertia. Coupling often occurs in a tortuous sample or at the walls of the sample container, and the superfluid background  $f_L$  takes this into account. As depicted in Fig. 6.8, it may also be possible for the superfluid to couple to the oscillation in the roughness of the adsorbed solid. Superfluid coupled in this manner cannot be distinguished from adsorbed solid.

Far below  $T_R$ , the surface is theoretically smooth. But if the solid grows through successive 2D structural transitions, each 2D structure could have some effective roughness. Figure 6.8(B) shows adatoms adsorbed with regular spacing in the top layer and superfluid partially coupling to the oscillation because the lattice spacing is large. Although the lattice spacing is not large enough to allow complete penetration of the

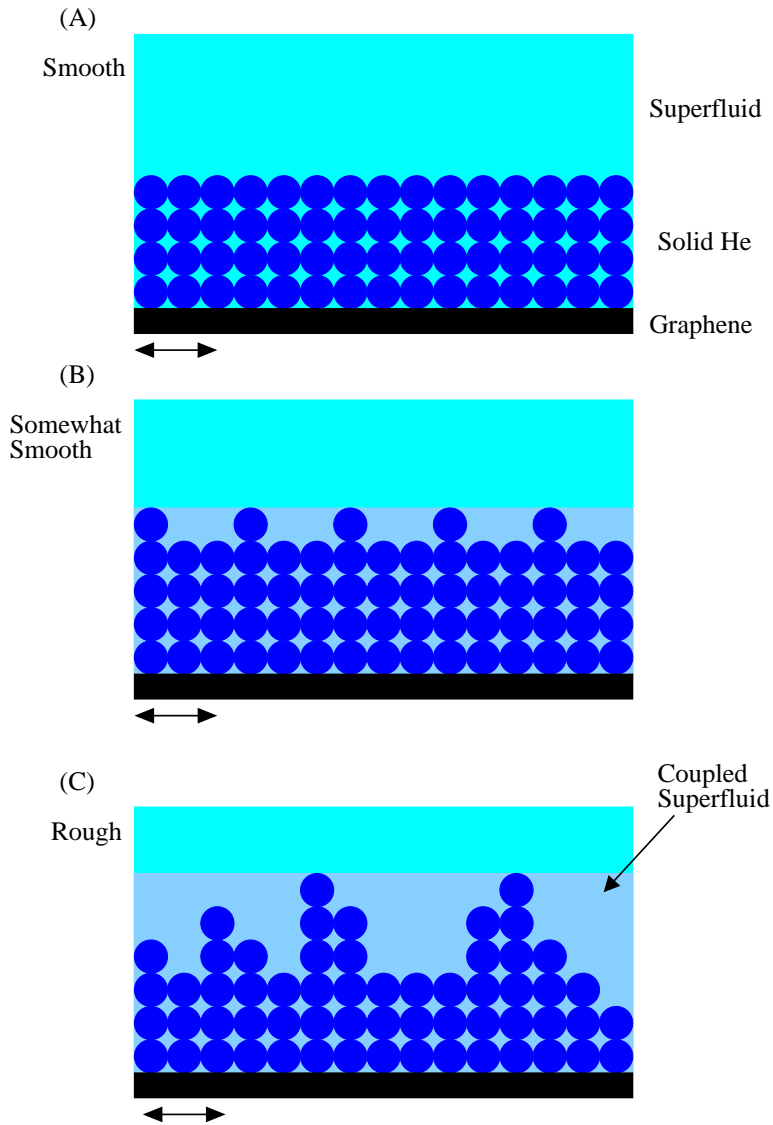


**Fig. 6.8:** Sketch of a (A) smooth surface, (B) somewhat smooth surface, and (C) rough surface. Some superfluid trapped in the roughness couples to the torsional oscillator motion.

superfluid, there may be partial coupling in the effective roughness of the solid surface. If the surface transitions to a rough state, as may happen when domain walls form during the transition from one 2D phase to another, there would be increased coupling of the superfluid to the torsional motion. This could manifest as the observed overshoot.

# 7

## Conclusion

The adsorption of solid  $^4\text{He}$  on grafoil and graphene from the superfluid phase was studied using the torsional oscillator method at temperatures from 1.65 K to 0.1 K. At 1.6 K and above, continuous growth was observed. Below 1.3 K, the adsorption isotherms on grafoil contain kinks and on graphene they have strong step-like structure with large discontinuities.

Growth and melting measurements on grafoil contain shifts in the resonant frequency and patterns of energy dissipation. We have converted the frequency into adsorption isotherm and seen that the amount of adsorbed solid grows and melts in a non-continuous manner. The isotherms contain shifts in the amount of adsorbed solid that occur approximately once per layer, indicating layer-by-layer growth. Although the solid adsorption theoretically occurs with step-like, whole-layer discontinuities (10), the isotherms are mostly smooth and punctuated with kinks and bumps.

Below 0.95 K, we have confirmed the observation of two-stage layering made by the Penn. State Group (4) and shown that the secondary stage is not the growth of additional layers, but rather that layers are mostly forming in two stages. Furthermore, close to  $P_s$ , less solid is adsorbed on the grafoil at low temperature; there are up to 3 layers less adsorbed at 0.1 K compared to 0.9 K

The grafoil substrate is far from ideal with average platelet sizes on the nm order and a tortuous pore structure. We propose that the non-ideality may be responsible for the mostly smooth adsorption isotherms, the irregularity seen in two-stage layering, and the peculiar observation of less adsorbed solid at low temperature

Growth measurements on graphene have also been performed. The average platelet diameters of the graphene are on the  $\mu\text{m}$  order, much larger than grafoil. Also, there is no tortuous pore structure. The isotherms show step-like structure with discontinuities that are each accompanied by a clear energy dissipation peak. The discontinuities and energy dissipation peaks are regularly seen in all isotherms below 1.3 K. The total

adsorption is nearly the same at all temperatures. This more ideal behavior may stem from the more ideal nature of the graphene substrate employed here.

In total, 5 discontinuities occur during the growth of a single layer, suggesting that the solid growth mechanisms are much more complicated than simple layering transitions. We propose an interpretation in which the uppermost solid layer grows through successive transitions between various commensurate and incommensurate structures. Each flat regime corresponds to a different two-dimensional structure and each discontinuity is a transition from one structure to another. A rough estimate of the internal energy is made for each proposed commensurate structure. The differences in internal energy between commensurate structures approximate the observed pressure differences between flat regions in the data.

As the temperature is lowered, the discontinuities and energy dissipation peaks become sharper. From 0.8 K and below, dips and overshoots of as much as one solid layer precedes each discontinuity.

Further theoretical work and experiments are needed to elucidate the nature of solid  $^4\text{He}$  growth on graphite and graphene.

# Appendix A

## Appendix

### A.1 Sample Surface Area Measurements: Nitrogen Adsorption

The surface area of the grafoil and graphene samples were determined by nitrogen adsorption using the BET method (39).

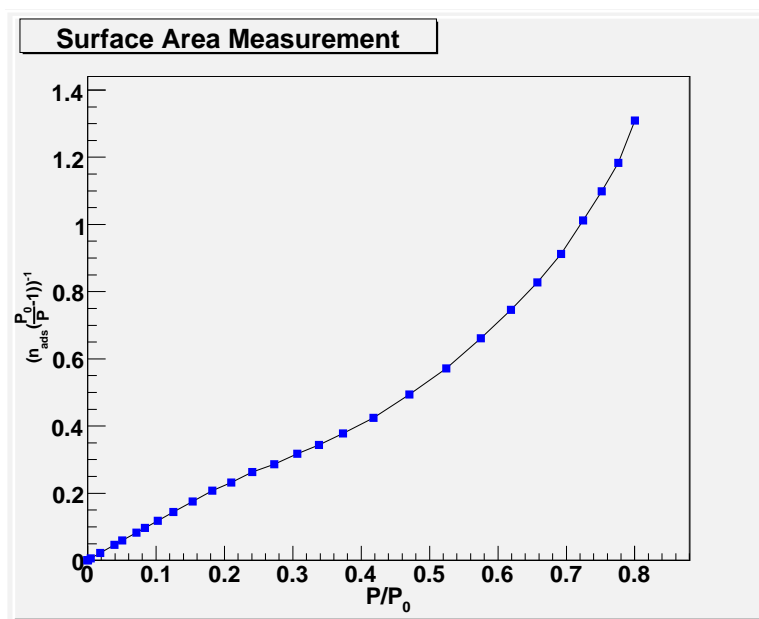


Fig. A.1: Nitrogen adsorption isotherm for the grafoil sample.

Measurements for the grafoil sample were made by hand and are shown in Fig. A.1. The data used for the BET fit, plotted in Fig. A.2, yielded a surface area of  $120 \text{ m}^2$  and a specific surface area of  $21 \text{ m}^2/\text{g}$ , a typical value for grafoil.

Measurements for the graphene sample were automated on a Belsorp Mini and are

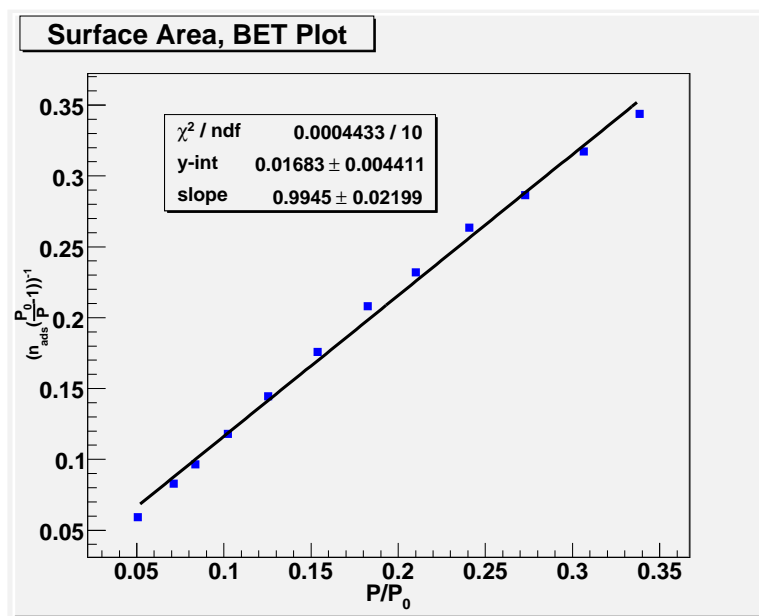


Fig. A.2: BET fit for the grafoil sample.

shown in Fig. A.3. The data used for the BET fit, plotted in Fig. A.4, yielded a surface area of 28 m<sup>2</sup> and a specific surface area of 85 m<sup>2</sup>/g, less than the manufacturer's specifications. However, some loss of surface area is expected from the compression needed to fix the sample into the torsional oscillator bob.

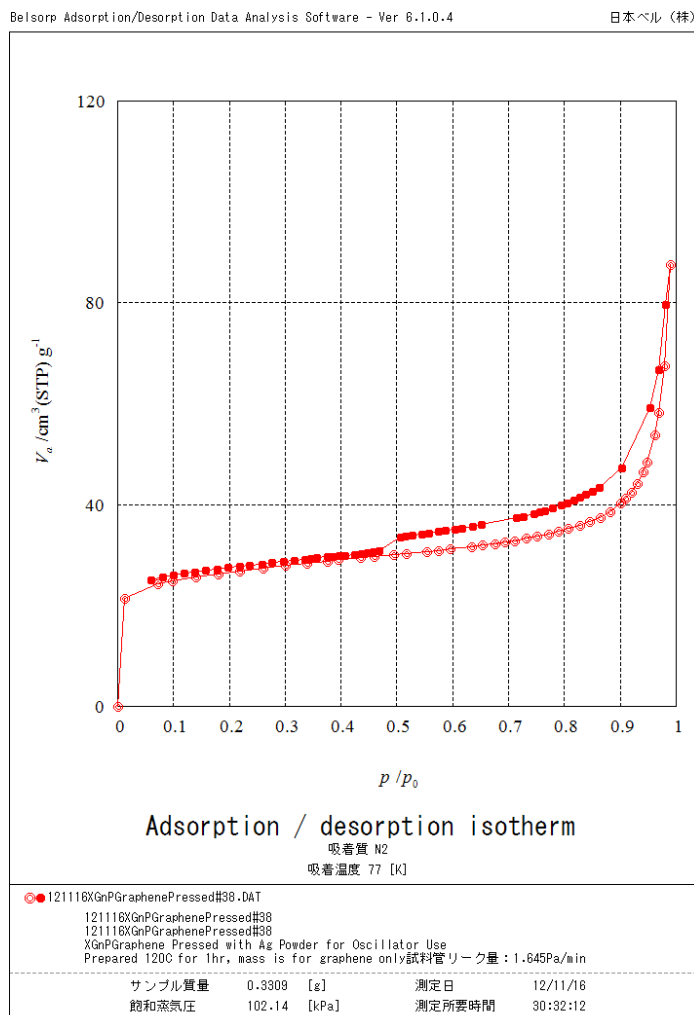


Fig. A.3: Nitrogen adsorption isotherm for the graphene sample.

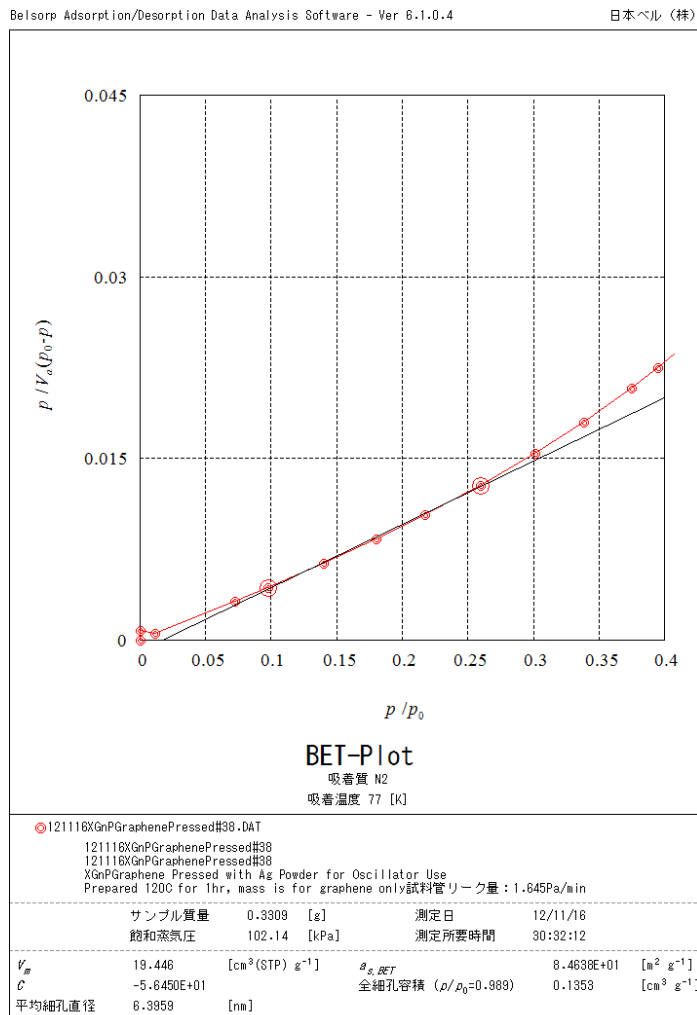


Fig. A.4: BET fit for the graphene sample.

## A.2 Temperature Dependence: Empty Cell and Low Pressure Measurements

This section presents data taken at constant pressure as a function of temperature. The data of the empty cells are shown in Figs. A.5 and A.7. Data taken at low pressure and used to fit  $f_L$  are shown in Figs. A.6 and A.8.

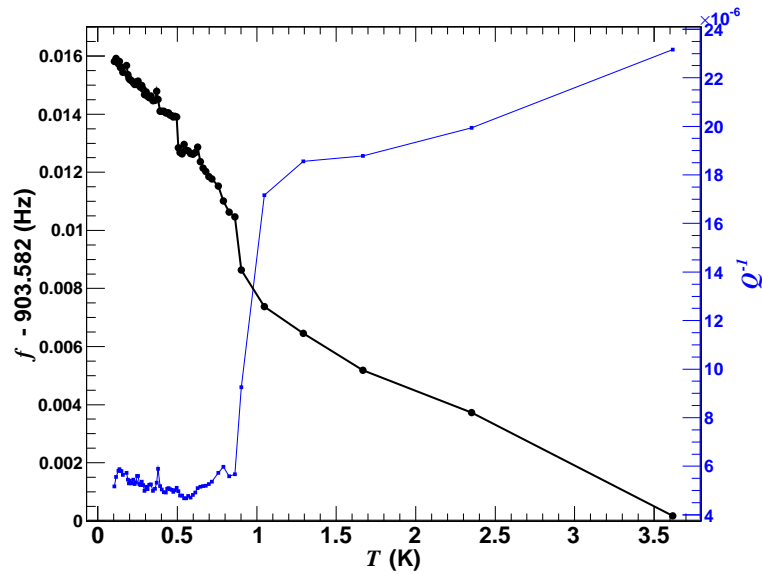


Fig. A.5: Grafoil empty cell data.

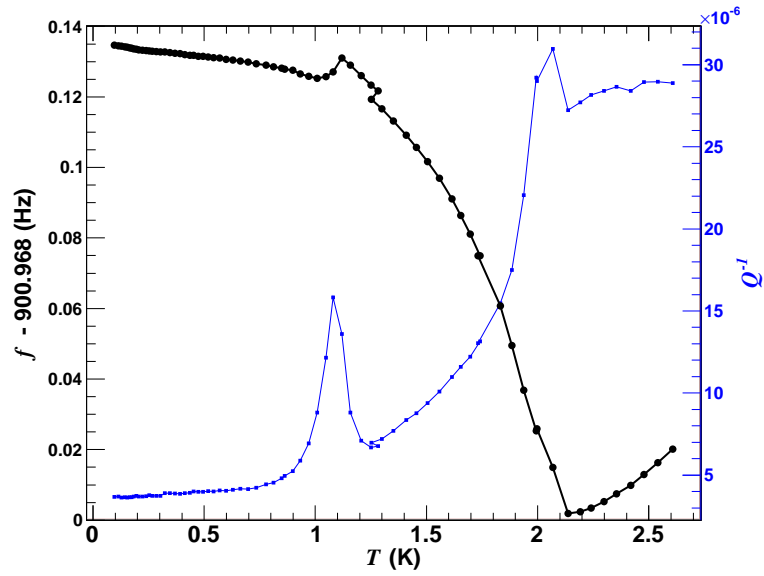


Fig. A.6: Grafoil data as a function of temperature at 0.5 MPa. Used to find  $f_L$ .

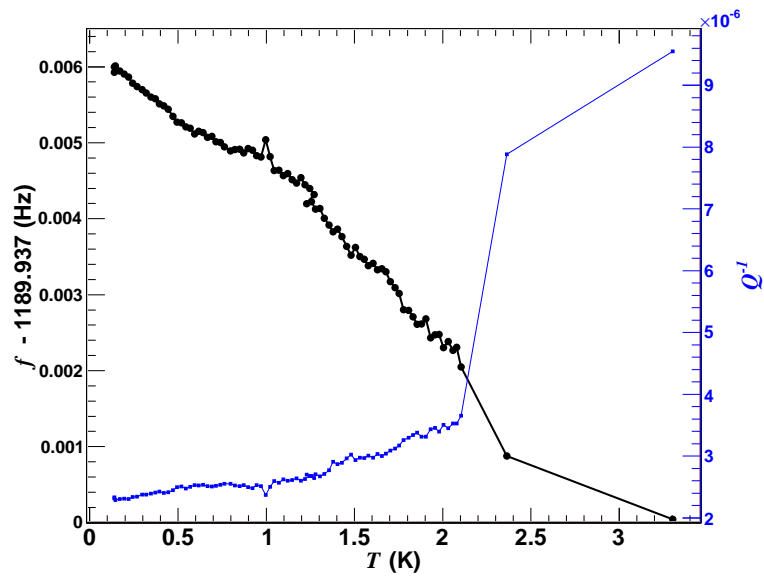


Fig. A.7: Graphene empty cell data.

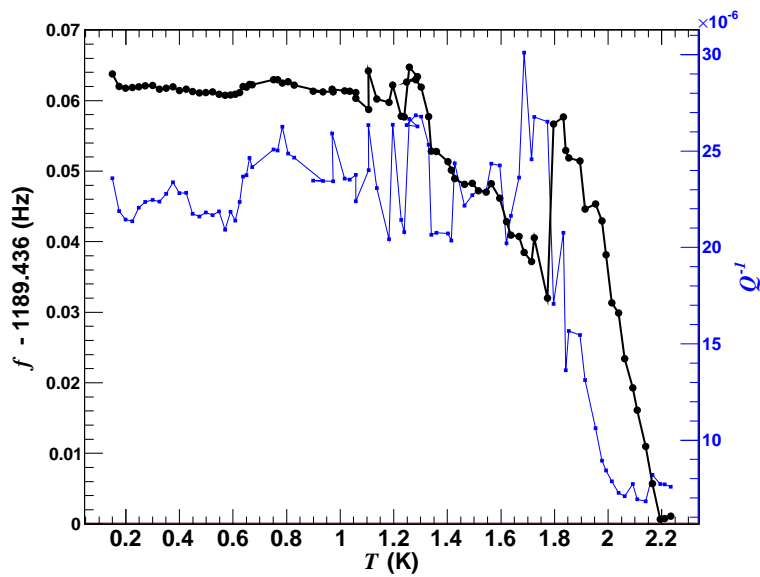


Fig. A.8: Graphene data as a function of temperature at 0.01 MPa. Used to find  $f_L$ .

## A.3 Grafoil Isotherms

## A.3.1 Melting

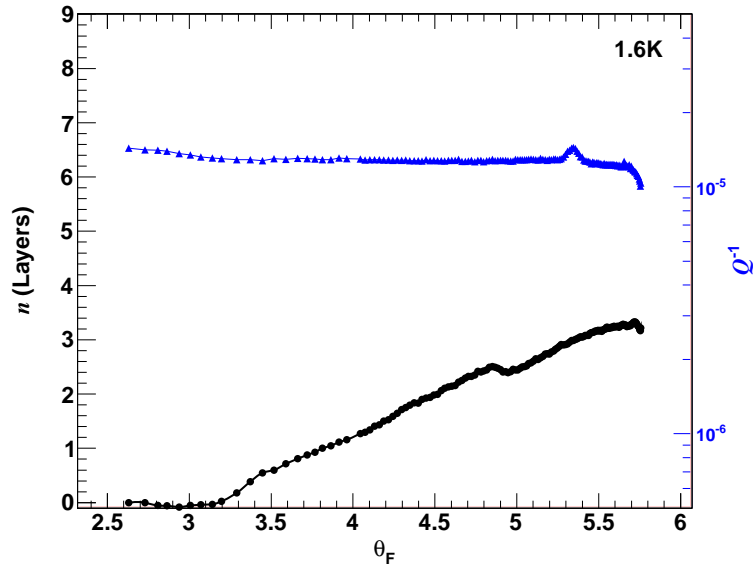


Fig. A.9: Grafoil melting 1.6 K isotherm.

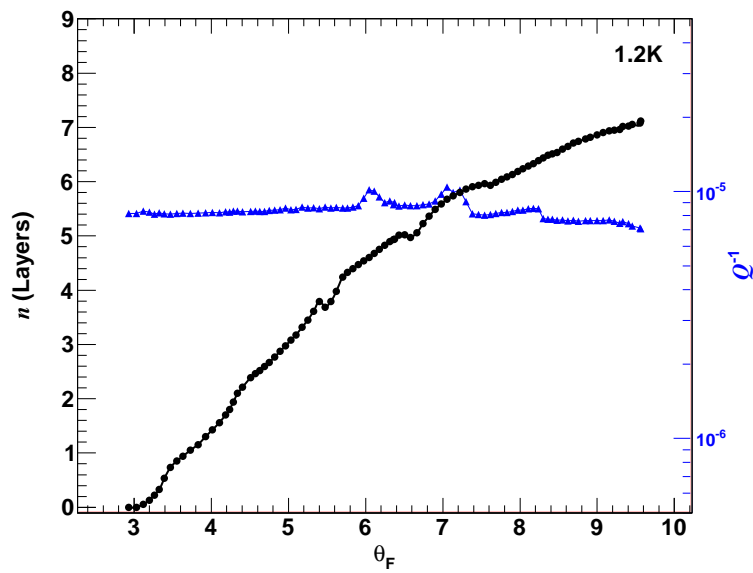


Fig. A.10: Grafoil melting 1.2 K isotherm.

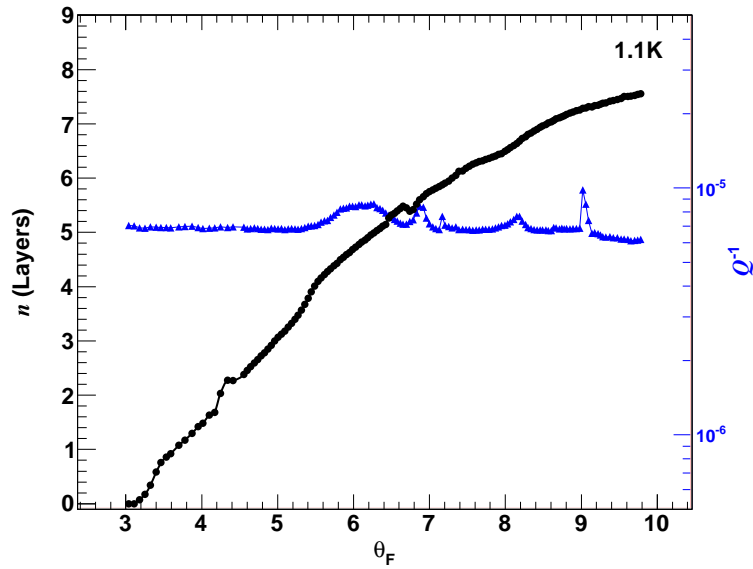


Fig. A.11: Grafoil melting 1.1 K isotherm.

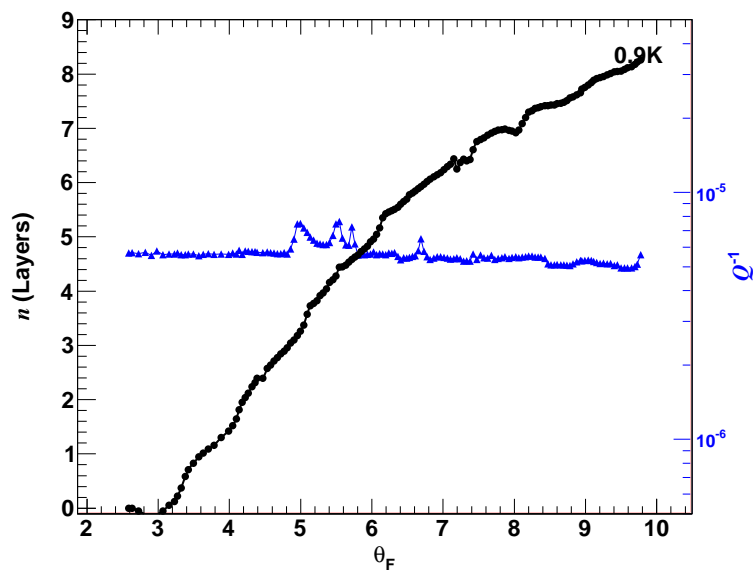


Fig. A.12: Grafoil melting 0.9 K isotherm.

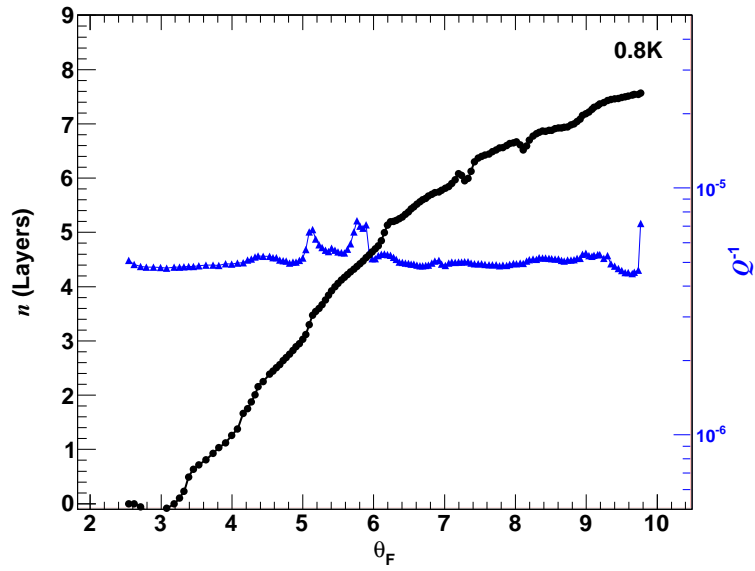


Fig. A.13: Grafoil melting 0.8 K isotherm.

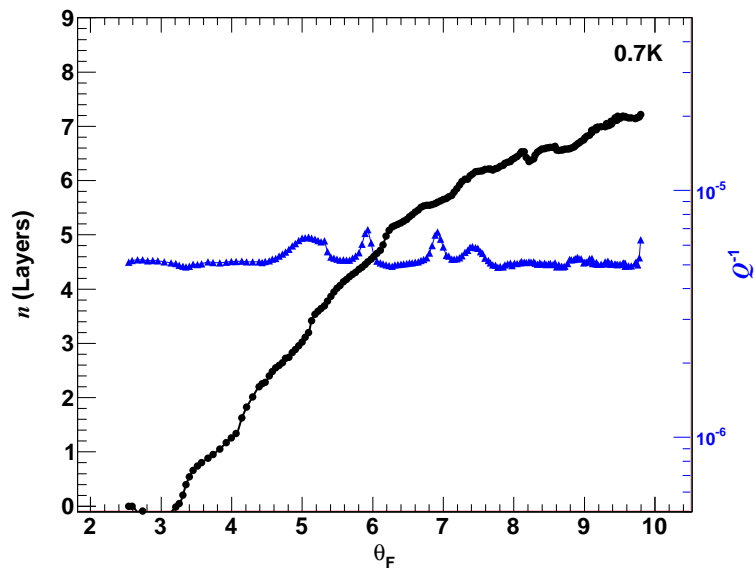


Fig. A.14: Grafoil melting 0.7 K isotherm.

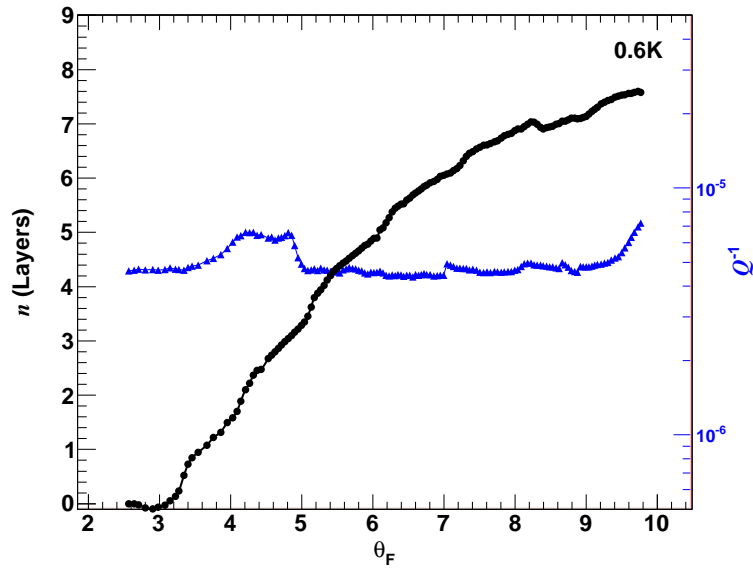


Fig. A.15: Grafoil melting 0.6 K isotherm.

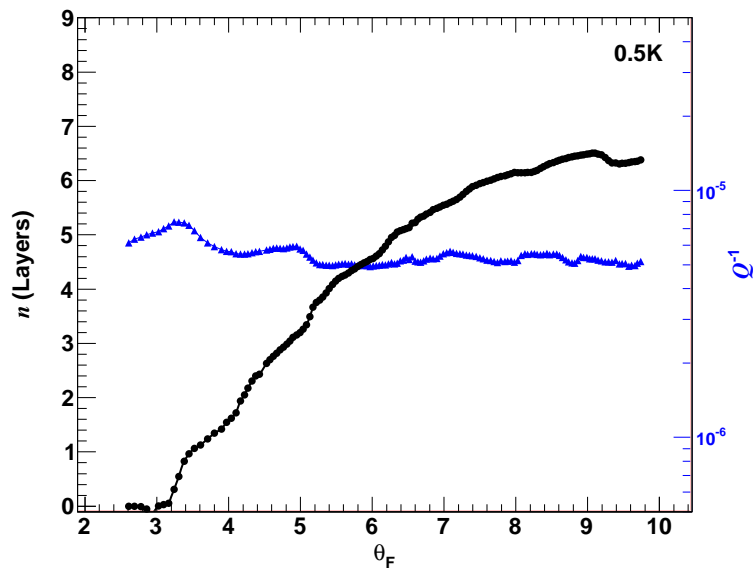


Fig. A.16: Grafoil melting 0.5 K isotherm.

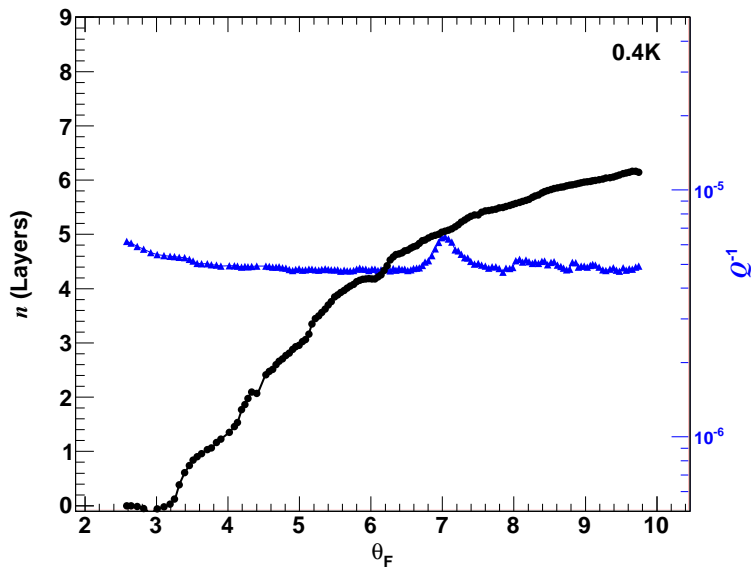


Fig. A.17: Grafoil melting 0.4 K isotherm.

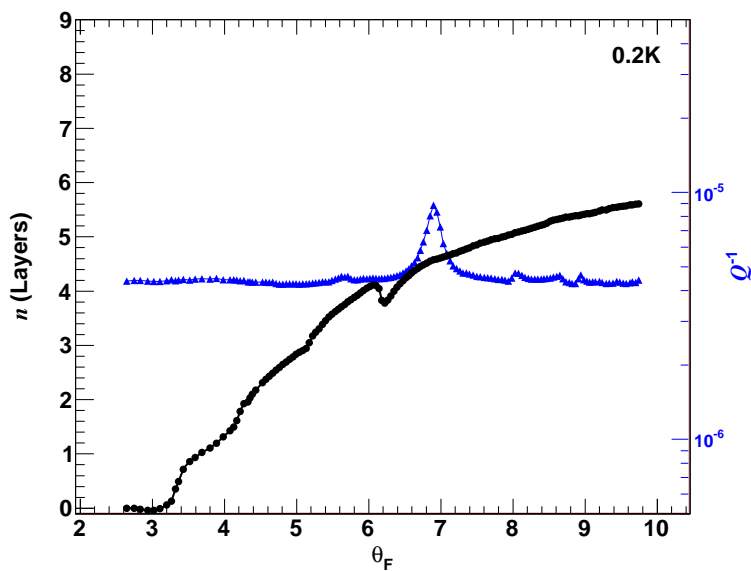


Fig. A.18: Grafoil melting 0.2 K isotherm.

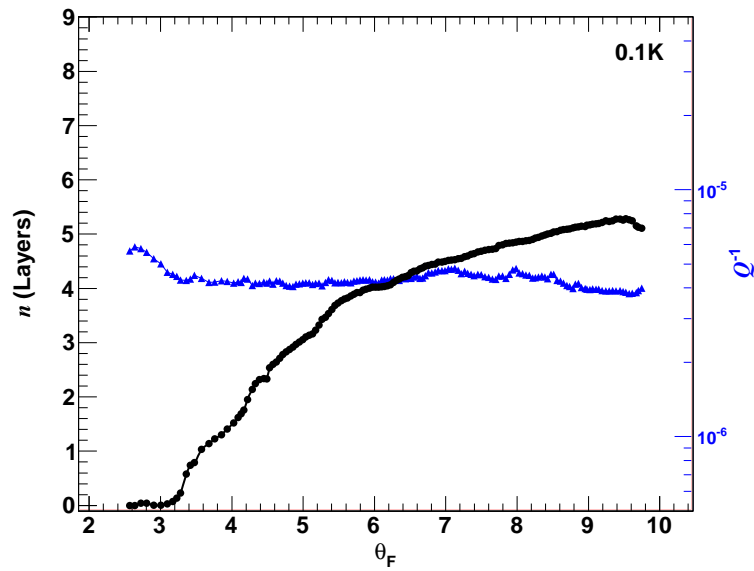


Fig. A.19: Grafoil melting 0.1 K isotherm.

A.3.2 Freezing

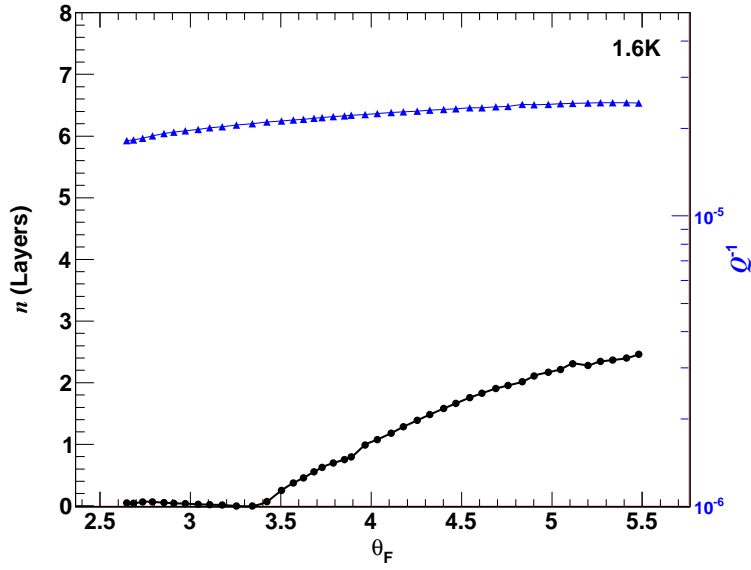


Fig. A.20: Grafoil freezing 1.6 K isotherm.

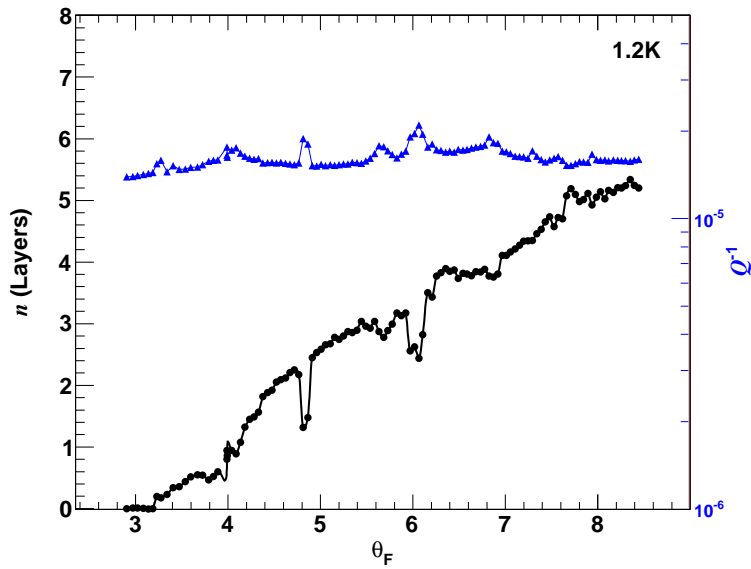


Fig. A.21: Grafoil freezing 1.2 K isotherm.

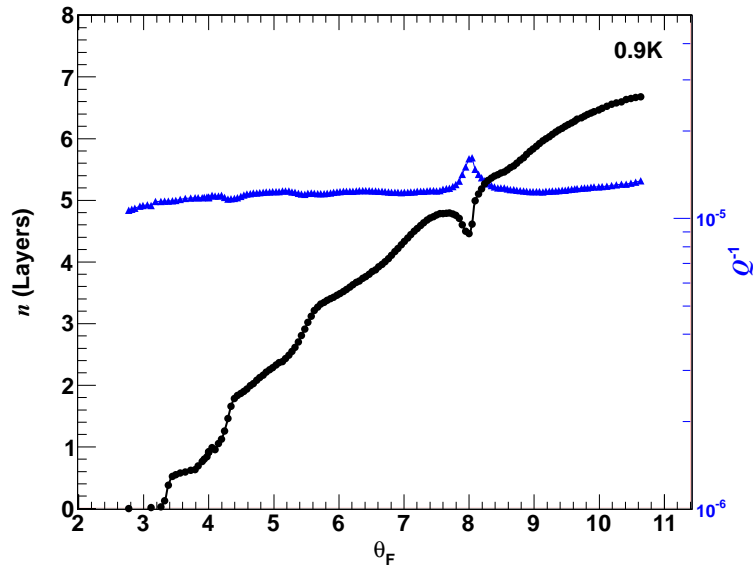


Fig. A.22: Grafoil freezing 0.9 K isotherm.

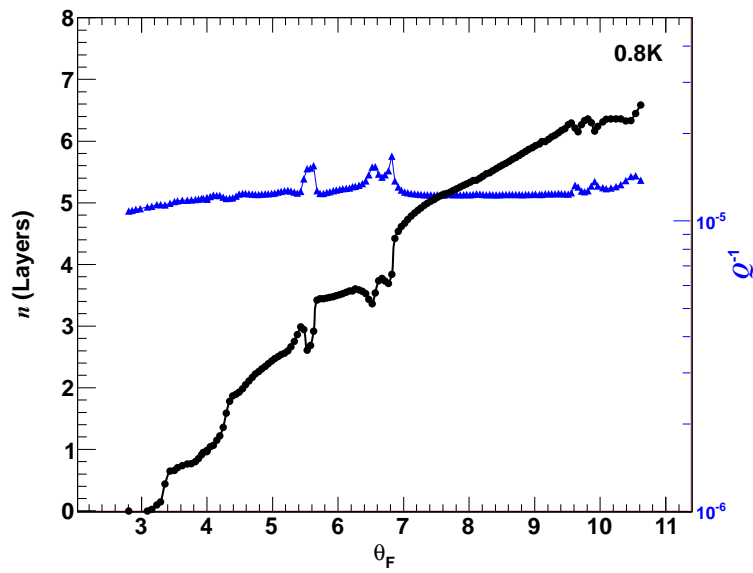


Fig. A.23: Grafoil freezing 0.8 K isotherm.

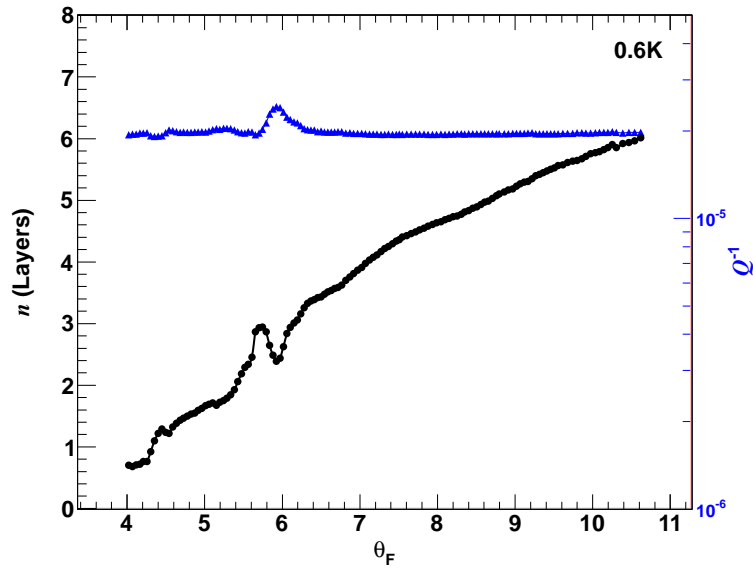


Fig. A.24: Grafoil freezing 0.6 K isotherm.

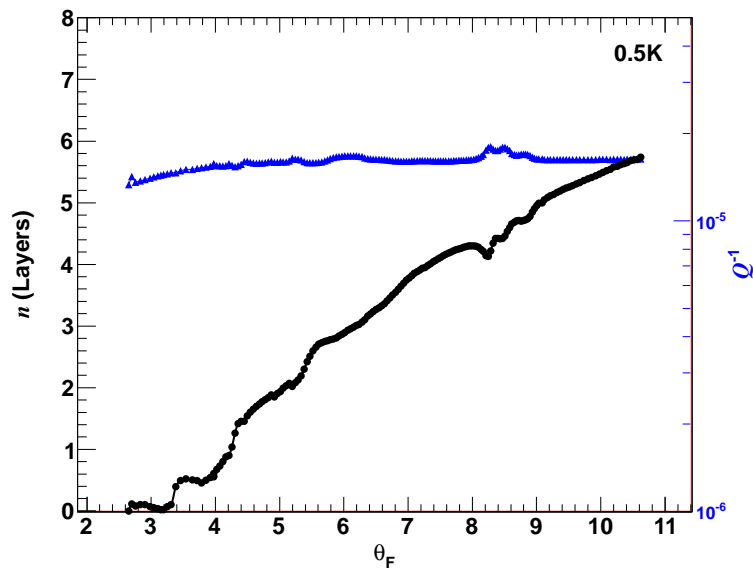


Fig. A.25: Grafoil freezing 0.5 K isotherm.

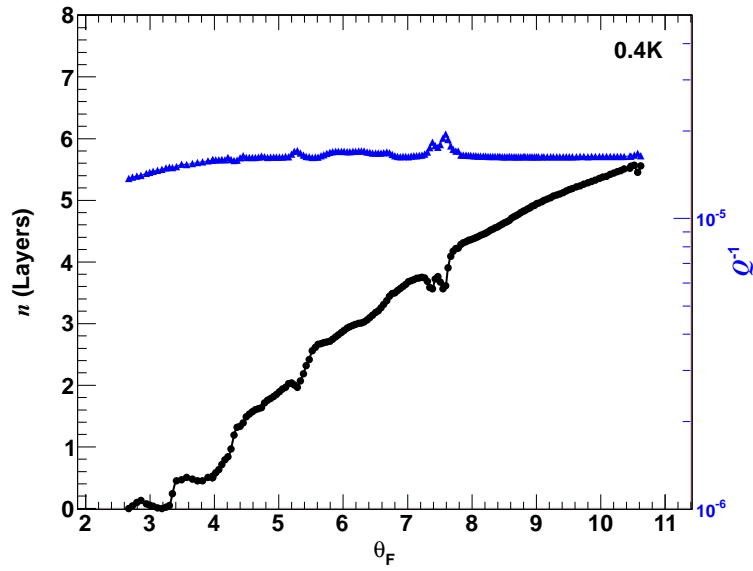


Fig. A.26: Grafoil freezing 0.4 K isotherm.

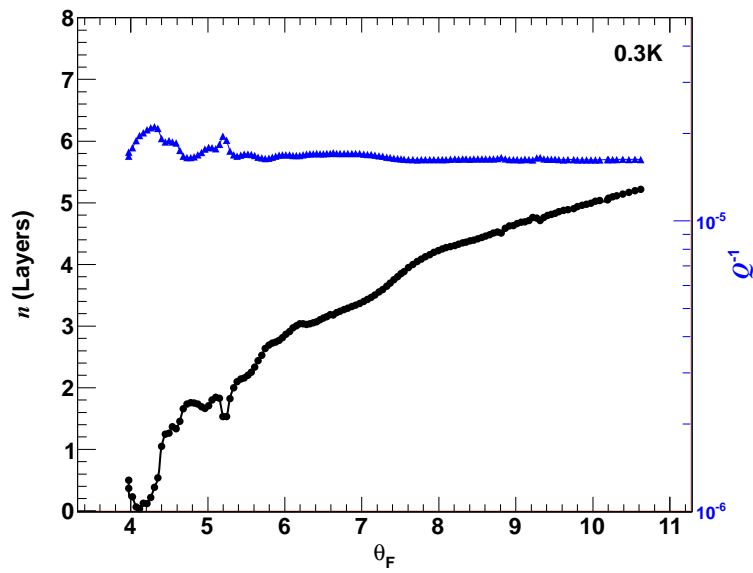


Fig. A.27: Grafoil freezing 0.3 K isotherm.

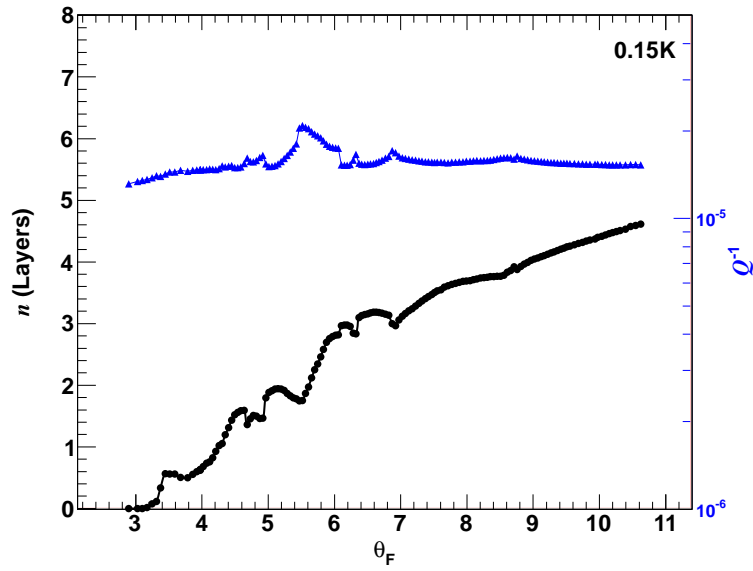


Fig. A.28: Grafoil freezing 0.15 K isotherm.

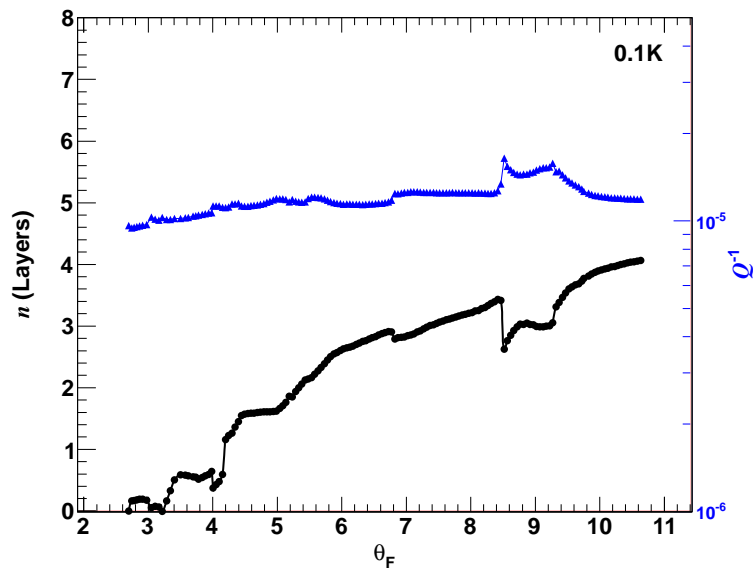


Fig. A.29: Grafoil freezing 0.1 K isotherm.

## A.4 Graphene Isotherms

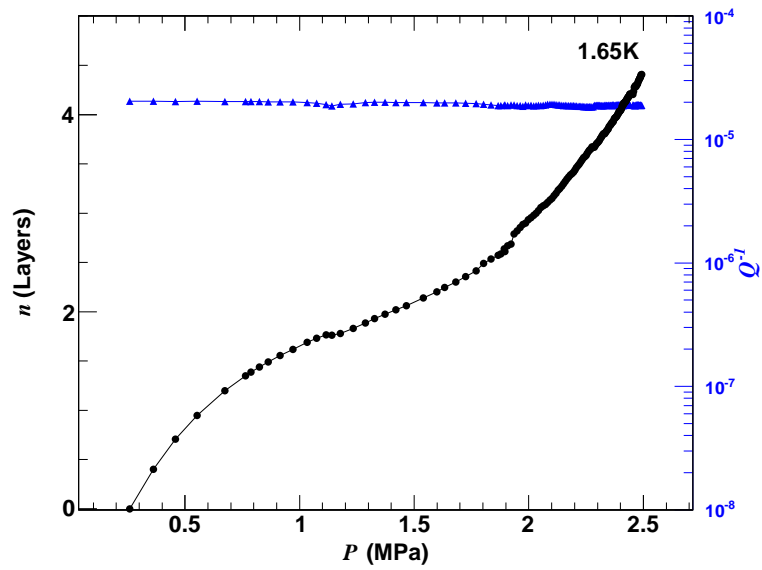


Fig. A.30: Graphene freezing 1.65 K isotherm.

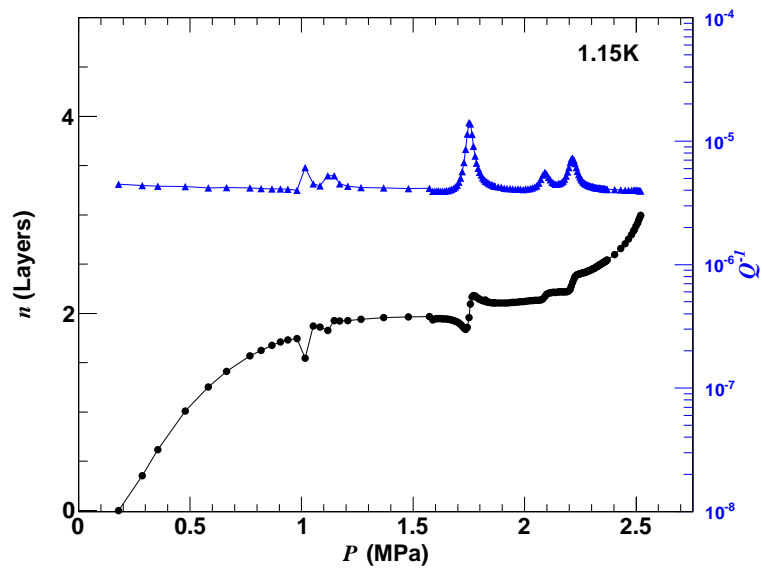


Fig. A.31: Graphene freezing 1.15 K isotherm.

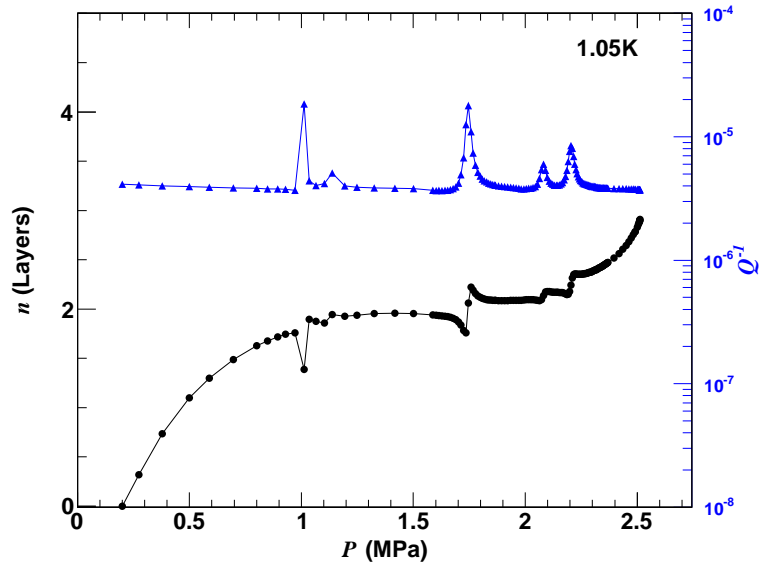


Fig. A.32: Graphene freezing 1.05 K isotherm.

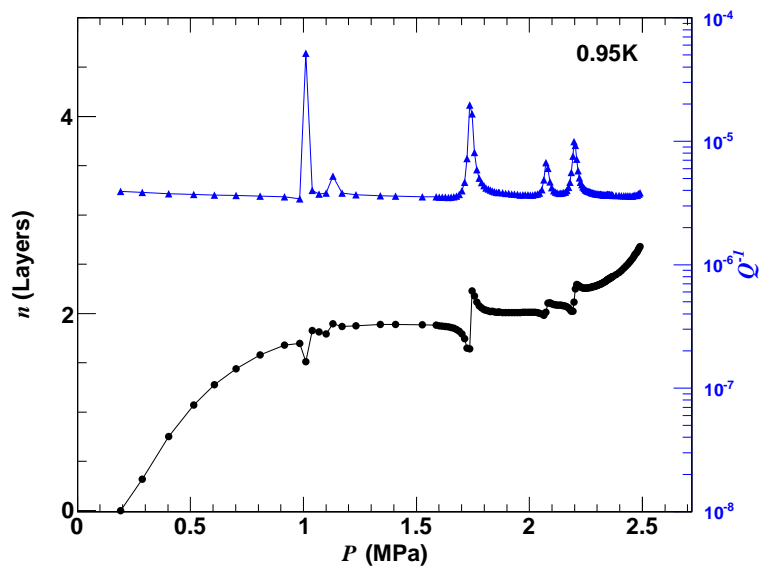


Fig. A.33: Graphene freezing 0.95 K isotherm.

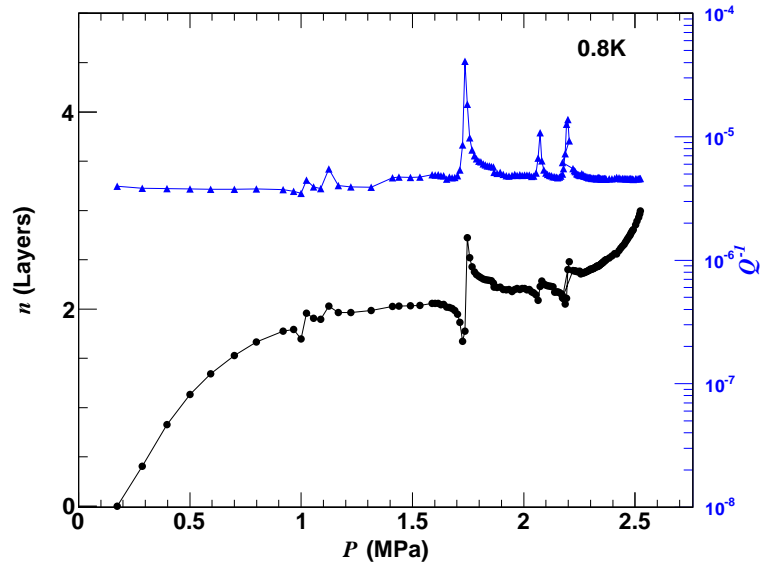


Fig. A.34: Graphene freezing 0.8 K isotherm.

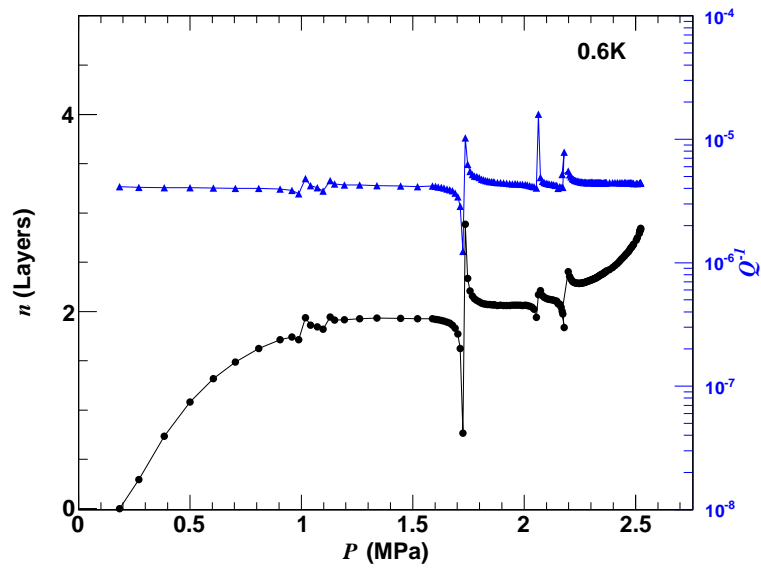


Fig. A.35: Graphene freezing 0.6 K isotherm.

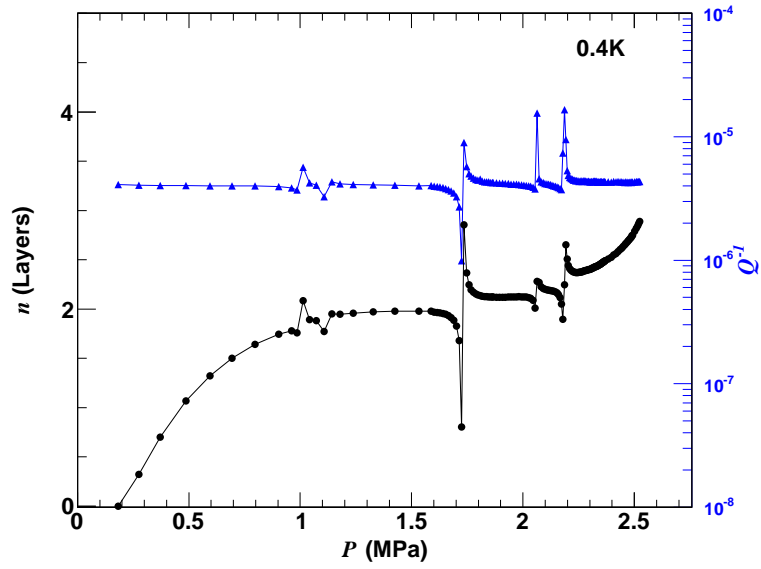


Fig. A.36: Graphene freezing 0.4 K isotherm.

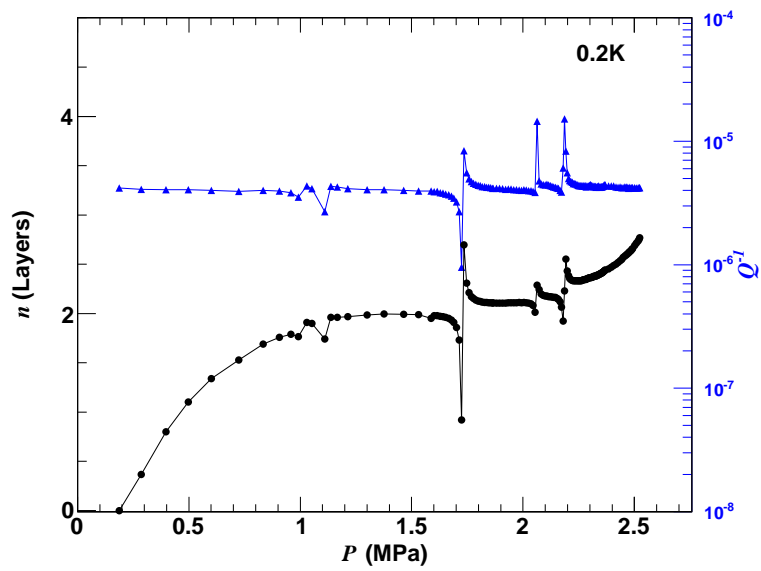


Fig. A.37: Graphene freezing 0.2 K isotherm.

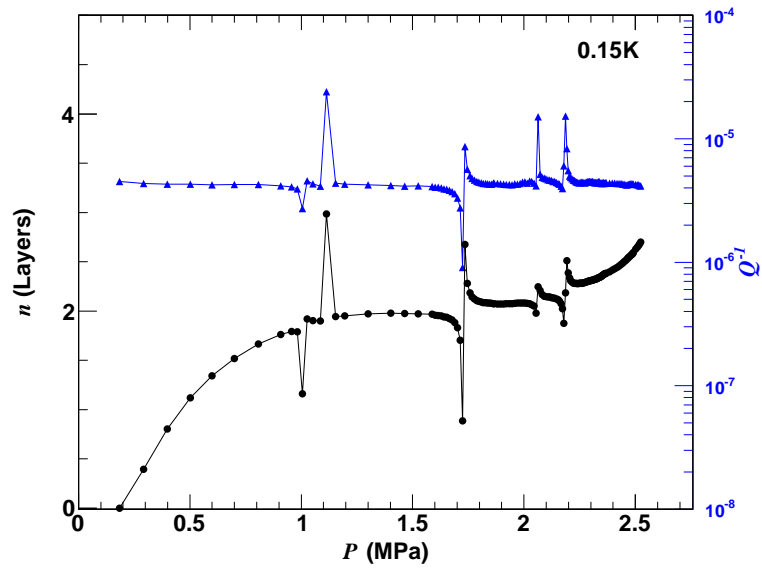


Fig. A.38: Graphene freezing 0.15 K isotherm.

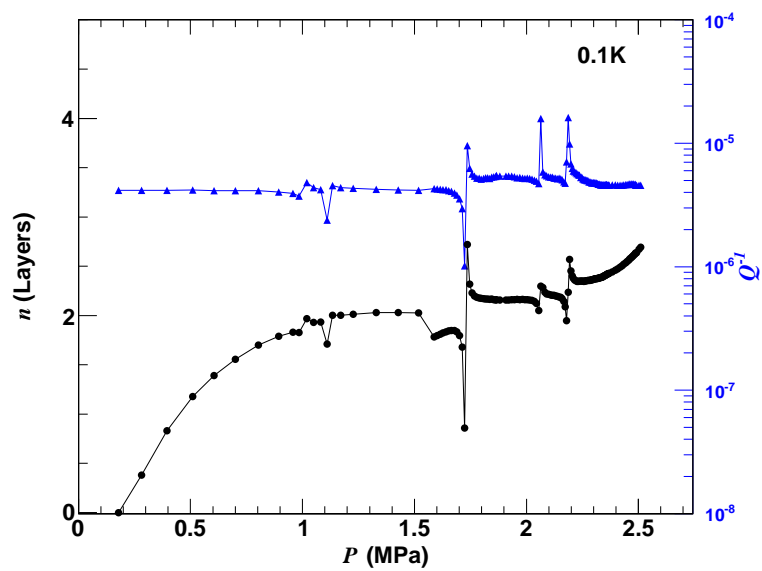
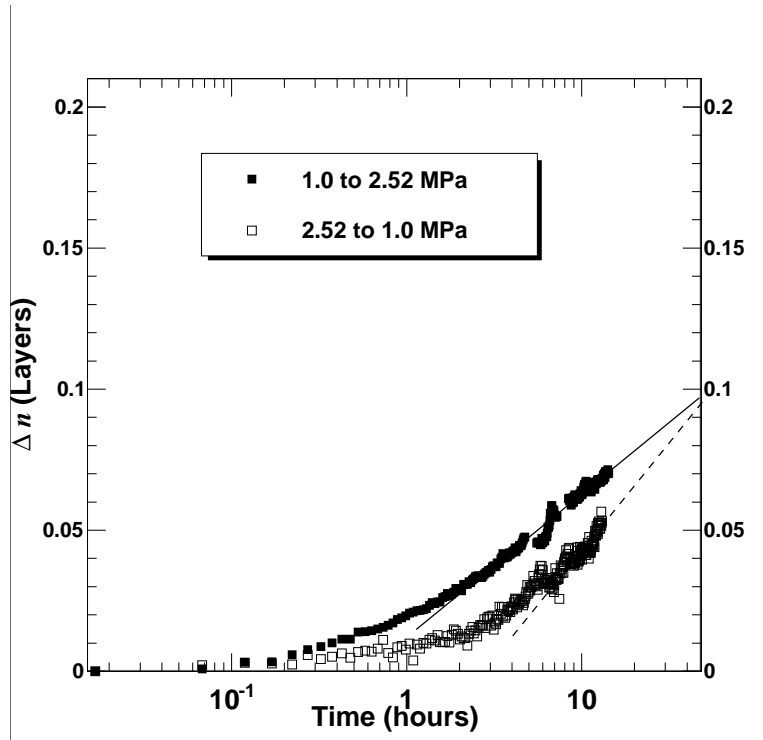


Fig. A.39: Graphene freezing 0.1 K isotherm.

A.5 Tunneling of  $^4\text{He}$  into Carbon Samples

**Fig. A.40:** Tunneling of  $^4\text{He}$  into the Grafoil sample as a function of time at 0.8 K. Straight lines are to guide the eye in extrapolating to Time = 48 hours.

Polturak and Eckstein (65) have seen that  $^4\text{He}$  can tunnel into graphite samples. Not only can  $^4\text{He}$  be adsorbed on the surface of graphite, but there may be voids and spaces created by the exfoliation process that can hold  $^4\text{He}$  atoms. It is doubtful that  $^4\text{He}$  can intercalate between graphene sheets, as this is energetically unfavorable. The number of atoms tunneling into samples was seen to have a logarithmic dependence on time and occur over very long periods that were on the order of days. The logarithmic dependence of the tunneling prompted Polturak and Eckstein to propose a two-well quantum model. One well is located on the “outside”, where  $^4\text{He}$  atoms can adsorb on the graphite surface from the liquid. The other well is located “inside” the graphite. Pressure differences between the outside and inside drive the tunneling effect into or out of the graphite. This effect was seen to be heavily sample dependent. The place into which atoms tunnel is not well understood. We have measured the size of the tunneling effect in our samples to ensure that our data is not heavily influenced by it.

In this thesis, atoms tunneling into the grafoil or graphene samples can increase the oscillator’s rotational inertia and artificially increase  $n$ . An upper bound for the

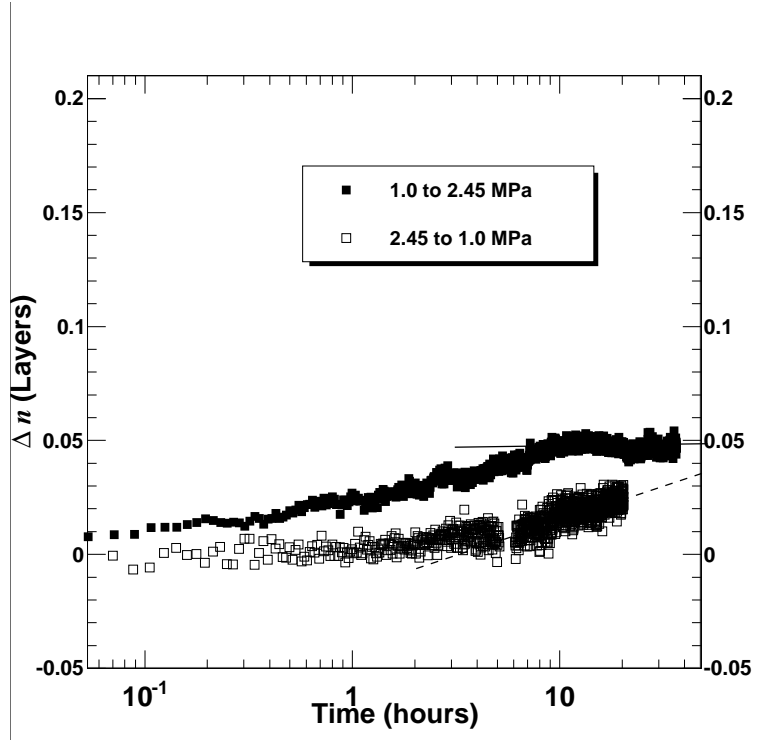


**Fig. A.41:** Tunneling of  $^4\text{He}$  into the Graphene sample as a function of time at 1.0 K. Straight lines are to guide the eye in extrapolating to Time = 48 hours.

tunneling effect was estimated for both cells in the following way. At constant temperature, the pressure was rapidly increased or decreased and then held constant. The pressure was changed from 1.0 MPa to just below  $P_s$  and vice versa. The rapid pressure change creates a pressure difference between the “outside” and “inside.” Even after the cell comes to equilibrium (within minutes), atoms tunnel into or out of the sample. To study the tunneling effect,  $f$  was measured each minute for over 1 day after inducing a rapid pressure change. A very small change in  $f$  was seen over time and converted into  $n$ .

Figure A.40 shows the tunneling effect for the grafoil cell and Fig. A.41 shows the effect for the graphene cell. Straight lines guide the eye and show the projected effect after 48 hours as the intersection with the vertical axis. 48 hours was the maximum time for any measurement in both experiments, but many measurements were taken within 24 hours or less. It is clear that the total tunneling effect is very small in both experiments: 0.1 layers for grafoil when compared to adsorption isotherms of 5-7 layers and 0.05 layers for graphene when compared to adsorption isotherms of 3 layers. Therefore, the tunneling effect is neglected when analyzing the data.

We believe that the tests performed here give an approximate upper bound for the

tunneling effect in our samples, but that the effect over the course of any measurement is smaller. First, the measurement time, as stated above, was usually much less than the projected 48 hours. Second, the pressure during a measurement is increased gradually in small steps. This produces much smaller pressure differences inside and outside the sample, probably leading to less tunneling.

# References

- [1] S. BALIBAR, H. ALLES, AND Y. A. PARSHIN. **The surface of helium crystals.** *Rev. Mod. Phys.*, **77**(1):317–370, May 2005. vii, 1, 5, 6, 58
- [2] S. RAMESH, Q. ZHANG, G. TORZO, AND J. D. MAYNARD. **Experimental Observation of the Increase of the Two-Dimensional Critical Temperature in Multilayer Adsorption.** *Phys. Rev. Lett.*, **52**(26):2375–2378, Jun 1984. vii, 1, 11, 12, 13, 57
- [3] V. GRIDIN, J. ADLER, Y. ECKSTEIN, AND E. POLTURAK. **Integral and Nonintegral Layer Formation in Multilayer Growth of Solid He4 on Grafoil.** *Phys. Rev. Lett.*, **53**(8):802–805, Aug 1984. vii, x, 1, 12, 14, 48, 57, 66, 69
- [4] M. J. MCKENNA, T. P. BROSIUS, AND J. D. MAYNARD. **Observation of Two-Stage Layering Transitions for Solid He4 on Graphite.** *Phys. Rev. Lett.*, **69**(23):3346–3349, Dec 1992. vii, 1, 12, 14, 15, 48, 57, 60, 75
- [5] V. ELSER. **Nuclear Antiferromagnetism in a Registered  $^3\text{He}$  Solid.** *Phys. Rev. Lett.*, **62**(20):2405–2408, 1989. x, 67, 68
- [6] K. O. KESHISHEV, A. Y. PARSHIN, AND A. V. BABKIN. **Experimental Detection of Crystallization Waves in  $\text{He}^4$ .** *Pisma Zh. Eksp. Teor. Fiz.*, **30**(1):63–67, July 1979. 1
- [7] L. D. LANDAU. *Collected Papers of L. D. Landau.* Permagon Press, New York, 1965. 1
- [8] S. T. CHUI AND J. D. WEEKS. **Dynamics of the Roughening Transition.** *Phys. Rev. Lett.*, **40**(12):733–736, Mar 1978. 1, 9
- [9] J. LANDAU AND W. F. SAAM. **Nucleation of Solid He4 Interfaces between Grafoil and High-Pressure Liquid He4.** *Phys. Rev. Lett.*, **38**(1):23–26, Jan 1977. 1, 9
- [10] D. A. HUSE. **Renormalization-Group Analysis of Layering Transitions in Solid Films.** *Phys. Rev. B*, **30**(3):1371–1376, Aug 1984. 1, 2, 11, 58, 75
- [11] S. RAMESH AND J. D. MAYNARD. **Measurement of Epitaxial Adsorption of Solid He4 on Graphite.** *Phys. Rev. Lett.*, **49**(1):47–50, Jul 1982. 1, 10, 12, 57
- [12] E. POLTURAK, V. GRIDIN, Y. ECKSTEIN, AND C. G. KUPER. **The Effect of Surface Solid on the Propagation of Sound Through Superfluid  $^4\text{He}$  in Grafoil.** *J. Low Temp. Phys.*, **58**(5):533–543, July 1985. 1, 12
- [13] J. D. WEEKS. **Variational Theory of Multilayer Solid Adsorption.** *Phys. Rev. B*, **26**:3998–4000, Oct 1982. 2

## REFERENCES

---

- [14] Y. NIIMI, T. MATSUI, H. KAMBARA, K. TAGAMI, M. TSUKADA, AND HIROSHI FUKUYAMA. **Scanning Tunneling Microscopy and Spectroscopy of the Electronic Local Density of States of Graphite Surfaces Near Monoatomic Step Edges.** *Phys. Rev. B*, **73**:085421, Feb 2006. 2, 12
- [15] H. WIECHERT, H.J. LAUTER, AND B. STHN. **Thermodynamic and neutron diffraction studies of the nucleation of solid<sup>4</sup>He on graphite.** *J. Low Temp. Phys.*, **48**(3-4):209–239, 1982. 2, 12
- [16] E. Y. ANDREI AND W. I. GLABERSON. **Sound Propagation in Helium-II in Grafoil.** *Phys. Rev. B*, **20**:4447–4449, Dec 1979. 2, 12, 58
- [17] E. R. GRILLY. **Compressibility of Liquid He<sup>4</sup> as a Function of Pressure.** *Phys. Rev.*, **149**(1):97, Sep 1966. 6
- [18] B. FÅK, T. KELLER, M. E. ZHITOMIRSKY, AND A. L. CHERNYSHEV. **Roton-Phonon Interactions in Superfluid <sup>4</sup>He.** *Phys. Rev. Lett.*, **109**:155305, Oct 2012. 6
- [19] J. P. FRANCK AND R. WANNER. **Elastic Constants of hcp He<sup>4</sup>.** *Phys. Rev. Lett.*, **25**:345–348, Aug 1970. 6, 49
- [20] K. O. KESHISHEV, A. Y. PARSHIN, AND A. V. BABKIN. **Experimental detection of crystallization waves in He<sup>4</sup>.** *JETP Letters*, **30**(1):56–59, 1979. 6
- [21] Y. ECKSTEIN, J. LANDAU, S. G. LIPSON, AND Z. OLAMI. **Role of Substrate Symmetry in Nucleating Solid Helium.** *Phys. Rev. Lett.*, **45**(22):1805–1808, Dec 1980. 7
- [22] D. S. FISHER AND J. D. WEEKS. **Shape of Crystals at Low Temperatures: Absence of Quantum Roughening.** *Phys. Rev. Lett.*, **50**(14):1077–1080, Apr 1983. 7
- [23] P. NOZIERES AND F. GALLET. **The Roughening Transition of Crystal Surfaces.** *J. Phys. (Paris)*, **48**:353, Apr 1987. 7
- [24] S. BALIBAR, F. GALLET, F. GRANER, AND E. ROLLEY. **The Roughening Transition and the Growth of Helium Crystals.** *Prog. in Crystal Growth and Characterization of Materials*, **26**:51–66, 1993. 9, 59, 62
- [25] S. FRANCHETTI. **The Problem of the Static Helium Film.** *Nuovo Cimento*, **4**:1504–1518, 1956. 9
- [26] B. LEWIS AND J. C. ANDERSON. *Nucleation and Growth of Thin Films.* Academic, New York, 1978. 16
- [27] H. G. SCHNEIDER, V. RUTH, AND T. KORMANY, editors. *Advances in Epitaxy and Endotaxy.* Elsevier, New York, 1990. 16
- [28] IVAN V. MARKOV. *Crystal Growth for Beginners: Fundamentals of Nucleation, Crystal Growth, and Epitaxy.* World Scientific, 1995. 16
- [29] P. A. CROWELL AND J. D. REPPY. **Superfluidity and Film Structure in <sup>4</sup>He Adsorbed on Graphite.** *Phys. Rev. B*, **53**:2701–2718, Feb 1996. 17

- [30] H. J. LAUTER, H. GODFRIN, AND P. LEIDERER. **4He Films on Graphite Studied by Neutron Scattering**. *J. Low Temp. Phys.*, **87**(3-4):425–443, 1992. 17
- [31] P. CORBOZ, M. BONINSEGNI, L. POLLET, AND M. TROYER. **Phase Diagram of 4He Adsorbed on Graphite**. *Phys. Rev. B*, **78**:245414, Dec 2008. 17, 64, 68
- [32] DENNIS S. GREYWALL. **Heat Capacity and the Commensurate-Incommensurate Transition of 4He Adsorbed on Graphite**. *Phys. Rev. B*, **47**:309–318, Jan 1993. 17, 64, 66, 67
- [33] M. C. GORDILLO AND J. BORONAT. **4He on a Single Graphene Sheet**. *Phys. Rev. Lett.*, **102**:085303, Feb 2009. 18
- [34] J. HAPPAHER, P. CORBOZ, M. BONINSEGNI, AND L. POLLET. **Phase Diagram of 4He on Graphene**. *Phys. Rev. B*, **87**:094514, Mar 2013. 18
- [35] Y. KWON AND D. M. CEPERLEY. **4He Adsorption on a Single Graphene Sheet: Path-integral Monte Carlo Study**. *Phys. Rev. B*, **85**:224501, Jun 2012. 18, 64
- [36] G. K. S. WONG IN. *Experimental Techniques in Condensed Matter Physics at Low Temperatures*. Addison-Wesley Publishing Co. Inc., 1988. 19, 21
- [37] K. SHIRAHAMA. *Kotai-butsumuri*, **30**(6), 1995. 19
- [38] G. C. STRATY AND E. D. ADAMS. **Highly Sensitive Capacitive Pressure Gauge**. *Rev. Sci. Instrum.*, **40**(11), 1969. 27
- [39] S. BRUNAUER, P. H. EMMETT, AND E. TELLER. **Adsorption of Gases in Multimolecular Layers**. *J. Am. Chem. Soc.*, **60**(2), 1938. 29, 77
- [40] [HTTP://XGSCIENCES.COM/PRODUCTS/GRAPHENE-NANOPLATELETS/](http://xgsciences.com/products/graphene-nanoplatelets/). 39
- [41] R. C. RICHARDSON AND E. N. SMITH. *Experimental Techniques in Condensed Matter Physics at Low Temperatures*. Addison Wesley, 1995. 42
- [42] C. BOGHOSIAN AND H. MEYER. **Density, Coefficient of Thermal Expansion, and Entropy of Compression of Liquid He4 Under Pressure Below 1.4K**. *Phys. Rev.*, **152**(1):200–206, Dec 1966. 48
- [43] A. M. KOGA, Y. SHIBAYAMA, AND K. SHIRAHAMA. **Layer by Layer Growth of Solid 4He on Graphite Down to 0.1 K**. *J. Low Temp. Phys.*, **166**(1):257–267, Mar 2012. 48
- [44] T. T. CHUNG AND J. G. DASH. **N2 Monolayers on Graphite: Specific Heat and Vapor Pressure Measurements Thermodynamics of Size Effects and Steric Factors**. *Surface Science*, **66**(2):559 – 580, 1977. 58
- [45] Y. LARHER. **The Critical Exponent Associated with the Two-Dimensional Condensation in the Second Adlayer of Argon on the Cleavage Face of Cadmium Chloride**. *Mol. Phys.*, **38**(3):789–795, 1979. 58
- [46] T. A. RABEDAU AND T. S. SULLIVAN. **Adsorption Binding-Energy Variation Resulting from Substrate Size Effects**. *Phys. Rev. B*, **34**:8118–8121, Dec 1986. 58

## REFERENCES

---

- [47] J. G. DASH AND R. D. PUFF. **Phase Transitions in Heterogeneous Films.** *Phys. Rev. B*, **24**:295–309, Jul 1981. 58
- [48] R. E. ECKE, J. G. DASH, AND R. D. PUFF. **Effects of Energy Heterogeneity on Phase Transitions in a Model Monolayer System.** *Phys. Rev. B*, **26**:1288–1296, Aug 1982. 58
- [49] R. E. ECKE, J. MA, A. D. MIGONE, AND T. S. SULLIVAN. **Effects of Substrate Heterogeneity on Adsorption Isotherms Near a Two-Dimensional Gas-Liquid Critical Point.** *Phys. Rev. B*, **33**:1746–1751, Feb 1986. 58
- [50] C.A SHOLL AND N.H FLETCHER. **Decoration Criteria for Surface Steps.** *Acta Metallurgica*, **18**(10):1083 – 1086, 1970. 59
- [51] S. DIETRICH. **Wetting Phenomena.** In C. DOMB AND J. L. LEBOWITZ, editors, *Phase Transitions and Critical Phenomena*, **12**. Academic Press, 1988. 59
- [52] P. BAK. **Commensurate Phases, Incommensurate Phases and the Devil’s Staircase.** *Reports on Progress in Physics*, **45**(6):587, 1982. 66, 72
- [53] D. S. GREYWALL AND P. A. BUSCH. **Heat Capacity of  $^3\text{He}$  Adsorbed on Graphite at Millikenvin Temperatures and Near Third-Layer Promotion.** *Phys. Rev. Lett.*, **62**(16):1868, 1989. 67
- [54] D. S. GREYWALL AND P. A. BUSCH. **Heat Capacity of Fluid Monolayers of  $^4\text{He}$ .** *Phys. Rev. Lett.*, **67**(25):3535–3538, Dec 1991. 68
- [55] F. LONDON. *Superfluids*, **2**. Wiley, 1954. 70
- [56] G.S. KELL, G.E. MCLAURIN, AND E. WHALLEY. **Second Virial Coefficient of Helium from 0 to 500 C by the Two-Temperature Gas-Expansion Method.** *J. Chem. Phys.*, **68**:2199–2205, 1978. 70
- [57] R. OUBOTER AND C. N. YANG. **Thermodynamic Properties of Liquid  $^3\text{He}$ - $^4\text{He}$  Mixtures.** *Physica B*, **144**:127–144, 1987. 71
- [58] P. M. CHAIKIN AND T. C. LUBENSKY. *Principles of Condensed Matter Physics*. Cambridge University Press, 1995. 72
- [59] S. N. COPPERSMITH, DANIEL S. FISHER, B. I. HALPERIN, P. A. LEE, AND W. F. BRINKMAN. **Dislocations and the Commensurate-Incommensurate Transition in two Dimensions.** *Phys. Rev. Lett.*, **46**:869–869, Mar 1981. 72
- [60] D. A. HUSE AND M. E. FISHER. **Domain Walls and the Melting of Commensurate Surface Phases.** *Phys. Rev. Lett.*, **49**:793–796, Sep 1982. 72
- [61] E. D. SPECHT, M. SUTTON, R. J. BIRGENEAU, D. E. MONCTON, AND P. M. HORN. **Phase Diagram and Phase Transitions of Krypton on Graphite in the One-to-Two-Layer Regime.** *Phys. Rev. B*, **30**:1589–1592, Aug 1984. 72

- [62] J. AMRIT, P. LEGROS, AND J. POITRENAUD. **Rough and Vicinal Surfaces of Helium-4 Crystals. Mobility Measurements.** *Journal of Low Temperature Physics*, **100**(1-2):121–130, 1995. 73
- [63] D. O. EDWARDS, S. MUKHERJEE, AND M. S. PETERSEN. **Quantum Kinks and the Growth Resistance of Atomically Rough  $^4\text{He}$  Crystals.** *Phys. Rev. Lett.*, **64**:902–905, Feb 1990. 73
- [64] K. H. ANDERSEN, J. BOSSY, J. C. COOK, O. G. RANDL, AND J.-L. RAGAZZONI. **High-Resolution Measurements of Rotons in  $^4\text{He}$ .** *Phys. Rev. Lett.*, **77**:4043–4045, Nov 1996. 73
- [65] E. POLTURAK AND Y. ECKSTEIN. **Low-Temperature Tunneling of  $^4\text{He}$  Atoms into Graphite.** *Phys. Rev. Lett.*, **58**(25):2680, 1987. 100